PH & TEMPERATURE MEASUREMENTS UTILIZING FCS

PH AND TEMPERATURE MEASUREMENTS IN BIOLOGICAL SYSTEMS UTILIZING THE ENVIRONMENTAL SENSITIVITY OF PROTON TRANSFER IN FLUOROPHORES

By

FELIX HAU CHUN WONG, B.Sc., M.Sc.

A Thesis

Submitted to the School of Graduate Studies

in Partial Fulfillment of the Requirements

for the Degree

Doctor of Philosophy

McMaster University

DOCTOR OF PHILOSOPY (2010) McMaster University

(Physics and Astronomy) Hamilton, Ontario, Canada

TITLE: pH and Temperature Measurements in Biological Systems Utilizing the Environmental Sensitivity of Proton Transfer in Fluorophores

AUTHOR: Felix Hau Chun Wong

B.Sc. & M.Sc. (McMaster University)

SUPERVISOR: Dr Cécile Fradin

NUMBER OF PAGES: xiv, 130

Acknowledgements

It is difficult to overstate my gratitude to my Ph.D. supervisor Dr. Cécile Fradin. Throughout my graduate studies, she provided encouragement, sound advice, good teaching, and good ideas. I would have been lost without her guidance. In addition, her patience and her trust in my ability helped me going through the difficult times.

I would like to thank the many people who helped me in my research. First, I thank the members of my supervisory committee, Dr. Kari Dalnoki-Verses and Dr. Tom Farrell for providing good advices to my works. I thank Dmitri Satsoura for providing the fusion protein of EGFP and Bax. I thank Asmahan Abu-Arish and Daniel Banks for their contributions in the EGFP project. I would also like to thank Dr. Stephen Ferguson and Lianne B. Dale at University of Western Ontario for providing the μ-opioid receptor expressing HEK 293 cells. Furthermore, I own many thanks to Corrie Griffiths for providing assistance in the laboratory, Tony Collins and Jamie McNicol for their technical supports at the McMaster Biophotonics Facility.

I also want to take a moment to thank all former and present members in Fradin group for providing a fun and stimulating environment to learn and to work, and I will definitely cherish the time when I worked with them. I particularly thank Asmahan and Daniel for being great colleagues and great friends. I also thank the secretaries in Department of Physics & Astronomy for assisting me in many ways. I thank all the people that I met at McMaster over the years who made my study at Mac a great experience.

Last but not the least, I thank my entire family for providing a loving environment for me.

Abstract

A great number of cellular processes can lead to local changes in proton concentration and temperature. So, it is desirable to be able to measure pH and temperature with non-invasive and spatially resolved methods. In this thesis, I describe two unique methods to measure pH and temperature using the environmental sensitivity of the proton transfer of fluorescent molecules. The first method is based on the detection of the temperature and pH dependent parameters associated with the blinking of fluorophores by fluorescence correlation spectroscopy (FCS). Employing EGFP as the probe, I used this method to characterize temperature increase at a laser focus due to light absorption in a thin liquid sample. Using pyranine as a probe, I extended the applicability of this method to a range of pH including physiological pH. Also, I investigated in details the effect of buffer composition on the blinking of the fluorophores. Then, I concluded that one limitation of this method is its strong dependence on buffer conditions, which are not well characterized *in vivo*. The second approach is a pH measurement method based on ratiometric imaging. This method is not as dependent on buffer condition. We improved on current ratiometric imaging techniques by demonstrating the possibility of using two-photon excitation. This method was used to measure pH in pyranine loaded vesicles created during receptor-mediated endocytosis of μ-opioid receptors expressed in HEK 293 cells. Preliminary results showed that the pH in the endocytic vesicles dropped to a value similar to those measurements in late endosomes roughly ~ 10 minutes after triggering the endocytosis, and eventually, the pH reading reached a value similar to that of the pH of lysosomes.

Table of Contents

Abbreviations

ADP:	Adenosine diphosphate
ATP:	Adenosine triphosphate
BCECF:	2',7'-bis(carboxyethyl)-5(6)-carboxyfluorescein
DAMGO:	[D-Ala^2, N-Me-Phe^4, Gly^5-ol]-Enkephalin acetate salt
DDW:	Deionized distilled water
DIC:	Differential interference contrast
ECFP:	Enhanced cyan fluorescent protein
EGFP:	Enhanced green fluorescent protein
EYFP:	Enhanced yellow fluorescent protein
FBS:	Fetal bovine serum
FCS:	Fluorescence correlation spectroscopy
FLIM:	Fluorescence lifetime imaging microscopy
FRET:	Fluorescent resonance energy transfer
G418:	Geneticin
GFP:	Green fluorescent protein
GRK:	G protein-coupled receptor kinase
GPCR:	G protein-coupled receptor
GRP:	G protein-coupled receptor phosphatase
HA:	Hemagglutinin epitope
HBSS:	Hank's balanced salt solution
HEK 293:	Human embryonic kidney cell
HEK293-MOR:	μ-opioid receptor transfected HEK 293
wt-HEK293:	wild type HEK 293
HPTS:	1-hydroxypyrene-3,6,8-trisulfonic acid (Pyranine)
α-MEM:	Minimum essential medium
NIR:	Near infra-red
PBS:	Phosphate buffered saline
SCC:	Sodium copper chlorophyllin

LIST OF FIGURES

Chapter 3

Chapter 4

Appendix

LIST OF TABLES

Chapter 1

Background

Our ability to observe biological processes at the level of a single cell level has improved tremendously in the last two decades with the introduction of various techniques. In addition, a current trend in the development of chemical systems is toward miniaturization in order to reduce the amount of materials required for a chemical reaction. Therefore, new approaches are needed to measure changes of environmental conditions during a chemical reaction within a tiny liquid volume, for example a cell or a microfluidic device. Among all environmental parameters, pH and temperature are arguably the two most important, because they are the driving forces behind many cellular processes. In this thesis, I present two unique approaches to measure pH or temperature in biological systems. In this introduction chapter, I start by discussing the importance of pH and temperature in cellular processes (section 1.1). Then, I highlight a few pH and temperature measurement methods that are based on fluorescence in section 1.2. Finally, I describe in details two chemical sensors that were used to measure pH and temperature in this thesis.

1.1 Importance of proton transfer and heat production in cellular processes

The survival of organisms is affected by their surrounding environmental conditions such as pH and temperature. As a result, different organisms have developed their own mechanisms to respond to changes in environmental pH and temperature, and keep their intracellular conditions stable. On the other hand,

many cellular processes can induce local pH or temperature changes. In fact, a pH gradient generates electric potential, hence potential energy, and a temperature change is equivalent to a change in thermal energy. Therefore, these energies can drive many thermodynamically unfavourable reactions. In addition, there is an interplay between electrical potential energy, thermal energy, and mechanical energy in many cellular reactions. So, it is important to specify these energies in order to fully understand the mechanisms of a cellular process. In the rest of section 1.1, several examples are discussed to illustrate the importance of pH and temperature in cellular reactions.

1.1.1 ATP synthesis and proton transfer in mitochondria

Adenosine triphosphate (ATP) is the basic energy currency at the cellular level. ATP synthesis is a chemical reaction that binds ADP (adenosine diphosphate) and a phosphate ion (HPO_4^{2-}), and this reaction takes place in mitochondria during cellular respiration. For ATP synthesis at the mitochondria, the transfer of protons across the mitochondrial membrane is an important step (reviewed in ref [1] and [2]). During cellular respiration, the breakdown of carbohydrate molecules releases electrons in addition to CO_2 and water. The electrons are then transported through the respiratory enzyme complexes on the mitochondrial inner membrane, and this electron-transport chain pumps protons across the membrane from the mitochondrial matrix to the intermembrane space. Therefore, it creates a proton gradient (difference in pH) across the inner membrane. The build-up of a proton gradient across the membrane generates a potential energy, and this potential energy drives protons back to the mitochondrial matrix through a large protein complex called ATP synthase. The passing of protons through the ATP synthase rotates the protein complex like a turbine, and this motion synthesizes ATP from ADP and phosphate ion. As a result, the electrical potential energy stored on the mitochondrial membrane is

converted to mechanical energy to rotate the ATP synthase, and then to chemical energy for ATP synthesis.

1.1.2 Heat production in mitochondria

Adaptive thermogenesis is an example that illustrates how heat production in our body responds to the temperature changes in the surrounding environment or to our diet, and it involves many cellular processes, from the brain sensing the cold to the heat production in the mitochondria inside the cells (reviewed in ref. [1]). For the non-shivering thermogenesis, instead of being converted into ATP, the energy of oxidation during the mitochondrial respiration is dissipated as heat, a reaction most likely to occur in brown fat cells (reviewed in ref. [2] and [3]). This mitochondrial respiration is uncoupled from ATP synthesis, and it requires a special transport protein (uncoupling proteins) to dissipate the energy of the proton gradient before activating ATP synthase. The mitochondrial uncoupling respiration is the main cellular reaction in thermogenesis. Nakamura and Matsuoka used calorimetry to investigate the heat production of mitochondrial uncoupling respiration. By monitoring the temperature change and the oxygen consumption in a suspension of rat liver mitochondria with the uncoupling proteins using a calorimeter, they estimated that the heat production of the uncoupling respiration is 29 ± 7 kJ/mol (~ 7.2 kcal/mol) [4].

1.1.3 ATP hydrolysis and temperature

ATP hydrolysis is the reverse reaction of ATP synthesis. The energy released by ATP hydrolysis under normal physiological conditions is between 11 and 13 kcal/mol [2]. As the result, the relatively high energy production of ATP hydrolysis can drive many thermodynamically unfavorable cellular reactions; for example, numerous molecular motors are driven by ATP hydrolysis. Kinesin is a

major cargo transporting molecular motor found in mammalian cells, and this molecular motor moves along microtubules by hydrolyzing ATP. Myosin is another major example of molecular motor found in muscle cells. This molecular motor walks along the actin filament through ATP hydrolysis as well, and it is responsible for the sliding of the actin filament in muscle cells that causes muscle contraction (all reviewed in ref. [2]). In addition, the rate of ATP hydrolysis in myosin is affected by temperature. When Harada et al studied the actin filament moving on a coated surface with actomyosin, they found that the sliding velocity of the filament increases two-fold with an increase in temperature from 22 to 30°C [5]. They also showed that the ATPase, the enzyme which catalyzed ATP hydrolysis, is five times more active at 30°C than 20°C. On the other hand, the excess energy released in ATP hydrolysis is converted to heat as a byproduct of muscle contraction, an important mechanism of thermogenesis during shivering [6].

1.1.4 Proton transfer in lysosomes

Lysosomes are membrane-bound digestive organelles in the cells that contain lysosomal enzymes such as proteases, nucleases, and glycosidases. These enzymes are involved in the hydrolysis of macromolecules. As their names suggest, proteases break down proteins to amino acids; nucleases break down nucleic acids into nucleotides; glycosidases break down large sugar molecules into smaller units. All of the lysosomal enzymes are acid hydrolases, which means their optimal activity is obtained in acidic environment (pH ~ 5) [2]. On the membrane of the lysosome, there are proton pumps that create such an acidic environment inside the organelle. H^+-ATPase is a major proton pump found on the lysosomes and it couples the energy released from ATP hydrolysis to proton pumping from cytosol into lysosome.

1.1.5 Importance of pH in endocytosis

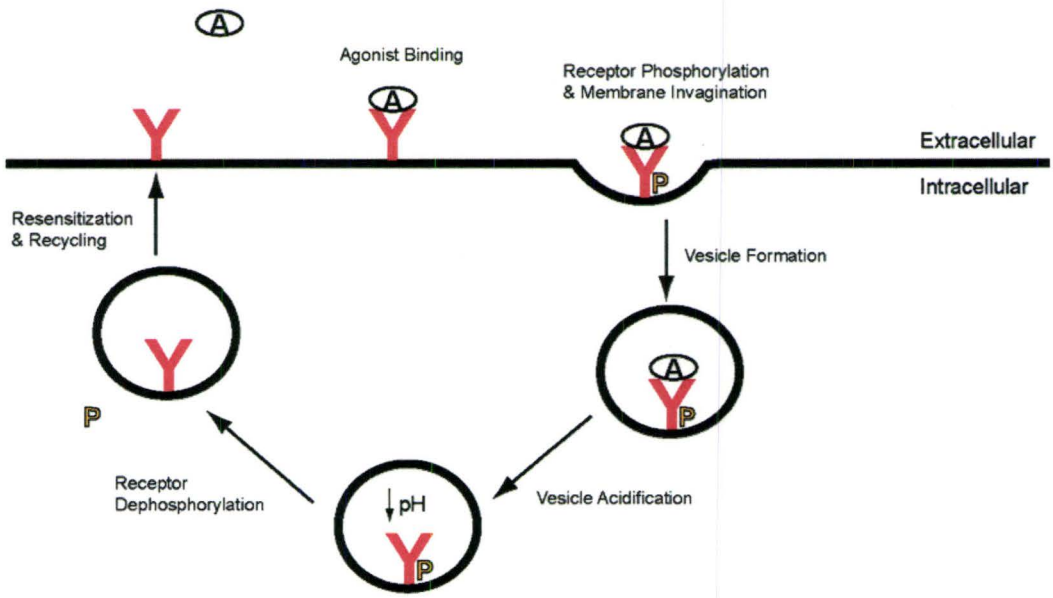

Figure 1.1. Schematic diagram of receptor resensitization during receptor-mediated endocytosis.

Endocytosis is a cellular process that consists in the uptake of extracellular materials by membrane invagination. Eventually, the invagination buds off to form tiny intracellular vesicles (~ 0.2 μm in diameter [7]) and can be transported to different compartments in cells, such as golgi and lysosome. Receptor-mediated endocytosis is a specific type of endocytosis that is triggered by the binding of an agonist to a membrane receptor. An agonist is a ligand that binds to a receptor and triggers a cellular response. This type of endocytosis usually occurs at the junctions between neurons, or between neurons and other type of cells, for signaling purposes.

G protein-coupled receptors (GPCRs) comprises a large family of membrane proteins related to signal transduction in cells. There have been numerous studies focused on GPCRs mediated endocytosis (reviewed in ref. [8-

11]). These studies show that the binding of agonists to the receptors leads to G protein-coupled receptor kinases (GRK) mediated phosphorylation of the receptor. Subsequently, a rapid binding of β-arrestin and G protein-coupled receptor phosphatase (GRP) to the receptor occurs, and this reduces the responsiveness of the receptor to binding of subsequent agonist (receptor desensitization). Endocytosis then begins with membrane invagination at a clathrin-coated region on the cell membrane. Although the mechanism is still not clear, eventually, the clathrin-coated pit pinches off as an endocytic vesicle. The endocytic vesicle first fuses with the early endosomes, and the extracellular materials in the endosomes are then sent to different organelles through transport vesicles. On the other hand, the internalized receptors are sent back to the cell surface from the early endosome through a recycling vesicle.

During the recycling process, resensitization of the receptor occurs. The resensitization process is thought to involve the acidification of the recycling vesicle by H^+-ATPase. Krueger et al have shown that a decrease in pH induces a change in receptor conformation (pH ~ 5) [8]. This conformational change then induces the receptor dephosphorylation, at which point, the responsiveness of the receptor returns. Recently, Iyer et al showed that the receptor is able to undergo dephosphorylation without internalization [12]. They also found that the rate of receptor dephosphorylation is the same with or without receptor internalization. However, as pointed out in ref. [13], their work did not explain why inhibitors of the receptor internalization can block receptor resensitization, or the significances of this finding in receptor signaling. Among all reactions in receptor-mediated endocytosis, the desensitization and resensitization of the receptors are the focus of many studies, because these two processes are strongly related to the understanding of tolerance to drugs. In the conventional view of the resensitization process, acidification in the recycling vesicle is an essential step to

resensitize the receptors. Later in chapter 4, I will show *in vivo* pH measurements in intracellular vesicles induced by receptor-mediated endocytosis.

1.2 Fluorescence methods for measuring local pH & temperature

In section 1.1, examples of the importance of proton transfer and thermal energy in various cellular processes have been discussed. Measuring pH and temperature at the cellular level will therefore provide important information about these cellular processes. Obviously, digital pH meters and thermocouples are too big to probe pH and temperature in a single cell. Instead, various molecular pH and temperature indicators have been developed in order to measure these parameters in tiny liquid volumes. Dyes, such as phenol red, have been used as a pH indicator in tissue culture for a long time. The color of phenol red changes over a range of pH from 6.8 to 8, but it is difficult to obtain quantitative pH measurements. On the other hand, fluorescent molecules have been used for quantitative pH and temperature measurements. To be used as a sensor, the fluorescence properties of these fluorophores must be sensitive to changes in pH or temperature. These environment sensitive fluorescent properties include fluorescence intensity or quantum yield, fluorescence lifetime, and the flickering due to the proton transfer of the fluorophore. By using different fluorescence techniques, one is able to exploit these properties to gauge pH or temperature.

1.2.1 Fluorescence intensity to probe pH or temperature

Probing pH or temperature by measuring fluorescence intensity is the most commonly used method. The absorption and the emission spectra of many fluorophores vary with pH or temperature. Therefore, the measured fluorescence

intensity is sensitive to either pH or temperature. These pH or temperature sensitive fluorophores can be either organic fluorophores or fluorescent proteins.

Fluorescein is one of the most common fluorescent probe and its fluorescent properties have been studied extensively [14-17]. Four different forms of fluorescein exist in aqueous solution, cationic, neutral, anionic, and dianionic, and their fractions in aqueous solution vary at different pH. Because these different forms have different fluorescent properties, the average absorption and emission spectra of fluorescein are sensitive to pH. Since fluorescein is membrane permeable, leakage has limited the use of fluorescein in confined environments such as a cell. 2',7'-bis(carboxyethyl)-5(6)-carboxyfluorescein (BCECF) has similar pH-dependent fluorescence properties as fluorescein [18], but it is membrane impermeable, and thus more useful [19, 20]. For example, Paradiso et al used BCECF to study the cytoplamsic pH of rabbit gastric glands [20]. They found that the Na^+ - H^+ exchangers on the cell membrane of the gastric gland play an important role in regulating cytoplasmic pH when the cell is exposed to a high acidity environment in the stomach.

Several fluorescent proteins, such as the green fluorescent protein (GFP) and the enhanced green fluorescent protein (EGFP), also show a pH dependence for their absorption and emission spectra due to the fact that their acidic and basic forms have different fluorescence properties [21-24]. Therefore, these proteins can be used to measure pH by determining the change in their fluorescence emission. In addition, there is a benefit to use fluorescent proteins as pH indicators for *in vivo* measurement. By using DNA cloning and transfection, the fluorescent proteins can be targeted to different cellular locations; and hence, the local pH in different cellular organelles can be measured. Works done by Keen et al and Llopis et al show that fluorescent proteins, such as EGFP, ECFP (enhanced cyan fluorescent protein), and EYFP (enhanced yellow fluorescent protein), could

be expressed in the cytosol, the mitochondria, and the golgi in mammalian cells. This allowed measuring temporal pH changes in different parts of the cell [22, 23]. On the other hand, a class of fluorescent proteins, called pHluorins, was generated using mutagenesis for the purpose of produce pH-sensitive fluorophores in samples with around neutral pH [24]. These proteins are GFP variants with higher pK_a value (~ 7), and this higher pK_a allows for a more significant change in fluorescence around physiological pH. Ecliptic pHluorin is one particular type of pHluorin that loses fluorescence gradually when the sample pH decreases. It was used for example to measure the pH in the synaptic vesicles [25].

Compared to fluorescent pH indicators, there are fewer examples of molecular temperature indicators using fluorescence emission as a gauge. Rhodamine B is one example of molecular thermometer. The emitted fluorescence is sensitive to temperature due to a strong temperature dependence of its quantum yield [26]. By measuring the fluorescence emission of rhodamine B, Kato et al showed that increasing temperature can increase the sliding velocity and force of actomyosin motors [27]. In addition, rhodamine B has been used to characterize the temperature profile in microfluidic devices with electroosmotic flow due to Joule heating [28, 29]. Another temperature sensitive fluorophore, tris(2,2'-bipyridine)ruthenium(II), has been used to perform thermal imaging using two-photon microscope in a sample with a heat source [30]. tris(2,2'-bipyridine)ruthenium(II) can fluoresce over a wide temperature range, from -196 to 100°C [31], and both of its quantum yield and fluorescence lifetime show a strong temperature dependence in the range 0 - 100°C. Rather than using the temperature dependence of quantum yield, Gota et al developed a new kind of molecular thermometer. Their molecular thermometer, called fluorescent nanogel thermometer **1**, contains a thermally sensitive polymer as the shell with water sensitive fluorophores in the interior [32]. At lower temperature, the nanogel swells and water molecules are absorbed into the interior. Then, the water

molecules quench the fluorophores and promote a drop in fluorescence intensity. At higher temperature, the polymer shell shrinks and the effect is reversed. In addition, it was created to contain a highly hydrophilic surface; consequently, it is suitable for temperature measurements in biological samples.

There are some advantages in using fluorescence intensity to gauge pH or temperature. First, this measurement method is very easy to integrate with other fluorescence imaging techniques. Once a pH or temperature calibration is obtained, the sample pH and temperature can be determined from the fluorescence images. Also, this method can measure rapid pH and temperature changes, because the temporal resolution of the experiment only depends on the temporal resolution of the photodetector. However, the accuracy of this type of measurements is very sensitive to the experimental setup and to the sample preparation. Only a slight change in the alignment of the microscope or in the fluorophore concentration during sample preparation can lead to a significant change in measured fluorescence intensity. Consequently, this method is suitable to determine relative changes in pH or temperature, but not absolute pH or temperature.

1.2.2 Ratiometric fluorescent pH indicators

The ratiometric approach to measure pH is an improvement over the intensity-based method. In this approach, ratiometric fluorophores are used as a probe to measure pH. This type of fluorophores has different excitation or emission maxima at various pH. In many cases, the spectral changes are due to the coexistence of protonated and deprotonated forms of the fluorophore, and each form has a different excitation or emission maxima. The ratiometric approach consists in determining the ratio of fluorescence signals measured for each of the excitation (or emission) maxima. For ratiometric fluorophores with

excitation spectral difference, the ratio of emitted fluorescence can be determined by exciting the fluorophores with two excitation maxima. On the other hand, for fluorophores with emission spectral difference, one can determine the ratio of fluorescence at the two emission maxima by using a single excitation wavelength.

Pyranine is a well-studied ratiometric fluorescent molecule with excitation spectral difference. The protonated and deprotonated forms of pyranine have different absorption maxima; 400 nm for the protonated state and 450 nm for the deprotonated state. A lowering in pH increases the absorption at 400 nm and decreases the absorption at 450 nm, while a raise in pH has the opposite effect on the two absorption wavelengths. The ratio of fluorescence measured for a 450 nm excitation to that measured for a 400 nm excitation (F_{450}/F_{400}) is therefore sensitive to pH. Alternatively, one can determine the ratio of fluorescence obtained for 450 and 415 nm excitations (F_{450}/F_{415}), where 415 nm is the isosbestic wavelength of pyranine [33]. Pyranine has been used to measure pH inside liposomes with the ratiometric method *in vitro* [34] and *in vivo* [35]. Also, by integrating the ratiometric approach with fluorescence imaging, pyranine has been used to investigate the acidity of endosomal vesicles at various locations in neurons [36]. Another example of ratiometric fluorophore as pH sensor is the ratiometric pHluorin. This protein is a GFP mutant with absorption maxima at 395 nm and 475 nm, and the fluorescence ratio obtained at the two maxima is sensitive to pH [24, 37]. Orij et al applied the ratiometric pH imaging using pHluorin as a probe to study the cytosolic and mitochondrial pH in growing yeast cells [37]. Compared to intensity-based pH measurements, the advantage of the ratiometric method is that the fluorescence ratio is not sensitive to fluorophore concentration or fluorescence collection and detection efficiency. Consequently, slight changes in experimental setup alignment and fluorophore concentration (for example due to photobleaching) do not influence the pH measurement significantly. The ratiometric approach can also be used to monitor the

concentration of Ca ion [38], Zn ion [39], or H_2O_2 [40], as well as O_2 pressure [41].

1.2.3 Fluorescence lifetime

Other than fluorescence intensity, the fluorescence lifetime can be applied to gauge pH and temperature. Fluorescence lifetime, τ, is the decay rate of fluorescence due to the spontaneous emission from the fluorophore. The decay of fluorescence after a pulse excitation can be described by single or multiple exponential decays:

$$I = \sum_i A_i \cdot \exp\left(-t/\tau_i\right)$$

A_i are the pre-exponential factors and the fluorescence lifetimes (τ_i) can be measured either using time domain or frequency domain methods [42]. Work done by Sanders et al indicate that the fluorescence lifetime of carboxyl SNAFL-1 is sensitive to pH [43]. They stained CHO cells with carboxyl SNAFL-1, and applied fluorescence lifetime imaging microscopy (FLIM) to obtain a pH image of the cells. Also, Hille et al applied FLIM to obtain pH images of BCECF-loaded cockroach salivary duct [44]. tris(2,2'-bipyridine)ruthenium(II) [31], the fluorescent membrane probe NBD [45], and rhodamine-G [46] are examples of fluorophores with temperature dependence of the fluorescence lifetime. By using these fluorescent probes, temperature images could be obtained using FLIM.

As for the ratiometric approach, the advantage of using fluorescence lifetime to probe pH or temperature is that the fluorescence lifetime is not sensitive to fluorophore concentration or photobleaching. As a result, this method can provide a more accurate quantitative measurement compared to intensity-based method. In addition to pH and temperature, the fluorescence lifetime of fluorophore is sensitive to other environmental conditions such as ion concentration [42, 47] and conformational change of the protein [48]. Since the

fluorescence lifetime depends on many different environmental conditions, a thorough calibration study should be conducted before *in vivo* pH or temperature measurement. Also, lifetime measurement and FLIM require expensive instrumentation, so this limits the popularity of this method for pH and temperature measurements.

1.2.4 pH measurement based on fluorophore blinking

Many fluorescent pH indicators, such as BCECF, EGFP, and pyranine, exist as an equilibrium between a protonated form and a deprotonated form with different excitation maxima, and they continuously go through a reversible protonation process. When one form of the fluorophore can be selectively excited, blinking of the fluorescent molecule is observed. Fluorescence correlation spectroscopy (FCS) is a perfect tool to detect the fluorescence fluctuations emitted by fluorophores in a sample [49, 50]. By using FCS, one obtains an autocorrelation function that reflects the different fluorescence fluctuations detected in a small confocal volume. The fluorescence fluctuations are usually due to the diffusion of fluorophores across the confocal volume, but these can also be the result of fluorophore blinking. A detailed description of FCS can be found in Appendix A. After analyzing the autocorrelation function, one can obtain the ratio of fluorophores in fluorescent and nonfluorescent states (different forms) and the relaxation time associated with the blinking. Previous studies have shown that the blinking of FITC, EGFP, and ecliptic pHluorin is sensitive to pH, and the parameters of the blinking as described by FCS were used to probe pH [51, 52]. The advantages of this method are related to the robustness of the blinking measurement when using FCS. In addition, only a low concentration of fluorophore is needed in FCS measurements. Therefore, the potential influence of high fluorophore concentration to different cellular processes during *in vivo* measurement can be avoided. In addition to pH dependence, chapter 2 and 3 will

describe my own FCS investigation on the temperature dependence of the reversible protonation processes of EGFP and pyranine.

1.3 Fluorescent biosensors

All the methods introduced in section 1.2 are based on measuring the fluorescence properties of various environment sensitive fluorophores. In this thesis, I will describe two pH and temperature measurement methods, where two environmentally sensitive fluorophores, EGFP and pyranine, were used. In the rest of this section, the structure, chemical, and fluorescent characteristics of EGFP and pyranine are introduced before going into the details of the measurement methods.

1.3.1 Enhanced green fluorescent protein

EGFP is a mutant of the natural fluorescent protein GFP originally extracted from the jellyfish Aequorea victoria. GFP was discovered together with aequorin, a blue light emitting protein in the presence of Ca^{2+} [53]. Later, it was discovered that the green light emission of the jellyfish is due to the fluorescent resonance energy transfer (FRET) between aequorin and GFP. GFP contains two excitation maxima, a major peak at 395 nm and a smaller absorption maximum at 470 nm at physiological pH. Also, the maximum fluorescence emission for GFP is in the range 503 – 508 nm (reviewed in ref. [54]).

After the successful cloning of the GFP cDNA [55], GFP variants were created first by random mutations, and later by site-directed mutations. One major green light emitted mutant of GFP is EGFP. EGFP is also referred to as GFP-F64L/S65T. Basically, two amino acids of GFP were replaced, Phe64 to Leu and Ser65 to Thr [56]. The mutation from serine to threonine shifts the absorption

frequency from 395 nm to around 488 nm in physiological conditions [56]. On the other hand, the mutation of phenylalanine to leucine improves the bacterial expression of the GFP mutants. In addition, these mutations do not significantly change the emission maximum (507 nm). The mutations of EGFP lead to several major improvements over the wild type GFP. First, the red-shift of the major absorption peak to 488 nm allows the excitation of EGFP using an argon-ion laser. This switch from UV to visible light excitation reduces photodamage and autofluoresce. Furthermore, the fluorescence of EGFP is 35 times that of the wild-type GFP at 488 nm excitation [56]. Consequently, EGFP can be regarded as an improved version of GFP.

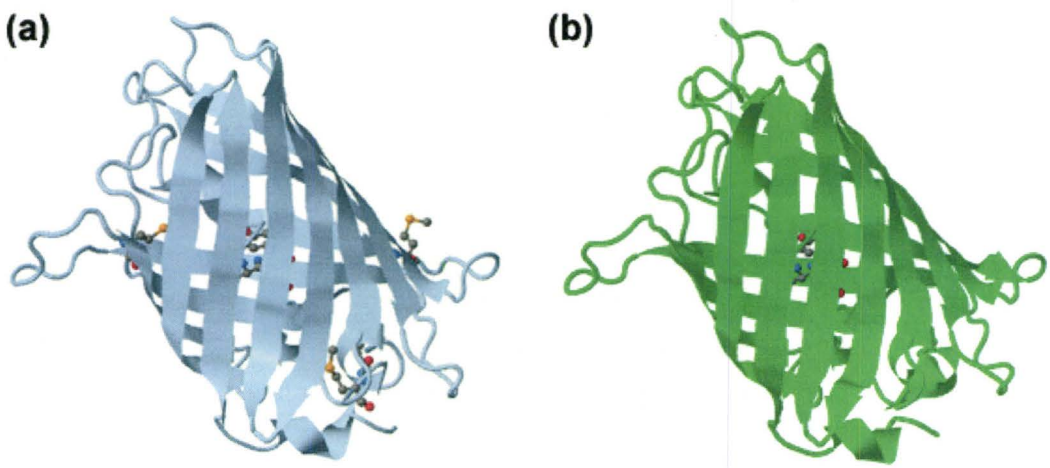

Figure 1.2. Crystal structure of (a) wild type GFP [57] and (b) GFP mutant S65T [58]. The structures were obtained from the RCSB Protein Data Bank (a) 1ema and (b) 1c4f.

EGFP is a 29 kDa monomer with 265 amino acids (data from BioVision, Inc.). The shape of the wild type GFP resembles an open-end cylindrical can. The crystal structure of GFP shows that there are 11 strands of beta sheets forming an antiparallel barrel, and the chromophore is hidden at the center of it [59]. The S65T GFP mutant shows a very similar crystal structure to that of the wild type

[57]. In fact, all studied GFP mutants show a similar barrel shape with minor differences in the overall structure. Therefore, it is likely that EGFP has the same shape as the wild type GFP. The diameter of the wild type GFP and other GFP mutants is roughly 30 Å and about 40 Å in length [57, 59]. The chromophore of EGFP consists of three amino acids, threonine, tyrosine and glycine. The hydroxyl group in the tyrosine of EGFP chromophore undergoes continuous protonation / deprotonation, and the proton transfer changes the conformation of the chromophore. As a result, it alters the absorption maxima of the protonated and the deprotonated forms of EGFP [50]. Wild type GFP has been shown to denature at temperature above 65°C or in solution with pH less than 4 or greater than 12 (reviewed in ref. [54]). Similar to the wild type, EGFP begins to denature at temperature ~ 65°C [60]. In addition, it has been reported that the fluorescence emission of EGFP decreases drastically at pH below 4 or higher than 12 [50].

GFP was immediately recognized as a useful fluorescent reporter *in vivo* after it was first expressed in both prokaryotic and eukaryotic cells [61]. Since then, GFP and its variants have been used in a range of different studies in molecular cell biology. Among all GFP mutants, EGFP is the most commonly used fluorescent proteins due to its strong fluorescence emission. A recent transgenic study showed successful expression of EGFP transgene in the somatic cells of primates [62]. Since the genetic information between human and primate is very similar, this study is a significant achievement in biomedical research, demonstrating the feasibility of human gene therapy. In the previous section, I have discussed the use of EGFP as fluorescent pH indicator. In addition to its usefulness as a molecular pH meter, I will show in this thesis that EGFP can be used as a molecular thermometer (Chapter 2) [63].

1.3.2 Pyranine

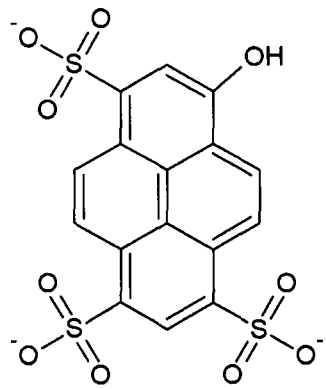

Figure 1.3. Structure of pyranine (1-hydroxypyrene-3,6,8-trisulfonic acid). The hydroxyl group of pyranine undergoes protonation/deprotonation.

Pyranine, 1-hydroxypyrene-3,6,8-trisulfonic acid or HPTS, is a pH sensitive organic fluorescent dye [34, 64]. Compared to EGFP, pyranine is a simpler fluorophore, with roughly 524 daltons in molecular weight. The hydroxyl group of pyranine can undergo a reversible protonation reaction. As mentioned previously, pyranine has two excitation maxima. Each excitation maximum represents the absorption of a different anionic form of pyranine, the protonated (400 nm) and the deprotonated form (450 nm). The absorbance of each peak varies with pH: the absorbance at 400 nm decreases with increasing pH and vice versa for the peak at 450 nm [34, 35, 44, 64]. On the other hand, pyranine has only one emission maximum at around 510 nm.

Pyranine possesses various characteristics that make it a good fluorescent pH indicator in biological sample at physiological pH (7.4). At physiological ionic strength, pyranine has a pK_a value of approximately 7.3 [34, 64]. This leads to a significant change in fluorescence with only small pH change at physiological pH. Since pyranine has three sulfonate groups, it remains ionized over a wide range of pH. Therefore, pyranine molecules are highly polar, and hence have a good

solubility in water [64]. The strong hydrophilicity also causes pyranine to be membrane impermeable. In addition, pyranine has a very low toxicity in the concentration range that is suitable for fluorescence microscopy [65].

In section 1.2.2, I have already discussed several applications of pyranine for ratiometric pH imaging. Other than using pyranine as a molecular pH indicator, pyranine is widely used as a photoacid to study proton transfer in acid-base reactions [66-71]. Photoacids are molecules that are significantly more acidic in the excited state than in the ground state, so they undergo more rapid deprotonation upon photoexcitation. In these proton transfer studies, the protonated form of pyranine is the photoacid and the deprotonated form is the conjugate base. By monitoring the temporal change in the absorbance of the sample using IR spectroscopy, the mechanisms of the proton transfer in the acid-base reaction were investigated because the protonated and the deprotonated states of pyranine have unique absorption wavelengths. And since the proton transfer of the photoacid is rapid in the acid-base reaction, IR spectroscopy can also monitor the change in the water molecules such as the stretching of the OH bond and the bending of the molecules, as well as the vibration of the hydrogen bonds during the acid-base reaction of pyranine. Consequently, it provides insights on the role of water molecules and hydrogen bonds during the acid-base reaction.

In chapter 3, I will show my investigation of the temperature dependence of the reversible protonation of pyranine using FCS. In addition, I will describe how various ions and ionic strength affect the reversible protonation of pyranine. Finally, the pH of endosomal vesicle was studied using the ratiometric pH imaging of pyranine obtained by two-photon excitation microscope. Both the methods and the results of this study will be discussed in chapter 4.

Chapter 2

A Molecular Thermometer Based on the Blinking of EGFP

2.1 Introduction

Thermal energy is an important source of energy in cells. Many animals can only survive in a narrow temperature range, so they have developed their own mechanisms to produce and to dissipate heat. In addition, thermal energy can drive various cellular reactions, which have been briefly discussed in chapter 1. Therefore, measuring the amount of thermal energy involved in a cellular reaction can give us an insight on how the reaction is driven thermodynamically. On the other hand, many non-invasive experimental techniques could potentially induce temperature increase in the sample. For example, optical tweezers can produce heat at the laser focus by light absorption of the infrared photons [72]. Since the laser induced heating may influence the results of studies and also may damage the samples, it is necessary to quantify the temperature change at the laser focus beforehand.

In the previous chapter, I have introduced several temperature measurement methods which are based on the measurement of temperature sensitive properties of fluorophores. The most common temperature measurement

method is to determine the temperature sensitive fluorescence emission intensity of fluorophores such as rhodamine B. However, using fluorescence intensity to gauge temperature does not permit accurate quantitative measurements, because local dye concentration and background signal have a strong influence on the fluorescence detection. To resolve this problem, I proposed another approach relying on the detection of EGFP blinking, and this method allows absolute temperature measurements unlike the intensity-based methods. The EGFP blinking is due to a reversible protonation reaction at the EGFP chromophore as discussed briefly in section 1.3.1. Since blinking leads to fluctuations of the fluorescence, the relaxation of this blinking process can be measured by FCS. In this chapter, I start by reporting my investigation of the temperature dependence of the EGFP blinking using FCS. Then, I describe how the EGFP blinking can be applied to temperature measurements. Finally, to demonstrate the feasibility of this approach, I present measurements of the temperature change at a laser focus due to light absorption by the sample as a first application for this method.

2.2 Materials and Methods

2.2.1 Sample preparation

CP buffer is composed of 10 mM citric acid (Anachemia Science, Montreal, Canada) and 100 mM potassium phosphate monobasic (EM Science, Darmstadt, Germany) [50]. Variants of CP buffer were also prepared and they are supplemented with 100 g/l of bovine serum albumin (BSA, BioShop, Burlington, Canada) plus different concentrations of sodium copper chlorophyllin, 0, 2.5, or 5 g/l (SCC, Sigma-Aldrich, St. Louis, MO, U.S.A.). SCC is a derivative of chlorophyll with absorption maxima at 400 and 633 nm. Addition of BSA in the CP buffer can reduce the aggregation of SCC at low pH. To adjust sample pH, either HCl or NaOH was added to the sample, and the pH was monitored with a digital pH meter.

Purified EGFP was purchased from BioVision (Mountain View, CA, U.S.A.) and a 1 g/l concentration stock solution was prepared in phosphate buffered saline (PBS, pH 7.4, BioShop, Burlington, Canada). For FCS measurements, the stock EGFP was diluted in CP buffer or CP buffer variants to concentration ranging from 70 – 700 nM. Other than pure EGFP, I also studied the blinking of EGFP fused to Bax (provided by Dmitri Satsoura), and the fusion protein was diluted in CP buffer as well. Each liquid sample was injected into a sample chamber, which is made of two cover slips (18 x 18 mm & 24 x 40 mm) with Parafilm as spacers. The opening of the sample chamber is sealed with wax after injecting the liquid sample. Roughly 10 μl of liquid can be held in the sample chamber, and the thickness of the liquid sample is around 100 μm. The home-built FCS system gives the possibility to control sample temperature with an inverted microscope stage temperature control system (PE-100NI, Linkam Scientific,

Surrey, UK) and a custom water immersion objective temperature control (Linkam Scientific, Surrey, UK).

2.2.2 Analysis of the autocorrelation function

A description on the basic concept and the experimental setup of the fluorescence correlation spectroscopy (FCS) are presented in Appendix A. A continuous reversible protonation reaction at the EGFP chromophore leads to an observable blinking of the protein with 488 nm laser excitation (50 μW except specified). In this case, only the deprotonated form of EGFP fluoresces. For EGFP, the fluorescence fluctuations obtained in FCS are the results of EGFP diffusion across the observation volume and of the blinking due to the reversible protonation of EGFP. As a result, the autocorrelation functions obtained from EGFP sample show two characteristic decays, and they can be analyzed using the following expression (see Appendix A) [50]:

$$G(\tau) = \frac{1}{N} \cdot \frac{1}{\left(1 + \tau/\tau_D\right)\sqrt{1 + \tau/S^2\tau_D}} \left[1 + \frac{B}{1-B} \cdot \exp\left(-\frac{\tau}{\tau_B}\right)\right] \qquad (2.1)$$

N is the average number of fluorophores in the detection volume. τ_D is the average residence time of the fluorophores in the detection volume. S is the aspect ratio of the detection volume, and it is determined experimentally using a standard dye, fluorescein (see Calibration of Observation Volume in Appendix B). B is the fraction of fluorophore in the protonated dark state. τ_B is the relaxation time associated with the EGFP blinking. Since I analyzed the autocorrelation functions only for lag time above 10 μs, I could ignore the fluctuation of the fluorescence emission due to triplet transition of EGFP, which occurs at lag time on the order of a few microseconds.

By definition, the equilibrium constant of the reversible protonation reaction of EGFP can be expressed as:

$$K = \frac{1}{10^{-pH}} \cdot \frac{B}{1-B} \tag{2.2}$$

Furthermore, the equilibrium constant, K, and the blinking relaxation time, τ_B, are expected to vary as a function of temperature according to the Arrhenius equation:

$$\ln(K) = -\frac{\Delta E}{R} \cdot \frac{1}{T} + \ln\left(\frac{A_p}{A_d}\right) \tag{2.3}$$

$$\frac{1}{\tau_B} = 10^{-pH} \cdot A_p \exp\left(-\frac{E_p}{RT}\right) + A_d \exp\left(-\frac{E_d}{RT}\right) \tag{2.4}$$

$\Delta E = E_p - E_d$. E_p and E_d are the activation energies of protonation and deprotonation respectively. A_p and A_d are the frequency factors of protonation and deprotonation respectively. R is the gas constant. The derivations of Eqs. (2.2) to (2.4) are detailed in Appendix C.

In each experimental condition, at least five measurements were taken. Depending on the molecular brightness of the fluorophore, which varies due to a number of factors and correlates with the signal-to-noise ratio, the time duration of a single measurement varied between 10 and 120 seconds. The data analysis software Kaleidagraph (Synergy Software, Reading, PA) was used to plot the autocorrelation functions and they were analyzed using the integrated curve fitting function of the software. This function returns values for the different variables and their corresponding fitting errors. Afterward, the average values of N, B, and τ_B were calculated, and their associated errors estimated as the largest value of the standard deviation and the fitting errors from each measurement. Therefore, the errors of the average values are either the variation of data from the sample mean or the scatter of the autocorrelation function compared to the best fit line. The values of ln(K) were calculated from the average values of B using Eq. (2.2), and the errors were calculated using error propagation. In addition, the concentrations of fluorophore in different samples were calculated from the average values of N.

2.3 Results

2.3.1 Autocorrelation of EGFP

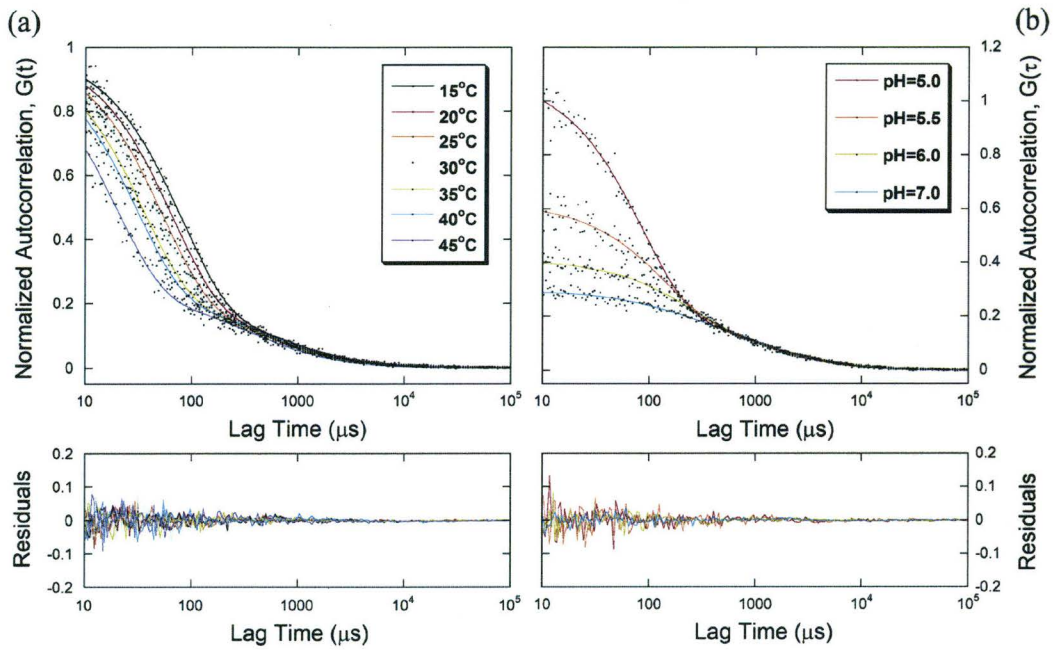

Figure 2.1. (a) Autocorrelation functions of EGFP in CP buffer (pH = 5) at various temperature and residuals corresponding to the fits. (b) Autocorrelation functions of EGFP in CP buffer at various pH (T = 20°C) and residuals corresponding to the fits.

The autocorrelation functions obtained from FCS measurements reflect the fluctuations of fluorescence emitted by the fluorophores in the confocal detection volume. The autocorrelation functions of EGFP in CP buffer (pH = 5) at different temperatures are shown in Figure 2.1a. At lag time above 10 μs, the autocorrelation function of EGFP in CP buffer shows only two distinct characteristic decays. Haupts et al found that the characteristic decay at the faster time scale, at lag time ~ 100 μs, represents the blinking of EGFP due to a protonation / deprotonation at the chromophore [50]. The other characteristic decay of the autocorrelation function is due to the diffusion of EGFP across the

detection volume. Further, I obtained the autocorrelation functions of EGFP in CP buffer at various pH at room temperature, and the results are shown in Figure 2.1b. The results indicate that the blinking terms of the autocorrelation functions vary with pH and temperature. So, the protonation / deprotonation of EGFP is sensitive to pH and temperature as predicted by Eq. (2.3) & (2.4). The autocorrelation functions in Figure 2.1 were analyzed using Eq. (2.1) in order to obtain the average values of B and τ_B. Figure 2.1 also illustrates the residuals corresponding to the fitting of the autocorrelation functions.

2.3.2 EGFP as a thermometer: kinetics of the reversible protonation reaction

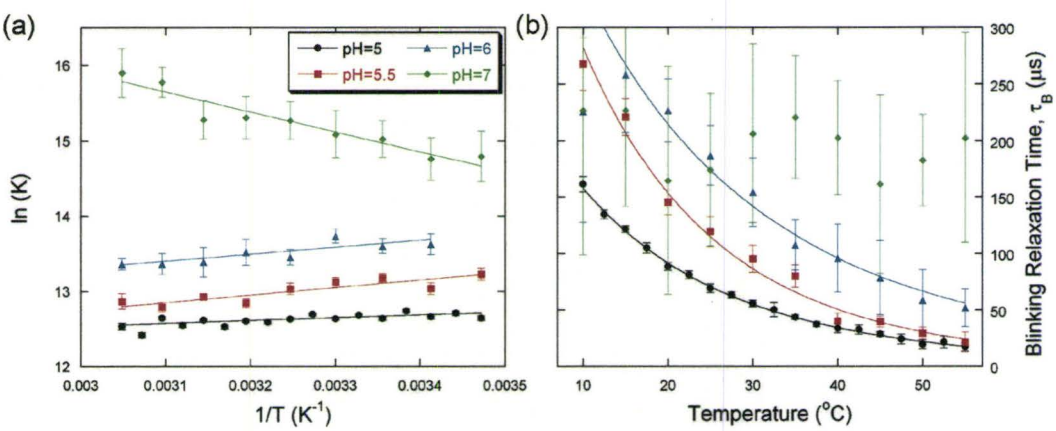

Figure 2.2. (a) Natural logarithm of the equilibrium constant, ln(K) as a function of the inverse temperature, and (b) the blinking relaxation time as a function of temperature for the reversible protonation process of EGFP in CP buffer at pH = 5, 5.5, 6, & 7.

From the average values of B obtained for various pH and temperatures, the equilibrium constant of the reversible protonation reaction of EGFP, K, was calculated using Eq. (2.2). Figure 2.2a shows ln(K) as a function of the inverse temperature for EGFP in CP buffer at various pH. Each data set on Figure 2.2a was analyzed using Eq. (2.3) to obtain ΔE and A_p/A_d. The results in Figure 2.2a indicate that ln(K) increases when sample temperature is decreased ($\Delta E < 0$),

except for pH = 7 ($\Delta E > 0$). In addition, the error on ln(K) increases with increasing pH.

Table 2.1. Average measured values for the thermodynamic parameters corresponding to the reversible protonation of EGFP in CP buffer at different pH. The errors corresponds to the standard deviation of a set of five measurements.

Thermodynamic parameters	pH = 5.0	pH = 5.5	pH = 6.0	pH = 7.0
A_p (/fs)	7.1±4.2	5.4±6.5	0.27±0.22	
A_d (/ns)	14±11	310±430	1.5±1.9	
E_p (kcal/mol)	9.2±0.3	9.0±1.1	6.7±0.5	
E_d (kcal/mol)	10.3±0.5	10.4±1.9	7.2±1.3	
ΔE (kcal/mol),	-1.1±0.1	-1.4±0.8	-0.6±1.8	5.3±1.4

Figure 2.2b shows the blinking relaxation time, τ_B, as a function of temperature for EGFP in buffer at various pH. Each data set was analyzed using Eq. (2.4). The results shown in Figure 2.2b demonstrate that the blinking relaxation time of EGFP is very sensitive to temperature at pH $\leq$6. The error on τ_B increases with increasing sample pH, similar to what is observed for ln(K). By using the values of ΔE and A_p/A_d found in Figure 2.2a, the values of A_p and E_p were determined using Eq. (2.4) to analyze Figure 2.2b, and finally, the values of A_d and E_d were calculated. The measured thermodynamic parameters at different pH are tabulated in Table 2.1. The results indicate that the values of the activation energies, E_p and E_d, are constant within error at low pH (pH $\leq$5.5, $E_p = 9.2 \pm 0.3$ kcal/mol and $E_d = 10.3 \pm 0.5$ kcal/mol).

Because of the strong temperature dependence of the blinking relaxation time, it is therefore a useful parameter to exploit for temperature measurements. The function giving τ_B versus temperature uniquely relates each measured value

of τ_B to an absolute temperature for a given pH, and can therefore be used as a temperature calibration curves for EGFP at different pH (Eq. (2.4) with corresponding thermodynamic parameters).

2.3.3 *Influences of various parameters on the temperature measurement*

To investigate the robustness of the blinking measurement, first, I investigated the effect of excitation laser power on the blinking relaxation time and the result is shown on Figure 2.3. At laser power > 100 μW, there is a gradual decrease of the blinking relaxation time, and it may be due to the emergence of a characteristic decay for the triplet transition on the autocorrelation function that is not accounted for in the fit. For laser powers used in FCS experiments (< 100 μW), however, the measurement of τ_B is stable. Also, the error of the measurement is more significant at low laser power (< 50 μW). So, the optimal laser power for measuring EGFP blinking is 50 – 100 μW. In addition, I determined the thermodynamic parameters from calibration curves recorded at various laser powers and the results are tabulated on Table 2.2. The results indicate that the thermodynamic parameters are in good agreement at various laser powers.

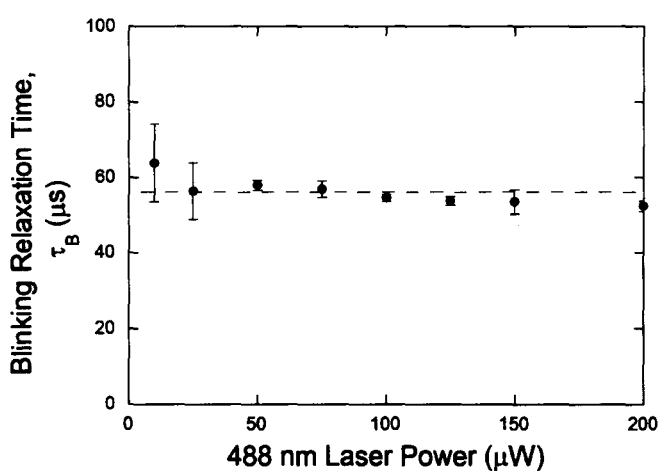

Figure 2.3. Blinking relaxation time as a function of excitation laser power for EGFP in CP buffer (pH =5). All measurements shown were taken at 30°C.

Table 2.2. Average thermodynamic parameters for the reversible protonation process of EGFP measured by FCS using different excitation laser powers. The errors are the standard deviation from different measurements.

Thermodynamic parameters	Laser power			
	20 μW	50 μW	200 μW	500 μW
A_p (/fs)	7.1±4.2	6.0±2.0	7.2±0.9	7.0±4.3
A_d (/ns)	14±11	25±11	9.0±1.5	15±11
E_p (kcal/mol)	9.2±0.3	9.1±0.2	9.1±0.1	9.0±0.2
E_d (kcal/mol)	10.3±0.5	10.6±0.3	10.0±0.1	10.3±0.3
ΔE (kcal/mol)	-1.1±0.1	-1.52±0.06	-0.9±0.1	-1.28±0.09

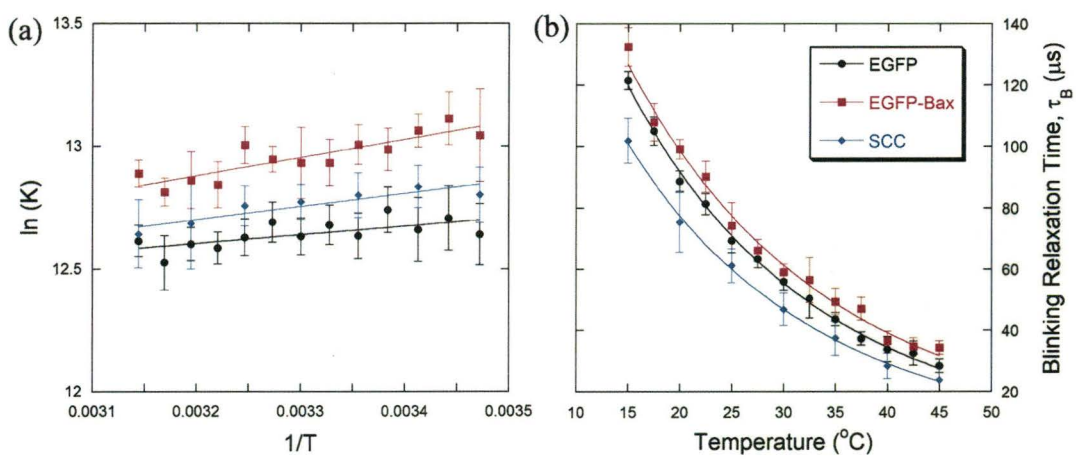

Figure 2.4. (a) ln(K) against inverse temperature, and (b) the temperature calibration curves of pure EGFP (black), fusion of EGFP and Bax (red), and EGFP in CP buffer supplemented with 5 g/l SCC and 100 g/l BSA (blue). All samples were in CP buffer at pH = 5.

Further on, I investigated how the buffer composition affects the temperature calibration curve. In addition, I investigated the temperature

dependence of the blinking of an EGFP fusion to the protein Bax. The autocorrelation functions were obtained from samples with 1) fusion protein of EGFP and Bax in CP buffer, and 2) EGFP in CP buffer supplemented with 100 g/l BSA and 5 g/l SCC. After the analysis, I plotted ln(K) versus 1/T (Figure 2.4a) and the temperature calibration curves (Figure 2.4b) for these samples. In general, the blinking relaxation time, τ_B, is still sensitive to temperature change for the EGFP fusion protein, and for EGFP in different solutions. There is a similar decrease in the blinking relaxation time with increasing temperature for all three samples, even though they are not in perfect agreement.

2.3.4 *Effect of using air and water immersion objectives on the blinking measurement*

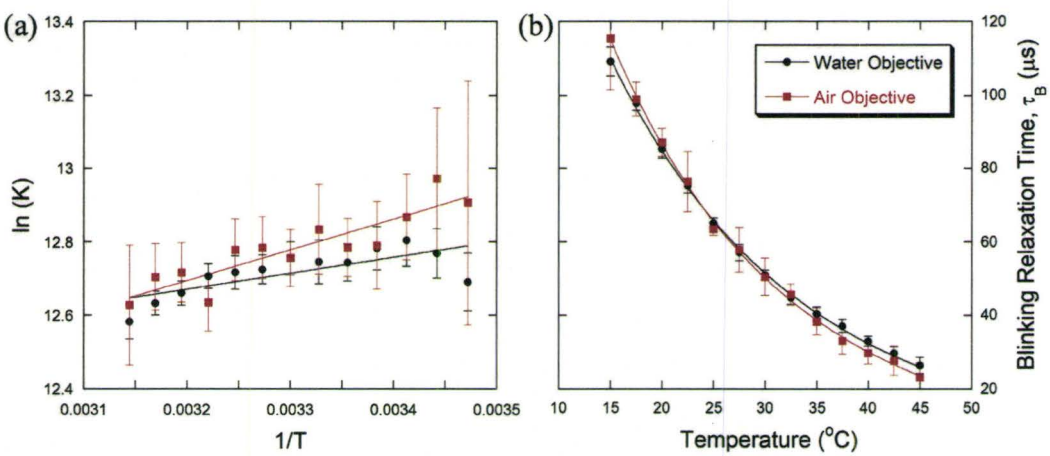

Figure 2.5. (a) ln(K) versus the inverse of temperature, and (b) the temperature calibration curves of EGFP obtained by the air- and water-immersion objectives (pH = 5).

Water and oil immersion objective lens act like a heat sink for the sample, because both of them have a physical contact with the sample chamber [73]. Therefore, it is desirable to use an air immersion objective, which has no physical contact with the sample, to avoid any artifact in temperature measurements. In

addition to physical contact, there are other differences between measurements using air or water immersion objectives. The air- and water-immersion objectives used for this study had different numerical aperture, 60x air-immersion objective with NA = 0.95 and 60x water-immersion objective with NA = 1.2. The difference in numerical aperture leads to a difference in the size of the diffraction limited laser focus, and hence, different sizes of the detection volume. Using calibration with a dye (see Appendix B), the detection volume of the air objective was determined to be 0.49 μm in radius and 1.86 fl in volume when the 488 nm laser was used. On the other hand, with the same laser beam, the radius of the detection volume is 0.39 μm and 1.65 fl in volume for the water objective. The study of the EGFP blinking using different objectives can provide some insight on the effect of the detection volume size on the blinking measurement. Figure 2.5 illustrates ln(K) versus 1/T and the calibration curves for pure EGFP in CP buffer (pH = 5) obtained using different objectives. The calibration curves indicate that the values of τ_B agree with each other over the whole temperature range. In addition, the values of ln(K) from the two data sets agree with each other as well.

2.3.5 Application: Temperature measurement at laser focus using EGFP

As a first application of our method, EGFP was used to characterize the heating at a laser focus due to the light absorption in a thin liquid sample. In this part, a commercial FCS instrument was used for the measurements. This system allows dual colour irradiation at the same spot in the sample. A 637 nm laser beam was used to induce light absorption from a chlorophyll derivative, SCC, dissolved in the sample. On the other hand, a second laser beam with a 488 nm wavelength was used to excite EGFP (~ 80 μW). First, I measured the temperature change at the laser focus when it was located far away from the cover slip surface. The theoretical prediction of the heating at the laser focus due to light absorption has been done by Peterman et al [72]. They predicted that the temperature change

due to light absorption at the laser focus away from the glass surface can be described as, $\Delta T \approx \varepsilon P / K$, where P is the laser power, and ε and K are the extinction coefficient and thermal conductivity of the liquid sample respectively. The measured temperature shown in Figure 2.6 indicates that there is no temperature change without SCC in the sample. On the other hand, in the presence of SCC, the temperature increases linearly with the increase in 637 nm laser power. In addition, the inset of the figure illustrates that the temperature increases linearly with increasing SCC concentration. Both the effects of laser power and SCC concentration agree with the theoretical prediction of laser induced heating.

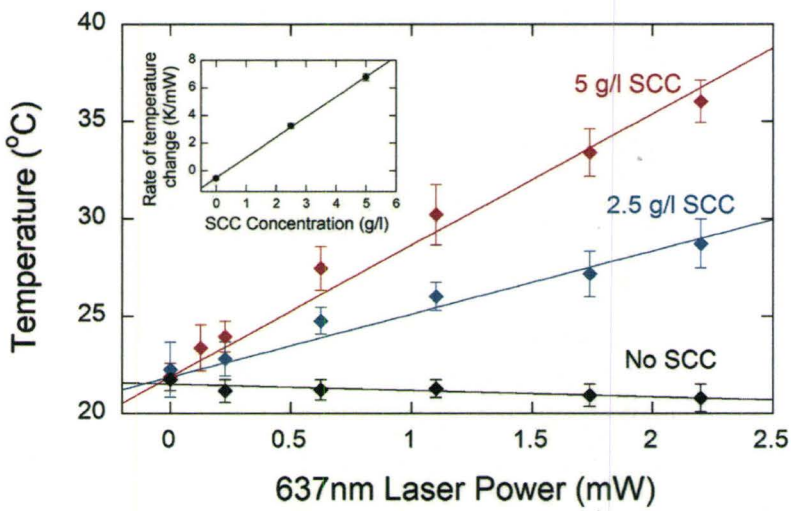

Figure 2.6. Increase in temperature at the focus of a 637 nm laser beam for solutions containing different concentrations of SCC. Lines represent linear fit of the data. (Inset) The average rate of temperature changes as a function of SCC concentration.

The theory by Peterman et al also predicts that the temperature change at the laser focus should vary as the laser focus is moved away from the surface of the sample chamber. The difference in temperature change is due to faster heat dissipation at the boundary of the sample, because the thermal conductivity of

glass is higher than that of water. To investigate the distance effect of temperature change, temperature measurements were taken at different focal planes above the glass surface and the results are shown in Figure 2.7. Without the red laser beam illumination, there is no temperature change at the laser focus as expected. When the 637 nm laser beam illuminated the sample, the result shows a steep temperature change as one moves away from the glass surface. However, the temperature measurement and the theoretical prediction are not in agreement. The measured temperatures are higher than the theoretical predictions at various focal planes. Also, the measured temperature reaches a saturated temperature at a shorter distance.

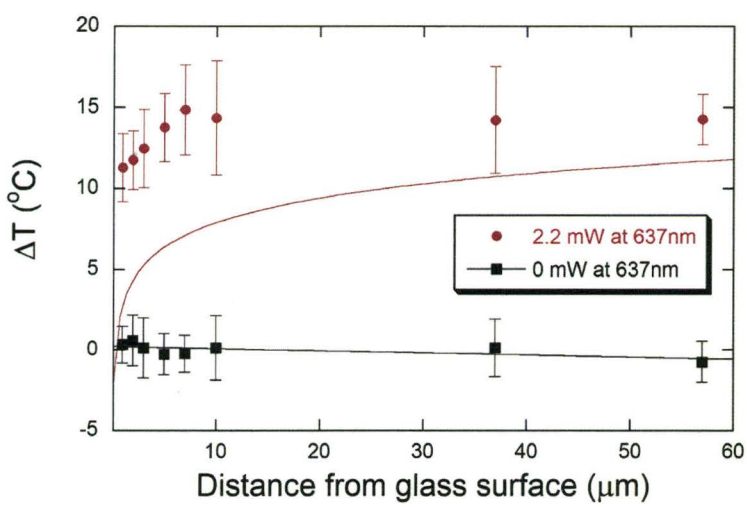

Figure 2.7. Temperature change at the laser focus in a 5 g/l SCC solution as a function of the distance between the laser focus and the glass cover slip, in the presence and in the absence of the 637 nm laser radiation. Solid lines are theoretical predictions from ref. [72] ($\varepsilon = 35\ cm^{-1}$, $K = 5.86\ W \cdot K^{-1} \cdot cm^{-1}$).

2.4 Discussion

The temperature measurement method described in this chapter utilizes the fact that the EGFP blinking is sensitive to temperature. At lower pH (pH $\leq$ 5.5), the relaxation time associated with the blinking of EGFP has a strong temperature dependence. In addition, the error on the measurement is low at this pH. Therefore, the blinking relaxation time can be used as a parameter to gauge temperature. My investigations of EGFP blinking also show that the blinking of EGFP is sensitive to pH and buffer composition. In order to perform an accurate temperature measurement, it is thus necessary to obtain a new temperature calibration curve at each pH and for each buffer composition. The calibration curves in Figure 2.4 indicate that temperature measurement without a proper calibration curve can easily lead to an error up to 5°C.

The temperature calibration curves obtained at various pH indicate that the error on the relaxation time τ_B increases with increasing sample pH. When the pH is increased above the pK_a, the fraction of EGFP in the protonated dark state, B, begins to decrease. So, the contribution of the term due to blinking in the autocorrelation function becomes small at pH > pK_a, and this leads to larger fitting error for the blinking term. In addition, the two characteristic decays of the autocorrelation functions at higher pH became more difficult to distinguish due to the increase in blinking relaxation time; hence, it introduces a larger fitting error on the measured values of the blinking term. At pH = 7, the result indicates that the blinking relaxation time appears to be independent of the temperature change, and this may be due to the large data scattering at pH = 7. Another possible explanation is due to the possibility of more complex protonation / deprotonation at the chromophore of EGFP. The enthalpy change obtained at pH = 7 is clearly positive. On the contrary, the enthalpy changes measured at pH $\leq$ 6 were negative, and in agreement with previous FCS studies (ΔH = -2.7 kcal/mol at pH = 6.5) [50].

It was suggested in ref. [74] that the relaxation process observed by FCS might involve protons coming from the inside of the protein. As a result, at higher pH, the observed blinking of EGFP may not be reduced to simple reversible protonation reaction from the bulk solution.

The temperature calibration curves of EGFP on Fig. 2.5b also show an interesting result. Different methods were used to control sample temperature when obtaining calibration curves using the two objectives. For the measurements with water objective, both stage and objective heater were used. However, only the stage heater was used for measurements using the air objective. Although both calibration curves are in agreement, the two calibration curves are crossing each other at the point which should indicate the room temperature (~24°C). For the calibration curve obtained by water objective, the difference of blinking relaxation time measured at the extreme temperatures is smaller than the result obtained by the air objective. This indicates that the objective heater did not sufficiently adjust the temperature of the water objective, and this could be due to heat dissipation on the objective at the region which is not covered by the objective heater.

Temperature measurements using the detection of fluorescent protein blinking by FCS present multiple advantages. First of all, the method can provide an absolute temperature measurement. Also, the temperature measurement is not sensitive to the excitation laser power ($\leq$ 200 μW) and size or shape of the detection volume. In addition, I have shown that using an air immersion objective can provide noninvasive measurement of the protein blinking. Furthermore, it has already been shown that the measurement on blinking relaxation time is not sensitive to the fluorophore concentration [51]. So, the temperature measurement using this approach does not require any EGFP concentration calibration. However, there is an optimal working concentration range of fluorophore for FCS, which is < 200 μM. The higher fluorophore concentration can induce error to the

autocorrelation analysis, because the fluctuation of fluorescence intensity due to the diffusion of fluorophores across the detection volume is insignificant compared to the average intensity. Therefore, small fluorophore concentration is preferred in FCS measurement. Nevertheless, the insensitivity of blinking measurement to the fluorophore concentration and the alignement of FCS make the proposed method an improvement over methods using fluorescence intensity as a gauge to temperature. The result in the application part shows that our method can be used to characterize steep temperature gradients with good spatial resolution. It also shows that the method can be applied at a liquid/solid interface as long as the solid surface does not modify the reversible protonation of the proteins. Finally, this method has the potential to be applied directly in biological samples by using genetically encoded fluorescent protein fusions. By using FCS, not only are we able to measure the concentration and the mobility of the fusion proteins in the cell, we can also determine additional information on the thermal environment of the protein in just a single measurement. One major concern for using EGFP to measure temperature in cells is that the blinking relaxation time has weak temperature dependence at physiological pH. Consequently, if we want to apply this method to measure temperature in sample at physiological pH, a fluorophore with higher pK_a ($pK_a \geq 7$) will be required in order to provide more accurate temperature measurements. On the other hand, using EGFP for temperature measurement *in vitro* can be onerous. In the next chapter, I present my investigations of the blinking of another fluorophore, a small organic molecule, pyranine ($pK_a \sim 7.3$).

Chapter 3

Simultaneous pH and Temperature Measurements Using Pyranine as a Molecular Probe

3.1 Introduction

In picoliter fluid compartments such as those found in microfluidic devices and in living cells, physical variables such as molecular concentrations, pH, and temperature can vary significantly over distances as short as a few micrometers. In microfluidic devices, sharp gradients can be created and controlled by combining several fluid flows into a single narrow channel [46, 75], but they may also unexpectedly arise from differences in conditions, for example temperature, between the fluid and the chamber [28, 29]. In cells, many cellular events can lead to local changes in either molecular concentration (including pH) or temperature. Intracellular signaling and the establishment of cell polarity, for example, are both based on the creation of sharp molecular gradients across the cell [76, 77]. Proton gradients build up across the inner and outer mitochondrial membrane as a result of ATP synthesis [1], and across the membrane of liposomes during endocytosis [8, 35, 36]. Spatially resolved methods allowing quantitative concentration or temperature measurements are therefore important tools for the study of the underlying processes leading to gradient formations in these systems. ATP hydrolysis can result in localized heat production at the mitochondria or the endoplasmic reticulum [4, 78].

Among all possible methods for pH and temperature measurements, optical methods allow submicron spatial resolutions and have the advantage of being non-invasive. Among these, fluorescence methods present the additional advantage of permitting high sensitivity measurements. The simplest fluorescence methods rely on the measurement of the pH or temperature dependent fluorescence emission intensity of a fluorescent probe. For example, the fluorescence quantum yield of BCECF is highly sensitive to pH, and therefore the fluorescence intensity of a solution containing a small concentration of this dye can be used as an indication of pH [19]. Similarly, the fluorescence quantum yield of rhodamine B changes with temperature, allowing temperature measurements [27]. These methods, however, are not appropriate for characterizing spatial gradients if either the excitation intensity, the collection efficiency or the fluorescent probe concentration is not uniform across the field of view. A more refined approach is therefore to use ratiometric methods, where two different fluorescence quantities are measured and compared through the calculation of their ratio, which eliminates any dependence on instrument characteristics or probe concentration [79]. This method has been widely applied for *in vivo* pH measurements, using the ratio of the emission intensities collected at two different wavelengths [35, 36, 80, 81]. Another possible approach is to measure a quantity that is not dependent on concentration, such as the probe diffusion coefficient [82], its fluorescence lifetime [43, 46], or the relaxation time of the fluorescence blinking generated from association and dissociation of protons to the fluorescent probe [51, 52].

In that context, we recently proposed to use the relaxation time associated with EGFP blinking for temperature measurements [63]. In presence of protons, EGFP constantly switches between a deprotonated form which is fluorescent under 488 nm excitation, and a protonated form which is not, causing a blinking

which can be quantified using fluorescence correlation spectroscopy (FCS) [50]. We showed that the relaxation time associated with this blinking is strongly temperature dependent and that it can therefore be used as a gauge to measure temperature [63]. However, the equally strong dependence of this parameter on other variables, in particular pH and buffer composition, requires attention. In addition, detection of protonation-dependent blinking by FCS is most sensitive at or below the probe pK_a, that is below pH ~ 6 for EGFP [63]. Finally, although GFP derivatives are expected to be useful in a cellular context since they can be genetically encoded, the use of organic fluorophores allows more flexibility in general.

Here we report on our investigations of the well-known pH sensitive dye 8-Hydroxypyrene-1,3,6-trisulfonic acid trisodium salt (pyranine or HPTS) as a possible combined pH and temperature indicator. Pyranine is a small, negatively charged organic fluorophore which is soluble in water and membrane impermeable [64]. Pyranine possesses a hydroxyl group and, like EGFP, it can exist in a protonated and a deprotonated form. Both are fluorescent, but with very different excitation maxima: 405 nm for protonated pyranine, and 450 nm for deprotonated pyranine [34, 64]. Pyranine is therefore an excellent probe for ratiometric pH measurements. It has been used in particular to measure pH inside and on the outer surface of liposomes [34], in endocytic vesicles [35] and in endocytic organelles in neurons [36]. In addition, pyranine has been often used as a photoacid to study proton transfer in acid-base reaction [66-69, 71, 83, 84]. Since pyranine has a pK_a ~ 7.2, we postulated that it would exhibit a detectable fluorescence blinking around physiological pH and below. We used FCS to study the photophysics of pyranine under 442 nm excitation, and we did detect a blinking corresponding to a protonation reaction, with an equilibrium constant and a relaxation time depending as expected both on pH and temperature. We further investigated the influence of buffer and salt concentration on the protonation

reaction, in order to establish the robustness of pH and temperature measurements inferred from pyranine blinking characteristics.

3.2 Materials and Methods

3.2.1 Sample preparation

Stock solutions of 4 g/l (7.6 mM) pyranine (purchased from Sigma-Aldrich) were prepared in phosphate buffered saline (PBS, 10x concentration, Bioshop, Burlington, Canada). For FCS measurements, pyranine stock solutions were diluted in a buffer solution down to concentration that ranged from 40 nM to 750 nM, depending on the pH of the solvent. Different types of buffer were used: Standard PBS (10 mM Na_2HPO_4, 2 mM KH_2PO_4, 137 mM NaCl, 2.7 mM KCl), modified PBS (where the concentration of one component was modified compared to standard PBS), basic phosphate buffer (10 mM Na_2HPO_4, 2 mM KH_2PO_4, and various concentration of NaCl, KCl, or $MgCl_2$), and HEPES buffers (20 mM HEPES, and various concentrations of NaCl, KCl, $MgCl_2$, or $CaCl_2$). Due to the formation of calcium phosphate precipitates, $CaCl_2$ ions were not used in phosphate buffers. All buffers were prepared with double distilled water. The buffers pH was adjusted by addition of HCl or NaOH, and measured using a digital pH meter. The ionic strength of the buffers was calculated according to:

$$\mu = \frac{1}{2}\sum_i c_i z_i^{\,2}$$

where c_i and z_i are the concentration and charge of ion i, respectively. It was considered that HEPES, a zwitterion, did not contribute to the ionic strength as suggested by Stellwagen *et al.* [85].

3.2.2 Fluorescence correlation spectroscopy

FCS experiments were performed on a home-built FCS instrument. The 442nm line of a He-Cd laser (Liconix, Santa Clara, CA) was first directed through a variable neutral density filter (Thorlabs, Newton, NJ) for adjustment of the laser

beam power, which was then measured using an optical power meter (Newport, Irvine, CA). It then passed through an adjustable iris allowing changing the beam diameter, in order to vary the size of the confocal detection volume. The beam then entered the back port of an inverted microscope (Nikon Eclipse TE2000-U, Nikon, Tokyo, Japan), where it passed through a band pass excitation filter (D436/10x, Chroma, Rockingham, VT) before being reflected upward by a dichroic mirror (455DCLP, Chroma, Rockingham, VT), into the back aperture of an air immersion objective (Plan Apo 60x 0.95NA, Nikon, Tokyo, Japan). Emitted fluorescence was collected by the same objective, passed through the dichroic mirror and through an emission filter (E475LPv2, Chroma, Rockingham, VT), and was focused through a pinhole in order to remove out-of-focus fluorescence. Five different sizes of pinhole were used, 50-, 75-, 100-, 150-, and 200-μm (purchased from Thorlabs), depending on the diameter of the excitation laser beam. Finally, the emitted fluorescence was separated by a 50/50 beam splitter (Chroma, Rockingham, VT) into two separate channels, and detected by two photomultiplier tubes (H7421, Hamamatsu Photonics, Hamamatsu City, Japan). The collected signals were fed to a multiple-tau correlator (Flex02-08D, Correlator.com, Bridgewater, NJ) that performed correlation analysis. Pinhole alignment and data acquisition were handled by a program written for Labview (National Instruments, Austin, TX). Most samples were placed in a chamber made by a microscope slide and a cover slip spaced by parafilm and sealed with wax. The temperature of such samples was controlled using an inverted microscope stage temperature control system (PE-100NI, Linkam Scientific, Surrey, UK). For microfluidic measurements, chips made of PDMS (microfluidic ChipShop, Jena, Germany) were used. The cross section of the microfluidic channel was a trapezoid, with a height of 20 μm, and a width varying between 92 μm and 120 μm. The inlet of the microfluidic chip was connected to a 20 ml syringe through a silicone tube. The syringe was then loaded on a digital infusion syringe pump (SP100i, World Precision Instruments, Inc.), dispensing flow rates between 0.03

and 1 ml/hour. For all samples, at least 5 individual FCS measurements were performed, each lasting between 30 and 200 s.

3.2.3 Analysis of the autocorrelation functions

In the absence of flow, autocorrelation functions were analyzed assuming pyranine was freely diffusing and undergoing a blinking process with exponentially distributed dwell times [50]:

$$G(\tau) = \frac{1}{N}\left(1+\frac{\tau}{\tau_D}\right)^{-1}\left(1+\frac{\tau}{S^2\tau_D}\right)^{-1/2}\left[1+\frac{B}{1-B}\exp\left(-\tau/\tau_B\right)\right] \qquad (3.1)$$

S is the aspect ratio of the ellipsoidal confocal volume. N is the average number of pyranine molecules present in the confocal volume, and τ_D is indicative of their residence time in that volume. τ_B is the relaxation time associated with pyranine blinking, and B is the fraction of pyranine molecules found on average in the dark state.

At the beginning of each series of measurement, fluorescein was used to determine the half-width, w_0, and half-height, z_0, of the confocal detection volume. Fluorescein has a known diffusion coefficient, D = 260μm^2/s [86], which allows calculating w_0 using the expression: $\tau_D = w_0^2/4D$, while z_0 can be calculated using the aspect ratio: $S = z_0/w_0$. The effective confocal volume is given by: $V = \pi^{3/2} w_0^2 z_0$, and allows calculating fluorophore concentrations: $c = N/V$.

In the presence of flow the expression of the autocorrelation function requires an additional term [87]:

$$G(\tau)_{flow} = G(\tau)\cdot\exp\left[-\left(\frac{\tau}{\tau_{flow}}\right)^2\left(1+\frac{\tau}{\tau_D}\right)^{-1}\right] \qquad (3.2)$$

where τ_{flow} is related to the flow rate, $v = w_0/\tau_{flow}$.

In all cases, we used the software KaleidaGraph (Synergy Software, Reading, PA) to analyze the obtained autocorrelation functions. Each reported parameter value represents an average value for at least 5 individual measurements, and the associated error corresponds to either the average error returned by the fitting program or the standard deviation of the 5 individual parameter values, whichever was the largest.

3.2.4 Determination of the thermodynamics parameters associated with protonation and deprotonation

Assuming that the fraction of non-fluorescent pyranine molecules, B, corresponds to the fraction of protonated pyranine molecules, we have:

$$B = \frac{[AH]}{[AH]+[A^-]}$$

where [AH] is the concentration of protonated pyranine and [A^-] is the concentration of deprotonated pyranine. We can therefore simply calculate the equilibrium constant associated with the protonation reaction from B using the Henderson-Hasselbalch equation:

$$K = \frac{[HA]}{[H^+][A^-]} = \frac{1}{10^{-pH}} \cdot \frac{B}{1-B} \qquad (3.3)$$

So that B is expected to vary with pH according to:

$$B = \left(10^{pH-pK_a}+1\right)^{-1} \qquad (3.4)$$

The rate constant for protonation, k_p, and the rate constant for protonation, k_d, can be calculated from the experimentally accessible parameters B and τ_B, since $K = k_p / k_d$ and since:

$$\tau_B = \frac{1}{[H^+]\cdot k_p + k_d}$$

Therefore:

$$k_p = \frac{B}{\tau_B \cdot 10^{-pH}} \tag{3.5}$$

and

$$k_d = \frac{1-B}{\tau_B} \tag{3.6}$$

3.2.5 Temperature dependence of the thermodynamic parameters.

For a blinking process due to a reversible chemical reaction with rate constants obeying Arrhenius' law, the associated relaxation time, τ_B, should depend on temperature according to:

$$\tau_B = \left[10^{-pH} \cdot A_p \exp\left(-\frac{E_p}{RT}\right) + A_d \exp\left(-\frac{E_d}{RT}\right) \right]^{-1} \tag{3.7}$$

R is the gas constant. E_p and E_d are the activation energies for protonation and deprotonation respectively. A_p and A_d are the frequency factors for protonation and deprotonation, respectively. Similarly, the equilibrium constant is expected to obey:

$$\ln(K) = -\frac{\Delta E}{R} \cdot \frac{1}{T} + \ln\left(\frac{A_p}{A_d}\right) \tag{3.8}$$

where $\Delta E = E_p - E_d$ is the difference in activation energies.

To determine the relationship between the pK_a and the temperature, we use the relationship between the free energy change associated with the reaction, ΔG, and the equilibrium constant:

$$\Delta G = -RT \ln K_a$$

and combine it with the Gibbs free energy equation:

$$\Delta G = \Delta H - T\Delta S$$

Assuming the enthalpy change, ΔG, and entropy change, ΔG, associated with protonation do not significantly depend on temperature, the temperature dependence of the pK_a should be:

$$pK_a = -\frac{1}{2.303R} \cdot \left(\frac{\Delta H}{T} - \Delta S \right) \tag{3.9}$$

3.3 Results

3.3.1 Observation of pyranine protonation using fluorescence correlation spectroscopy

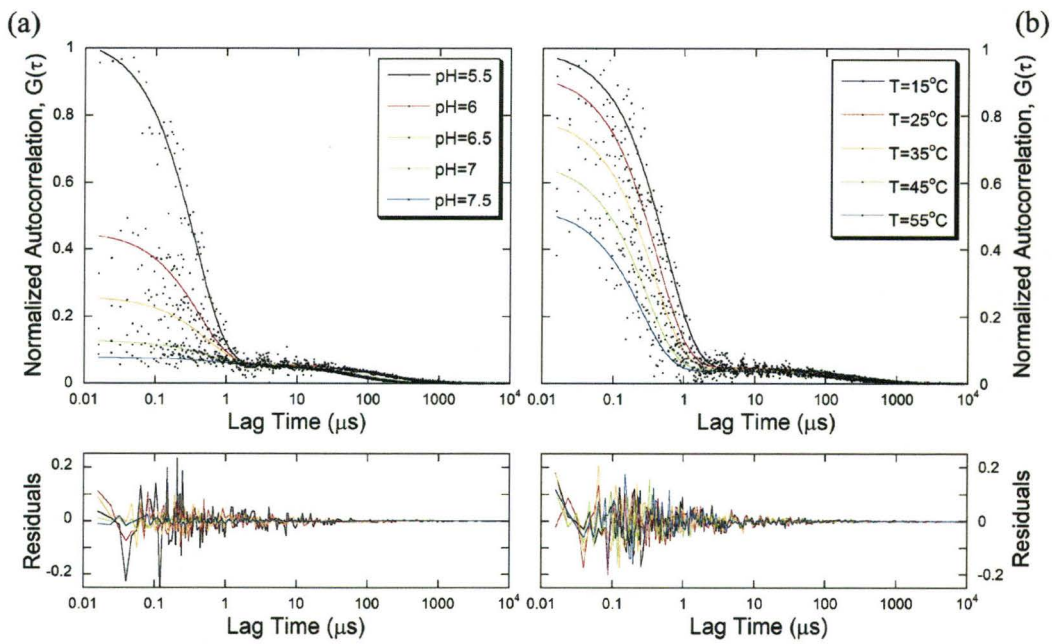

Figure 3.1. Pyranine blinking due to protonation/deprotonation as observed by FCS. (a) Autocorrelation functions obtained from pyranine in PBS at various pH (T=30°C) and residuals corresponding to the fits. (b) Autocorrelation functions of pyranine in PBS (pH=5.5) for different temperature and residuals corresponding to the fits. Data was fitted with Eq. (3.1) and normalized using the same amplitude of the diffusion term.

We used FCS to study solutions of pyranine in phosphate buffer (standard PBS) for pHs ranging between 4 and 9 and for temperatures ranging from 15°C to 55°C. We used a 442 nm excitation wavelength, at which only the non-protonated form of pyranine is fluorescent, so that reversible protonation of the fluorophore should result in detectable fluorescence fluctuations. As expected, the

autocorrelation functions (ACFs) obtained showed two distinct decays, one around ~100 μs characteristic of fluorophore diffusion, and one around ~ 1 μs which we attributed to reversible fluorophore protonation (Fig. 3.1a & 3.1b). We consequently analyzed all ACFs using Eq. (3.1), and Fig. 3.1a & 3.1b also show the residuals corresponding to the fits. After we obtained the parameters τ_D and τ_B from the analysis of the ACFs, the residence time and the relaxation time associated with blinking of pyranine as a function of pH is shown in Fig. 3.2a for pyranine at 20 and 50°C. Also, the fraction of pyranine in the non-fluorescent state, B, obtained from the analysis is shown in Fig. 3.2b. In agreement with the hypothesis that this non-fluorescent state corresponds to the protonated state of the fluorophore, B switches from a value of ~1 at low pH to a value of ~0 at high pH according to the Henderson-Hasselbalch equation (Eq. 3.4, with a small background term added). This analysis returns a value of the pK_a which slightly decreases with temperature, from ~7.1 at 15°C to ~6.9 at 55°C. This range of values is in good agreement with previously reported values for the pK_a of pyranine [33, 34, 64]. Assuming that the enthalpy change (ΔH) and entropy change (ΔS) associated with pyranine protonation are constant in the temperature range explored, the linear dependence of the pK_a on inverse temperature (Fig. 3.2c, inset) can be understood in terms of Gibbs equation for the free energy of a reaction (Eq. 3.9). Doing so provides $\Delta H \sim -10 \pm 1$ kJ/mol and $\Delta S \sim 0.101 \pm 0.003$ kJ/(K.mol).

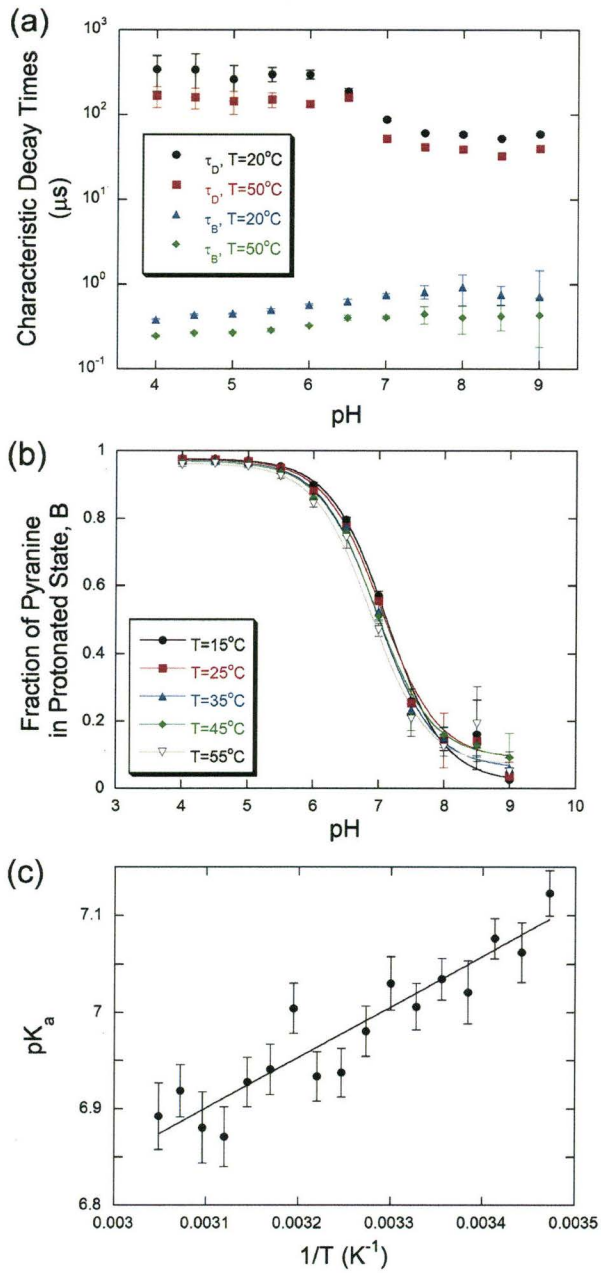

Figure 3.2. (a) Average residence time of pyranine as a function of pH in the detection volume. (b) Fraction of pyranine in protonated state as a function of pH at various temperatures. Data were fitted with Eq. (3.4). (c) Dissociation constant of pyranine as a function of the inverse absolute temperature. Data were fitted with Eq. (3.9).

3.3.2 Temperature and pH dependence on the reversible protonation process of pyranine

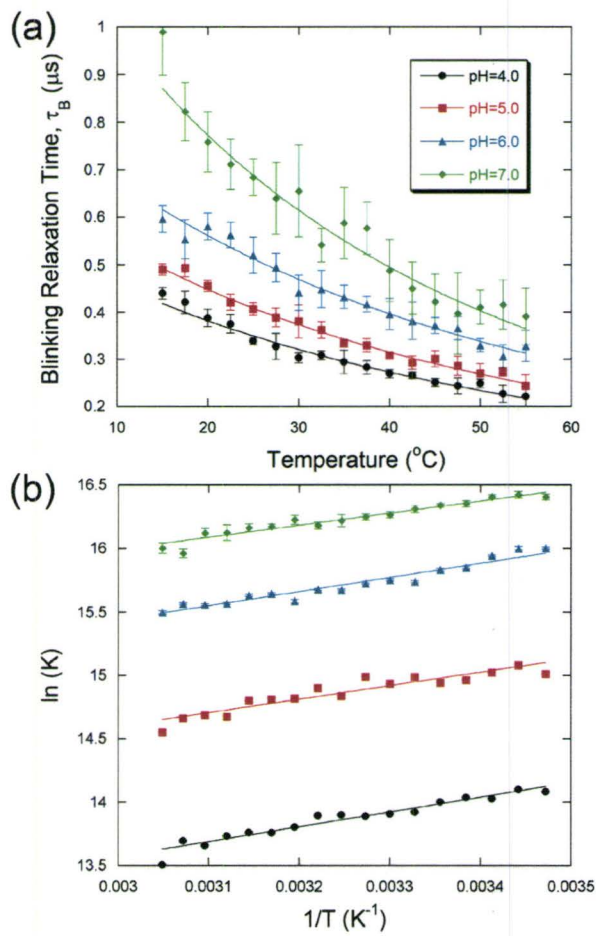

Figure 3.3. (a) Equilibrium constant of the protonation / deprotonation reaction determined from pyranine's blinking as a function of the inverse absolute temperature at various pH. Data was fitted with Eq. (3.7). (b) The blinking relaxation time of pyranine against temperatures at different pH. Data was fitted with Eq. (3.8). All errors are the standard deviations calculated from multiple measurements.

When considering the ACFs recorded at a given pH for different temperatures (Fig. 3.1b), we observed that both the amplitude of the photophysics

term (directly related to the fraction of protonated pyranine) and its characteristic decay time (equal to the relaxation time associated with pyranine protonation) decreased with increasing temperature. Analysis of these ACFs allowed obtaining the relaxation time associated with pyranine protonation and deprotonation as a function of temperature (Fig 3.3a), as well as the natural log of the equilibrium constant of the reaction (shown in Fig. 3.3b as a function of the inverse of the temperature). The relaxation time showed a stronger temperature dependence for pHs approaching the pK_a of pyranine, however the error on the measured values of the relaxation time also became larger with increasing pH. Assuming that the rate constant for protonation and deprotonation are following Arrhenius' law, the temperature dependence of the equilibrium constant and relaxation time associated with the protonation reaction should be accurately captured by Eqs. 3.7 and 3.8. We found that this was the case, and fitting of the data with these equations provided the values of the frequency factors (Fig. 3.4a) and of the activation energies (Fig. 3.4b) of the protonation/deprotonation process at each of the different pHs studied.

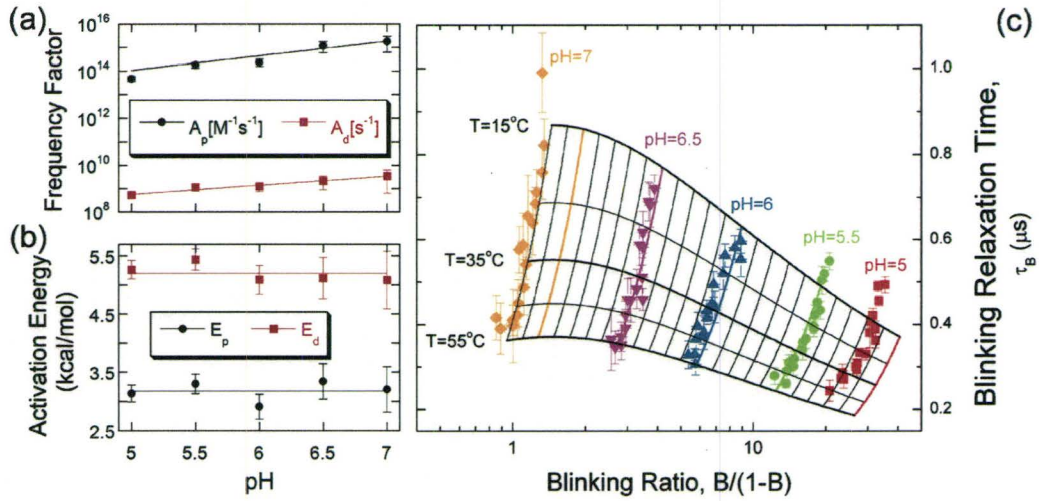

Figure 3.4. (a) Frequency factors of the Arrhenius equation and (b) activation energies of the protonation / deprotonation of pyranine at various pH. (c) Blinking relaxation time against blinking ratio for protonation / deprotonation process of pyranine. The solid lines represent the expected dependence at either fixed pH or fixed temperature. Same colour is used for the data at a given pH and the corresponding expected dependence at that pH. The fit of the frequency factors and the activation energies at different pH in (a) and (b) were used to calculate the expected dependence shown in (c). Fitting equation of A_p:

$y = 8.8\times10^{10}\cdot\exp(1.4\cdot x)$; A_d: $y = 6.3\times10^{6}\cdot\exp(0.9\cdot x)$; E_p: $y = 3.2$; E_d: $y = 5.2$.

3.3.3 *Possibility of combined pH and temperature measurements using pyranine*

The fraction of protonated pyranine, B, depends strongly on pH and weakly on temperature, while the protonation relaxation time, τ_B, depends strongly on temperature and weakly on pH (Fig. 3.4c). This makes measuring temperature and pH using these parameters independently difficult. On the other hand, each combination of the two parameters B and τ_B corresponds to a unique combination of pH and temperature. Therefore, by measuring both B and τ_B (as done with FCS), we should be able to determine accurately both pH and

temperature. For this, one needs to relate B and τ_B to pH and temperature. In order to so, we first found two empirical expressions to calculate the frequency factors and the activation energies for protonation and deprotonation as a function of pH (Figs. 3.4a and 3.4b, empirical expressions are shown in the caption of Fig. 3.4). It was then possible to determine the iso-temperature and iso-pH lines using these expressions. Such lines are plotted in Fig. 3.4c, showing that around pH ~ 6 and T ~ 30 °C, both these parameters can be determined from B and τ_B with a precision of ~ 0.1 pH unit and ~ 2 °C.

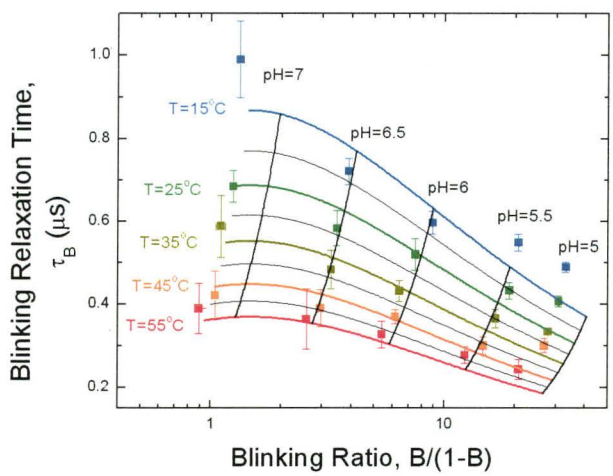

Figure 3.5. Blinking relaxation time against blinking ratio for protonation / deprotonation process of pyranine for few selected temperatures that illustrated on Fig. 3.4c. The solid lines represent the expected iso-pH or iso-temperature lines. Same colour is used for the data and the corresponding iso-temperature line.

3.3.4 Sensitivity of the measurement to excitation intensity, size of the detection volume, pyranine concentration and liquid flow.

For the pH and temperature measurement proposed to be valid, the measurement of the blinking parameters of pyranine by FCS must not depend on experimental characteristics (such as excitation intensity and exact size of the confocal detection volume) or pyranine concentration. We therefore investigated

how the excitation power, the concentration of pyranine, and the size of the confocal detection volume influenced the values measured for B and τ_B by FCS (for pyranine in PBS). We used a range of values for these parameters that included that usually used for FCS experiments (i.e. excitation intensities from 30 to 500 μW, pyranine concentrations from from 50 to 500 nM, and radius of the confocal observation volume from 0.2 to 1 μm). The results of these experiments are shown in Fig. 3.6. They indicated that, as expected, neither the measured fraction of protonated pyranine molecules, B, nor the measured blinking relaxation time, τ_B, was affected by the excitation intensity, the size of the observation volume or the fluorophore concentration.

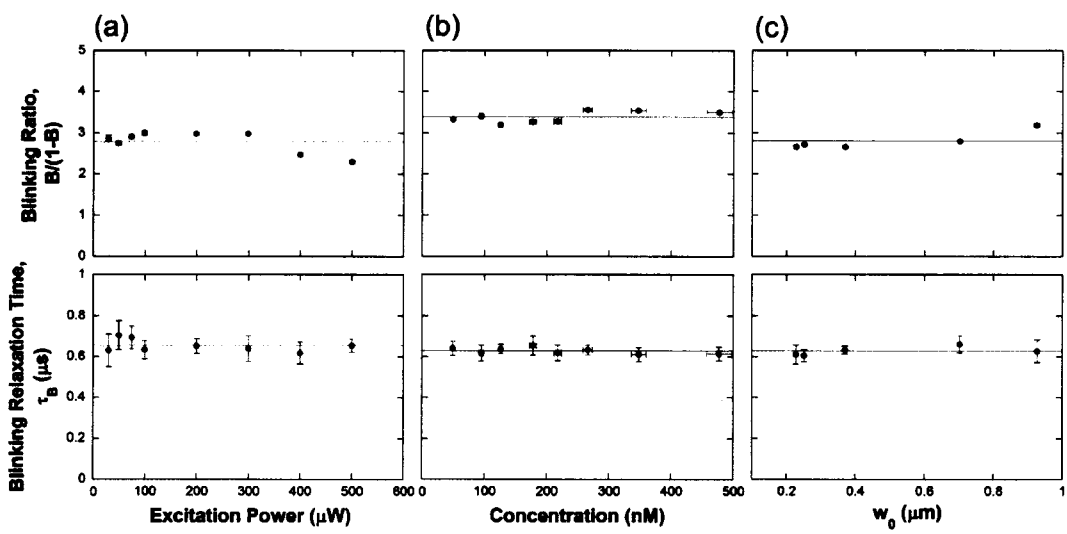

Figure 3.6. Stability of pH/temperature measurement against various factors. Blinking ratio (top) and blinking relaxation time (bottom) of pyranine against (a) the 442 nm excitation laser power, (b) the concentration of pyranine, and (c) the radius of the confocal detection volume. All pyranine samples are in PBS at pH=6.5. Measurements were taken at room temperature. Errors were calculated by the standard deviations.

For the pH and temperature measurement proposed to be applicable in systems such as microfluidic channels or living cells, the measurement should

also be insensitive to the eventual presence of liquid flow. We therefore performed FCS experiments for pyranine solutions flowing in a microfluidic chip. ACFs recorded for different velocities of the laminar flow are shown in Fig. 3.7a. While the decay time corresponding to the residence time of the pyranine molecules in the observation volume obviously decreases as the flow rate is increased, as expected, the decay term due to fluorophore blinking remains remarkably constant. Accordingly, the measured fraction of protonated pyranine and the measured protonation relaxation time were not dependent on flow rate (Figs. 3.7b). Therefore, liquid flow does not influence the FCS measurement of the blinking parameters of pyranine.

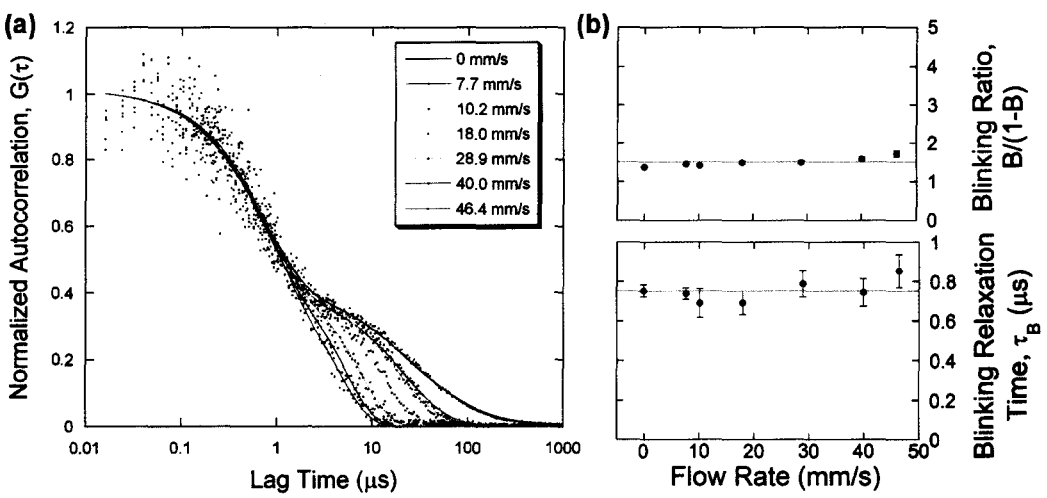

Figure 3.7. Stability of pH/temperature measurement against flow rate. (a) Normalized autocorrelation function of pyranine obtained in a microfluidic channel at different flow rate. The ACFs were fitted with Eq. (3.2). (b) Blinking ratio (top) and blinking relaxation time (bottom) of pyranine obtained in microfluidic channel at various flow rates. Pyranine is in PBS at pH=7 and the measurements were taken at room temperature. Errors were calculated by the standard deviations.

3.3.5 *Influence of buffer composition and ionic strength of the solution*

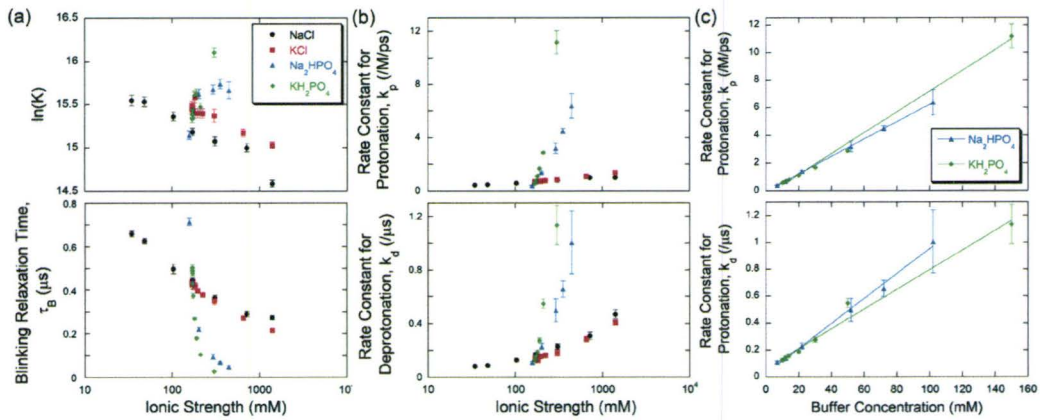

Figure 3.8. Protonation / deprotonation dependence on buffer composition. (a) Equilibrium constant (top) and relaxation time associated with the blinking (bottom) as a function of ionic strength when varying buffer conditions. The buffer in PBS (pH=5.5) with cone component concentration varied at a time. (b) Rate constant for protonation (top) and rate constant for deprotonation (bottom) as a function of ionic strength calculated from the data in (a). (c) Rate constant for protonation (top) and rate constant for deprotonation (bottom) as a function of buffer concentration and data were fitted with Eq. (3.10). Measurements were taken at 20°C.

One parameter which is known to influence protonation and deprotonation is the ionic environment of the molecule. The blinking of pyranine as detected by FCS will thus be dependent on buffer composition, and since this dependence cannot be avoided, it needs to be understood. Therefore, we next studied how different ions and their concentrations in the buffer influenced the protonation reaction. Starting from the PBS buffer used in all our previous experiments, we first investigated how varying the concentration of each individual buffer component affected the blinking of pyranine. The changes in the equilibrium constant and blinking relaxation time observed for these different components are shown in Fig. 3.8a, and the corresponding protonation and deprotonation rates are

shown in Fig. 3.8b. Two important observations can be made. First, the protonation equilibrium constant is only weakly dependent on buffer composition (with *ln K* changing only by ~3% for increases in the ionic strength on the order of 70-fold), while the reaction relaxation time noticeably decreased with increasing buffer ionic strength as a result of an increase in both protonation and deprotonation rates. Second, the influence of the phosphate buffer (Na_2HPO_4 and KH_2PO_4) on the reaction rates (and therefore on relaxation time) was much stronger than that of the salts (NaCl and KCl). In the following, we therefore consider in turns the effect of buffers and the effect of salts.

It has been previously proposed that the presence of another molecule with acid-basic properties (noted BH in its acidic form and B^- in its basic form in the following) could increase the probability of proton exchange for the molecule of interest (in our case pyranine, noted AH in its acidic form and A^- in its basic form) due to direct interaction according to: $AH + B^- \leftrightarrows A^- + BH$ [51]. In this scenario, the rate for protonation (or deprotonation) of pyranine is therefore the sum of the rate of the reaction with an isolated proton ($AH \leftrightarrows A^- + H^+$), k_P^0 (or k_D^0) and of the rate of the reaction with the other acid-basic molecule, $k_P^B[Buffer]$ (or $k_D^B[Buffer]$). The rate constant for protonation and deprotonation with the dependence of buffer concentration (Na_2HPO_4 and KH_2PO_4) from Fig. 3.8b is shown in Fig. 3.8c, and the results were fitted by the expression:

$$k_{P/D} = k_{P/D}{}^0 + k_{P/D}{}^B \cdot [Buffer] \qquad (3.10)$$

The dependence on buffer concentration we observed for the protonation and deprotonation rates of pyranine was indeed linear, therefore our data is consistent with the idea that phosphate molecules have a strong influence on the protonation of pyranine because direct proton exchange can occur between the two molecules. In addition, the parameters of the fit were tabulated on Table 3.1.

TABLE 3.1: Values of k_P^0, k_D^0, k_P^B, and k_D^B obtained from the analysis of the buffer concentration dependence of the equilibrium constant of the reversible protonation of pyranine.

	k_P^0 (/M/ps)	k_P^B ($/M^2$/ps)	k_D^0 (/μs)	k_D^B (/M/μs)
Na_2HPO_4	-0.04±0.02	62.7±0.4	0.03±0.02	9.3±0.3
KH_2PO_4	-0.3±0.1	75±2	0.06±0.02	7.3±0.4

To better understand the effect of salts on pyranine protonation, we studied pyranine blinking in either phosphate buffer (10 mM Na_2HPO_4 and 2 mM KH_2PO_4, same as for PBS) or HEPES buffer (20 mM HEPES), at pH = 5.5, and with varying concentrations of either monovalent (NaCl, KCl) or divalent ($MgCl_2$, $MgCl_2$) cations. The effect of these different salts on the equilibrium constant, relaxation time, protonation rate and deprotonation rate is shown in Fig. 3.9, where these parameters are plotted as a function of ionic strength. Strikingly, the values of K_a, τ_D, k_p and k_d measured for a given buffer are almost the same for all the ions studied, with the exception of $MgCl_2$ in phosphate buffer. This shows that, to first approximation, salts influence pyranine protonation only through the change in ionic strength they are causing.

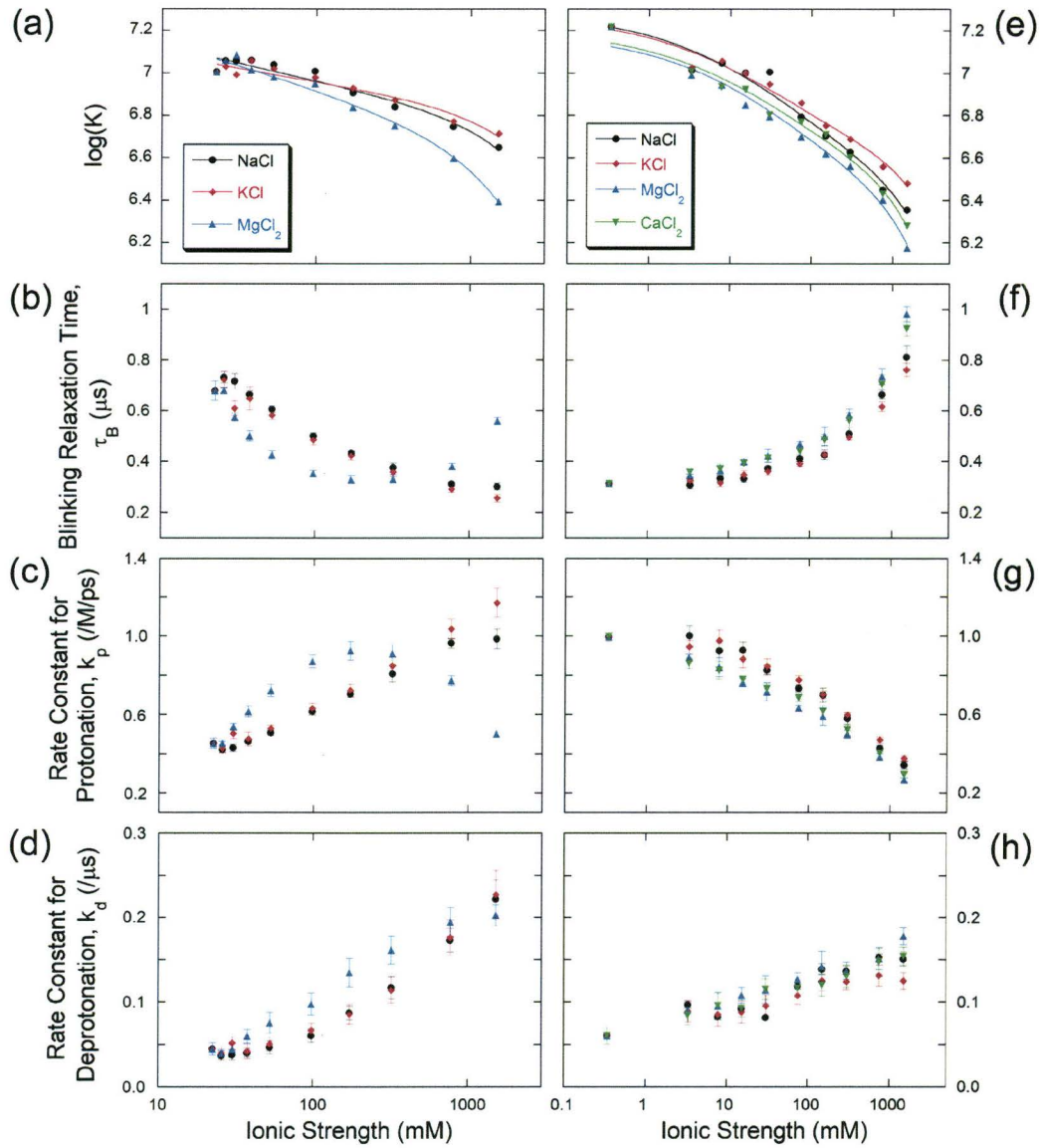

Figure 3.9. Protonation / deprotonation dependence on ionic strength. Equilibrium constant (a, e) and blinking relaxation time (b, f) of pyranine as a function of ionic strength. Rate constant for protonation (c, g) and for deprotonation (d, h) of pyranine calculated from the data in (a, b, e, f). Buffer in (a, b ,c, d) was 10 mM sodium phosphate and 2 mM potassium phosphate, and buffer in (e, f, g, h) was 20 mM HEPES. The legend indicates which salt was added in order to vary the ionic strength. All samples are at pH=5.5 and all the measurements were taken at 20°C. Lines are fit of the data with Eq. (3.11).

The influence of ionic strength on the equilibrium of acid-basic reactions has been studied by Boens *et al.* in the context the reversible protonation of BCECF [18]. They explained this influence in terms of the respective activities of the protonated and deprotonated form of the acid-basic molecule, which depend on ionic strength according to the Truesdell-Jones equation, an extended version of the Debye-Hückel equation. Taking into account these ionic-strength dependent activities allows rewriting the equilibrium constant for a reversible protonation reaction as [18]:

$$\log(K) = pK_a - \left[A\left(z_2^{\,2} - z_1^{\,2}\right)\frac{\sqrt{\mu}}{1 + \dot{a}B\sqrt{\mu}} + L\mu \right] - \log\left(a_{H_2O}\right) \qquad (3.11)$$

A and B are constants equal to A = 0.51 and B = 0.33 at room temperature and atmospheric pressure. z_1 and z_2 are the ionic charge of the protonated and deprotonated form of the acid-basic molecule. μ is the ionic strength of the solution. $\dot{a}$ is the ionic radius of the molecule in angstroms. L is an adjustable parameter, which depends on the experiment. a_{H_2O} is the water activity. In the case of pyranine (z_1 = -3 and z_2 = -4), Eq. 3.11 predicts that *log K* should decrease with increasing ionic strength, which is indeed what we observed for all the salts we studied. We fit our *log* K data with Eq. 3.11, fixing the water activity to 1, since it is ~1 in PBS [88]. The resulting values of pK_a, $\dot{a}$, and L obtained are listed in Table 3.2.

TABLE 3.2: Values of pK_a, $\dot{a}$, and L obtained from the analysis of the ionic-strength dependence of the equilibrium constant of the reversible protonation of pyranine.

Buffers	pK_a	$\dot{a}$ [Å]	L
Phosphate buffer + NaCl	7.35±0.04	19±4	0.14±0.05
Phosphate buffer + KCl	7.28±0.04	24±6	0.12±0.04
Phosphate buffer + $MgCl_2$	7.38±0.03	15±2	0.24±0.05
HEPES buffer + NaCl	7.28±0.03	12±2	0.14±0.07
HEPES buffer + KCl	7.26±0.02	15±2	0.10±0.04
HEPES buffer + $MgCl_2$	7.19±0.03	13±2	0.18±0.06
HEPES buffer + $CaCl_2$	7.20±0.02	14±2	0.18±0.05

Whereas the equilibrium constant showed a similar trend for all buffer and ions studied, the relaxation time associated with the protonation of pyranine had a very different dependence on ionic strength depending on the buffer. The relaxation time strongly decreases with ionic strength in phosphate buffer, but it strongly increases with ionic strength in HEPES buffer (Fig. 3.9). By looking at the rate constants, one can see that this difference stems from the dependence of the protonation rate on ionic strength. At pH = 5.5, the protonation rate dominates the relaxation time, $\tau_B \sim (k_p[H^+])^{-1}$. And whereas k_p increases with ionic strength in phosphate buffer, it decreases with ionic strength in HEPES buffer (Fig. 3.9). These opposite trends can be explained by taking into account the fact that, as discussed above, pyranine protonation (and deprotonation) is mostly due to direct interactions with buffer molecules, and that pyranine is a globally negatively charged molecule. At pH = 5.5, the dominant form of phosphate is the negatively charged $H_2PO_4^-$, with lesser amounts of HPO_4^{2-}, whereas the dominant form of HEPES is the zwitterion $C_8H_{17}N_2O_3S$–OH, with lesser amounts of $C_8H_{18}N_2O_3S$–OH^+ and $C_8H_{17}N_2O_3S$-O^-. Increasing the ionic strength should always result in an

increase in the reaction rate between two negatively charged molecules, such as pyranine and phosphate ions. Accordingly, the rates of phosphate buffer mediated protonation and deprotonation of pyranine increase with increasing solution ionic strength. Similarly, the rate of HEPES mediated deprotonation of pyranine increases with ionic strength, since the basic form of HEPES is also negatively charged. On the other hand, the acidic form of HEPES is a zwitterion, and as our results show, increasing the ionic strength decreases the protonation rate of pyranine, which could be because the rate of reaction between pyranine and HEPES decrease and/or the rate of reaction between pyranine and protons decrease.

In phosphate buffer, $MgCl_2$ produces a different effect from all the other ions. The protonation rate increases and then decreases with $MgCl_2$ concentration, and consequently the relaxation time decreases then increases with $MgCl_2$ concentration. This behavior could be the result of a small amount of magnesium phosphate precipitation forming in the buffer at high concentration of $MgCl_2$, changing the ion concentration in the buffer.

3.4 Discussion

Several observations support the idea that the fast ~1 μs decay of the autocorrelation functions obtained from pyranine solutions are due to fluorescence fluctuations caused by the reversible protonation of the molecule. First, we excited pyranine at a wavelength (442 nm) at which only the basic non-protonated form of the molecule is fluorescent, which means reversible protonation should result in fluorescence fluctuations. Second, the fluorescence fluctuations observed on the ~1 μs time-scale do not depend on focal volume size, showing that they are not due to center of mass motions of the fluorophore, nor do they depend on excitation intensity, showing that they are not due to other intensity-dependent photophysical properties of pyranine, such as triplet transition. Third, the observed fraction of non-fluorescent pyranine molecules decreases with increasing pH, according to the Henderson-Hasselbalch equation for the acid form of pyranine.

Our work suggests that pyranine can be used as a molecular thermometer, exactly as EGFP [63]. There are, however, a few important differences between the two molecules. First, pyranine is a smaller, cheaper fluorophore than EGFP, which can be more easily stored and manipulated than a protein, and which therefore is more advantageous for *in vitro* measurements. Second, whereas our previous study of EGFP photophysics showed that EGFP blinking could be detected reliably by FCS only for pH less than 6 (with very large measurement errors above that), the blinking of pyranine could be detected until pH=7 (with measurements errors, however, that did increase with pH). The reason behind this difference is that pyranine has a higher pK_a (7.2 at 20°C) than EGFP (5.8 at 20°C). And whereas the strong temperature dependence observed for the EGFP blinking relaxation time at low pH was lost when approaching physiological pH, the blinking relaxation time of pyranine retained a significant temperature

dependence over the whole pH range studied, that is until pH=7. For these reasons, pyranine, contrarily to EGFP, can be used as a molecular thermometer close to physiological pHs. Third, the relaxation time associated with pyranine protonation is much faster (~1 μs or less) than that associated with EGFP protonation (~100 μs or more) in similar pH, temperature and buffer conditions. This is probably due to the fact that the hydroxyl group of pyranine is readily accessible, whereas that of EGFP is buried inside the barrel structure of the protein. This is an advantage for FCS experiments, because it means the protonation term is better separated from the diffusion term in the FCS (by 3 orders of magnitude for pyranine, and only ~1 order of magnitude for EGFP), thus the parameters associated with the protonation can be measured with a greater accuracy for pyranine. On the other hand, however, the maximum dynamic range exhibited by the relaxation time of pyranine protonation (a ~3-fold decrease in the range 15 C to 55 C at pH = 7) is smaller than that exhibited by EGFP (~10-fold at pH = 5), which means temperature measurements using pyranine won't be as precise as when using EGFP.

A major limitation of the temperature measurements we proposed in the last chapter, based on the measurement of fluorophore protonation relaxation time, τ_B, is that they need to be performed at fixed and known pH. Similarly a major limitation of ratiometric pH measurements, based on the measurement of the ratio between protonated and deprotonated fluorophore, or B, is that they need to be performed at fixed and known temperature. Here, we have shown that using FCS to measure both τ_B and B, we can measure both temperature and pH in a single measurement. Our results show that the best working pH range is between 5 and 7 for pyranine, based on a comparison between measurements and theoretical predictions in Fig. 3.4c. We estimated that in this region, the combined pH and temperature measurement gives us an uncertainty not exceeding ±0.2 for pH measurements. The sample at pH between 5.5 and 6.5 gives us smaller error for

the measurement, within ±0.1. However, the measurement error starts to increase to ±0.2 when pH reaches either 5 or 7. The temperature measurement is less precise, to ±5°C.

As for EGFP, the detection of the blinking of pyranine is a very robust measurement, which does not depend on fluorophore concentration, excitation intensity, fluorescence collection and detection efficiency, size of the confocal volume or liquid flow. However, it is very sensitive to buffer concentration. This issue has already been raised by Widengren and colleagues, who studied the effect of buffer concentration on pH measurements based on the detection of fluorophore blinking by FCS [51]. They showed that the total rate of the protonation/deprotonation reaction, which is the inverse of the blinking relaxation time, increases linearly with buffer concentration for both GFP and FITC, due to direct proton exchange between the buffer molecules and the fluorophores. Our results suggests that direct proton exchange with phosphate ions indeed occurs, and that it is a major contributor to pyranine protonation, where for example the deprotonation rate increases about 2-fold upon addition of 20mM phosphate buffer at pH=5.5. Therefore the sensitivity of fluorophore blinking on buffer concentration seems inevitable, unless direct proton exchange with buffer molecules can be prevented. This means, however, that if temperature is precisely known, the value of the relaxation rate can be used to measure the concentration of a known buffer very accurately.

Pyranine blinking is also somewhat dependent on salt concentration. We found that the values of log(K) reliably decreased with increasing ionic strength of the solution. This can be understood qualitatively in terms of the relative stability of the different forms of the molecule. Deprotonated pyranine is a tetra-anion, whereas protonated pyranine is a tri-anion. Therefore increasing the solution ionic strength, and therefore the effects of charge screening, will increase

the stability of the deprotonated form of pyranine compared to its protonated form, thus decreasing K (Eq. 3.3). Since only the stability of the final products of the protonation/dperotonation reaction are important here, this result does not depend on the mechanism of protonation/deprotonation. Quantitatively, this effect is captured in the Truesdell-Jones equation, and its derivative, Eq. 3.11. Analysis of our data with these equations gave us good fits, and returned an average value for the ionic radius of pyranine (~16 Å) which is comparable to the value of the hydrodynamic radius of the molecule that can be calculated from our FCS data (~10 Å at pH < 7 and ~2 Å at pH ≥ 7), and to the ionic radius of BCECF determined by the modeling of the molecule (~ 8 Å) [18]. They are reasonable values given the ionic radii of other simple ions: the hydroxide ion has an ionic radius of 10.65 Å, while a heavier ion sulfate is around 5 Å [89]. For the other adjustable parameter in the fit, L, we also found values in a similar range than for other ions listed in ref [89].

The picture gets more complicated however when considering separately the dependence of the protonation and deprotonation rates on ionic strength. Whereas the deprotonation rate increases with increasing ionic strength both in phosphate and HEPES buffers, the protonation rate dependence on ionic strength is very different in both buffers. The protonation rate increases with ionic strength in phosphate buffers, but decreases with ionic strength in HEPES buffer. This can be explained qualitatively by remembering that protonation occurs in part through direct interactions between buffer and pyranine molecules, and by considering that phosphate and HEPES buffers have very different charges (phosphate ions are negatively charged, HEPES is a zwitterion). Therefore charge screening through increase of the solution ionic strength is indeed expected to increase direct interactions between the negatively charged pyranine and the negatively charged phosphate ions, and therefore buffer-mediated protonation. It may have an opposite effect in the case of HEPES, a zwitterion. In support of the theory that

protonation/deprotonation rates depends on ionic strength mainly because of interactions between the fluorophore and the buffer molecules, Widengren et al. found that NaCl alone in the solution would not change the rate of the proton exchange [51], we find that varying the chloride salts concentrations in buffer influences the reversible protonation rate. However, the influence of chloride salts on the pyranine blinking is smaller compared to the buffer.

Chapter 4

In Vivo pH Measurements in Pyranine Loaded Endosomal Vesicles Using Ratiometric Imaging

4.1 Introduction

Receptor-mediated endocytosis is triggered by the binding of agonists to membrane receptors. It leads to an uptake of extracellular materials. In addition, it induces receptor desensitization and internalization, which leads to a loss of responsiveness of the cell to the agonist as described in section 1.1.3. Cells have developed their own mechanism to restore this responsiveness by resensitizing and recycling the receptors back to the membrane. The resensitization of receptor involves dephosphorylation, and a previous *in vitro* study by Krueger et al has shown that the optimal condition to dephosphorylate the β2-adrenergic receptor, a member of the GPCR superfamily, is at pH = 5 [8]. By disrupting the acidity of the cells using NH_4Cl, they also showed that it impairs the receptor dephosphorylation in HEK 293 cells. Therefore, acidification of endosomal vesicles was proposed to be an essential step during the recycling process. In the present chapter, I describe my efforts to measure the temporal pH change in endosomal vesicles during the resensitization of μ-opioid receptors in HEK 293 cells. The μ-opioid receptor is a subtype of opioid receptor in the family of GPCR with opiate drugs as agonist. The μ-opioid receptors are commonly found in the

central nervous system, and they are the focus of studies to understand drug addiction [90].

To monitor temporal pH changes in cell, ratiometric imaging was used. However, instead of using single photon excitation as in most previous studies, the ratiometric pH imaging was done using two-photon excitation microscope. Two-photon excitation microscopy is based on laser scanning confocal microscopy [91]. A single photon with the proper wavelength can induce the fluorescence emission of a fluorophore. Alternatively, the same fluorophore can be excited by the absorption of two longer wavelength photons, where the combined energy of the two photons is able to bring the fluorophore to its excited state. However, the molecular absorption cross section for two-photon absorption is much smaller than that for single photon absorption. Therefore, two-photon excitation requires strong local instantaneous excitation intensity in order to sufficiently excite the fluorophores. The photon density at the focus of a femtosecond pulsed laser can achieve this strong localized intensity. Since only the intensity at the laser focus is strong enough to excite the fluorophores, two-photon excitation can reduce the overall photobleaching in the sample, and no confocal pinhole is required to remove out-of-focus fluorescence. Two-photon laser scanning microscope is a powerful tool to image live cells compared to single photon excitation. By using a near infra-red (NIR) laser, photodamage is further reduced in the sample. Also, using long wavelength excitation allows imaging thicker samples. The ratiometric imaging can also provide measurement in pH change within an area. On the contrary, pH and temperature measurement by FCS only allows for point measurement. Therefore, the ratiometric imaging should have an advantage to monitor the pH change of the intracellular vesicles that moved within the cells.

In section 1.2.2, I have already introduced the ratiometric approach as a method to monitor sample pH. The technique of ratiometric pH imaging is well-established with one-photon excitation. However, there are difficulties when applying this technique with two-photon excitation. These are due to the fact that many ratiometric dyes lose the changes in excitation or emission spectra at various pH with two-photon excitation, because usually the absorption or emission of one form dominates the other form (reviewed in ref. [92]). As a result, the ratiometric approach to monitor pH in two-photon excitation is still not a routine measurement method. Currently, studies have focused on finding suitable dyes in two-photon excitation [92-95].

In this chapter, I will first describe the implementation of ratiometric pH imaging with two-photon excitation using pyranine as a pH sensor. I measured the two-photon excitation spectra of pyranine to study the ratiometric properties of the dye; this led to the determination of two optimal excitation wavelengths for ratiometric pH imaging. Then, I investigated the influence of several experimental conditions on the measured value of the fluorescence ratio of pyranine. Further on, I applied two-photon ratiometric pH imaging to measure the acidity of endosomal vesicles in HEK 293 cells (human embryonic kidney cells) transfected with μ-opioid receptor DNA. HEK 293 cells have already been shown to have properties that resembles that of the stem cell of neurons [96], thus they represent a good neuronal cell model to study receptor-mediated endocytosis. The transfected HEK 293 cells stably expressed μ-opioid receptors, and endosomal vesicle formation was induced by the exposure of the cells to agonists. Our results, though encouraging, need to be validated by additional experiments and controls.

4.2 Materials and Methods

4.2.1 Preparation of media and reagents

The cell culture medium was composed of α-MEM (minimum essential medium) supplemented with 10% fetal bovine serum (FBS) and 1% Penicillin-Streptomycin (10,000 units/ml Penicillin, 10,000 μg/ml Streptomycin, Invitrogen, Carlsbad, CA, U.S.A.). To incubate the transfected cell line, the cell culture medium was supplemented with 0.5 g/l of Geneticin (G418, Invitrogen, Carlsbad, CA, U.S.A.). For imaging experiments, the cells were kept in an imaging medium. The imaging medium was composed of phenol red free α-MEM (Invitrogen, Carlsbad, CA, U.S.A.), 5% FBS, 1% Penicillin-Streptomycin, and 20 mM HEPES (1M solution, Invitrogen, Carlsbad, CA, U.S.A.).

[D-Ala^2, N-Me-Phe^4, Gly^5-ol]-Enkephalin acetate salt (DAMGO, Sigma-Aldrich, St. Louis, MO, U.S.A.) is a synthetic opiate drug with high specificity for μ-opioid receptors. The binding of DAMGO to μ-opioid receptors triggers endocytosis and then leads to receptor internalization. 10 mM stock solution of DAMGO in DDW were prepared, and stored at -20°C.

Pyranine (8-Hydroxypyrene-1,3,6-trisulfonic acid trisodium salt, Sigma-Aldrich, St. Louis, MO, U.S.A.) is an organic fluorophore with ratiometric characteristics that was described in chapter 1. 20 g/l (38 mM) stock solutions of pyranine were prepared in PBS (pH = 7.4), and the solutions were stored at room temperature in the dark. The stock solution was diluted at various concentrations in PBS at different pH to investigate fluorescence emission properties. To adjust sample pH, either HCl or NaOH was added to the sample, and the pH was monitored with a digital pH meter. For imaging the pyranine solutions, they were injected in sample chambers made of a microscope slide and a cover slip

separated with Parafilm stripes. The openings of the sample chambers were sealed with wax.

4.2.2 Tissue culture

The transfected HEK 293 cells (HEK293-MOR) is a cell line stably expressing μ-opioid receptors with hemagglutinin (HA) epitope tags, and it was generously provided by Dr. Stephen Ferguson at University of Western Ontario. In addition, wild type HEK 293 cells (wt-HEK293), which do not express the μ-opioid receptor, were obtained from the same group and served as a negative control. For cell culture, roughly 4 x 10^5 cells were seeded on a 60 mm disposable Petri dish with 5 ml of cell culture medium, and were incubated at 95% humidity and 5% CO_2 at 37°C. When the cell confluence reached 80 - 90%, cells were harvested, diluted and seeded on a new Petri dish. For imaging experiments, the cells were seeded on cover slip bottom Petri dishes. These were made by piercing a 1 cm x 1 cm hole in the center of a disposable Petri dish, and by gluing a cover slip at the bottom with silicone adhesive (Momentive performance materials, Albany, NY, U.S.A.). The special-made Petri dishes were then rinsed with 100% ethanol and placed under UV light for at least 15 minutes for sterilization. To enhance cell adhesion to the cover slip, the glass surface was coated with 1 mg/l fibronectin (1 g/l solution, Sigma-Aldrich, St. Louis, MO, U.S.A.) in PBS for at least 1 hour at room temperature. Afterward, the surface was rinsed with PBS before seeding the cells. When the cell confluence on the cover slip reached ~ 60%, the sample was ready for the next step in sample preparation.

4.2.3 Immunolabeling of μ-opioid receptors on HEK293-MOR cells

HA tagged μ-opioid receptors were immunolabeled using a Zenon labeling kit as follows. First, when needed to induce receptor-mediated endocytosis, 5 μl

of stock DAMGO was added to the cell sample together with 5 ml of fresh cell culture medium (DAMGO concentration = 10 μM). The sample was then incubated at 37°C with 5% CO_2 and 95% humidity for 30 minutes before washing twice with Hank's balanced salt solution (HBSS, Electron Microscopy Sciences, Fort Washington, PA, U.S.A.). For negative control of HEK293-MOR cells, the DAMGO treatment steps were skipped. Fixation of the cells was then performed by adding 4% paraformaldehyde in PBS and the sample was incubated at room temperature for 15 minutes before washing with HBSS. To permeabilize the cell membrane, the cells were treated with 0.2% Tween 20 (Sigma-Aldrich, St. Louis, MO, U.S.A.) at room temperature for 15 minutes, and the sample was washed three times with HBSS. Since the μ-opioid receptors contain HA tags, anti-HA primary antibodies were used and the primary antibodies were labeled fluorescently using a Zenon labeling kit according to the protocol suggested by the manufacturer (Zenon Rabbit IgG Labeling Kit with Alexa Fluor 546, Invitrogen, Carlsbad, CA, U.S.A.): 1 μl of primary antibody (Rabbit anti-HA, 1g/l, Bethyl Laboratories, Inc., Montgomery, TX) was added to 5 μl of the kit's Zenon labeling reagent, which contained the fluorescently labeled secondary antibodies. The mixture of the primary and the secondary antibodies was incubated at room temperature for 5 minutes. Then, 5 μl of blocking reagent in the kit was added to the mixture, and it was incubated at room temperature for another 5 minutes before adding 239 μl of HBSS. The diluted antibody solution was then applied to the sample, and incubated at room temperature for 30 minutes in dark. After washing the sample three times with HBSS, another fixation step was performed by incubating the sample with 4% of paraformaldehyde for 15 minutes. Then the sample was washed 3 times with HBSS, and the cells are kept in imaging medium during the experiments.

4.2.4 Preparation of pyranine loaded HEK 293 cells via endocytosis

First, the cells were kept in imaging medium instead of cell culture medium at 37°C for roughly one hour to minimize any potential shock to the cells due to a sudden change in medium. To trigger endocytosis, 5 – 50 µl of stock DAMGO (final concentration = 10 – 100 µM) was added to the sample supplemented with ~ 0.03 g/l (57 µM) of pyranine. Then the sample was incubated for various times (1 – 15 min) at room temperature or 37°C to study the efficiency of pyranine uptake by the cells. After the incubation, each sample was washed at least three times with HBSS to remove the pyranine left outside the cells. The sample was then kept in the imaging medium for fluorescence experiments.

4.2.5 Confocal imaging for pyranine solutions and cell samples

Confocal images of either the pyranine solutions or the cell samples were taken with a commercial laser scanning confocal microscope with one- or two-photon excitation (Leica DMI 6000B microscope with Leica TCS SP5 scanner). The microscope is connected to a PC and allows changing the settings of the microscope through a software, Leica Application Suite Advanced Fluorescence. This software also allows acquiring confocal images. To study fluorescence emission of pyranine in two-photon excitation, the tunable wavelength femtosecond pulsed NIR laser (Chameleon Ultra) was used to excite the pyranine samples. For all measurements, 10 mW laser power was used, which gave a good signal-to-noise ratio while keeping photobleaching to a minimum. To detect the fluorescence emitted by pyranine, the detection window was set in the range 490 – 530 nm, and the same detector gain (850 V) was selected for all measurements. For ratiometric pH imaging, two-photon confocal images at 810 and 860 nm excitation were taken in sequence automatically. The same laser power (10 mW)

and detector gain (850 V) were selected for both measurements. The choice of excitation wavelength (810 & 860 nm) will be discussed in section 4.3.1. To excite Alexa Fluor 546 and image the fluorescently labeled HEK 293 cells, a DPSS 561 nm continuous wave laser with 30 % of the laser power was used, and the detection window was set in the range 568 – 665 nm. Once again, the same detector gain (850 V) was used for all measurements.

4.2.6 Image analysis

The analysis of confocal images was performed using the image analysis software, ImageJ. All confocal images obtained from the SP5 laser scanning confocal microscope were 8-bit grayscale images, thus the pixel intensity ranged between 0 and 255. ImageJ was used to determine the average pixel intensity, F, and its standard deviation, σ, in selected areas of an image. Then, the standard error was calculated as, $\sigma/\sqrt{N}$, where N is the number of pixels in the selected area. Since the sampling size is large for each measurement (equals to the number of pixels), I determined the standard error as the uncertainty of the measurement to show the variation of data based on the population mean.

A Javascript program for ImageJ was written to produce a pH image from the two fluorescence confocal images acquired during ratiometric pH imaging (the first one corresponding to 810 nm excitation and the second to 860 nm excitation). This program determines at each pixel the ratio between the fluorescence emitted by pyranine at 810 & 860 nm excitation. Then, the measured fluorescence ratio is converted to pH using a previously obtained calibration curve. Finally, the result is displayed as a 2D pH image, colour-coded to represent the magnitude of pH at each pixel. The script of this program is shown in Appendix D. Briefly, the program does the following: For each pixel, the program reads the intensities of the 810 & 860 nm confocal images (F_{810} & F_{860}). If the emitted

fluorescence of the 810 nm image is lower than or equal to a fixed background intensity (determined as the average value of 810 nm confocal images of cell samples without pyranine), the program assigns a black colour to the pixel indicating that there was not enough fluorescence signal to calculate a pH value (background pixel). If the pixel intensity in either channel is at maximum value (F_{810} or F_{860} = 255), the program assigns a white colour to that pixel indicating that it is a saturated pixel. In all other cases, the program calculates the logarithm of the fluorescence ratio, $\log(F_{860}/F_{810})$. For each pH range as shown on Figure 4.1, there is a corresponding range of $\log(F_{860}/F_{810})$ values, which was determined from the fit of the pH calibration curve on Figure 4.3 (For example, $4 < pH \leq 4.5$: $-1.07 < \log(F_{860}/F_{810}) \leq -1.02$). Afterward, the program checks at each pixel, which pH range does the calculated value for $\log(F_{860}/F_{810})$ fall in, and it assigns different colours to the pixel according to the colour scheme shown in Figure 4.1. Finally, a 2D pH map is displayed, and the number of pixels falling in each different pH range is shown in a separate window.

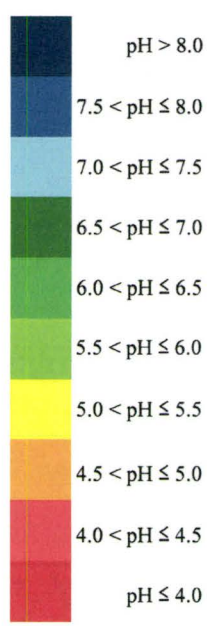

Figure 4.1. Colour scheme for pH maps produced by the ratiometric pH imaging method.

4.3 Results

4.3.1 Excitation spectra of pyranine in two-photon excitation

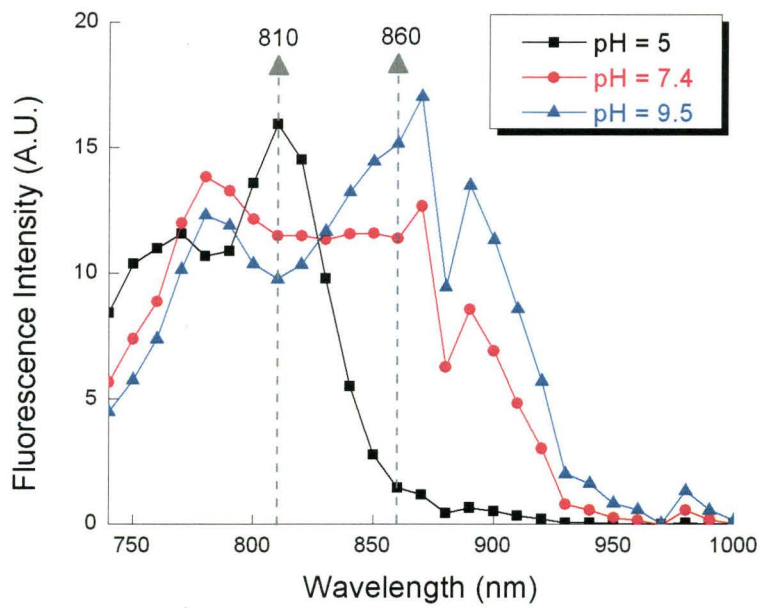

Figure 4.2. Excitation spectra of pyranine (0.04 g/l or 76 μM) at various pH measurements with two-photon excitation.

To determine the two-photon excitation spectrum of pyranine (there is no available method to determine two-photon absorption spectra), I measured the emitted fluorescence of pyranine at various excitation wavelengths, λ = 740 – 1000 nm, using the two-photon laser scanning microscope. The emitted fluorescence values were determined by analyzing confocal images of 0.04 g/l (76 μM) pyranine recorded for different excitation wavelengths. The background signal was determined by imaging PBS sample. Then, net average pixel intensities were calculated. Figure 4.2 illustrates the excitation spectra of pyranine as measured for three different pH (5, 7.4, & 9.5). These spectra can provide insights on fluorescence emission of pyranine at different pH, and the spectra can help selecting excitation wavelengths for ratiometric pH imaging. A first excitation of

810 nm was chosen because it is the maximum excitation wavelength of protonated pyranine in two-photon excitation (maximum excitation at low pH). The energy of two 810 nm photons is equivalent to that of a single 405 nm photon, which is consistent with the one-photon excitation maximum observed for protonated pyranine ($\lambda \sim 400$ nm) [33, 34, 64]. A second peak emerges on the excitation spectra at ~ 870 nm at higher pH. However, instead of choosing 870 nm, I selected 860 nm as the second excitation wavelength for the ratiometric measurements. This was to avoid the steep fluorescence drop observed between 870 & 880 nm, which is probably due to instrumental artifacts, and could introduce distortion in the measurements. Although 860 nm is not a maximum of the excitation spectra, the intensity at 860 nm excitation still changes significantly with varying pH. Consequently, the combination of 810 & 860 nm excitations provides a significant variation in fluorescence ratio with pH.

4.3.2 pH calibration curve of pyranine by two-photon excitation

Once the two excitation wavelengths for ratiometric pH imaging were chosen, fluorescence ratios (F_{860}/F_{810}) were measured by imaging pyranine samples (512×512 confocal images) at different pH. First, I determined the average intensities of 810 & 860 nm images (F_{810} & F_{860} respectively) and their standard errors. Then, fluorescence ratios (F_{860}/F_{810}), logarithm of the fluorescence ratio $\log(F_{860}/F_{810})$, and their propagated errors were calculated. Figure 4.3 shows $\log(F_{860}/F_{810})$ as a function of pH for pyranine in two-photon excitation. Each data point is an average of two measurements in the same sample, and the error bars were selected from the largest value of either the propagated error of each measurement or the standard deviation of the two measurements. The sigmoid curve shown on Figure 4.3 subsequently served as a pH calibration curve to measure pH in samples containing pyranine. The fit of the pH calibration

curve is a 4th order polynomial function producing the best fit for the data obtained for pH ranging between 4 and 8:

$$y = -17.8 + 12.8x - 3.63x^2 + 0.447x^3 - 0.0198x^4$$

This function is then used to calculate the expected values of $\log(F_{860}/F_{810})$ at different pH, and to convert the measured $\log(F_{860}/F_{810})$ to pH using the Javascript program described above.

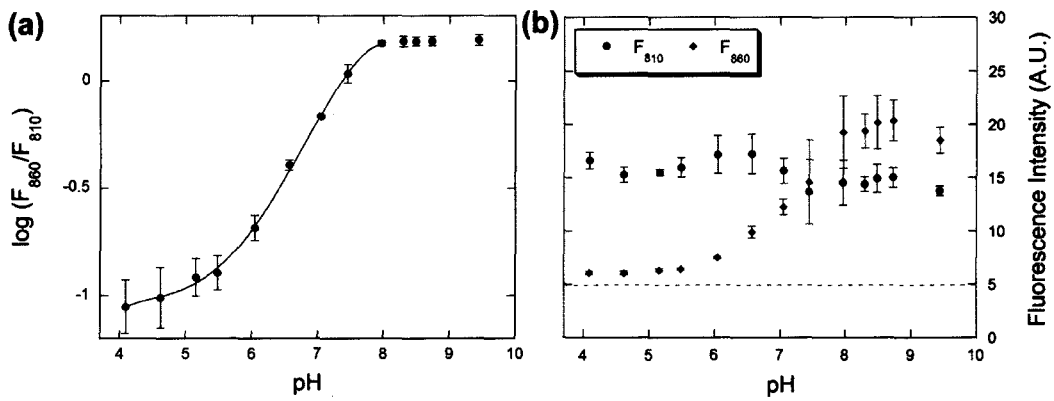

Figure 4.3. (a) pH calibration curve of pyranine (0.04 g/l or 76 μM) for ratiometric pH imaging with two-photon excitation. The best fit line is a 4th order polynomial function. (b) Fluorescence intensity measured for 810 nm & 860 nm excitations and used to build the pH calibration curve shown in (a). The dotted line is an estimation of fluorescence background of the sample.

4.3.3 Effects of various experimental conditions on the ratiometric pH imaging

The ability to reproduce identical results in spite of fluorophore concentration and instrumental variations is desirable for any pH measurement method. Ratiometric pH imaging with one-photon excitation has already been shown to be a robust method to measure pH *in vivo* [35, 36]. This section illustrates the effects of various experimental conditions on the measured fluorescence ratio with two-photon excitation. First, Figure 4.4a shows the measured value of $\log(F_{860}/F_{810})$ as a function of pyranine concentration in PBS

(pH = 5). The error bars are the propagated error calculated from the standard errors of F_{860} and F_{810}, and the error bars are very small in this case. Figure 4.4b and 4.4c show the corresponding fluorescence intensities measured at 810 & 860 nm excitation respectively. The result indicates that there is a gradual decrease in $\log(F_{860}/F_{810})$ at pyranine concentration < 57 μM (< 0.03 g/l), and no significant difference at concentration ≥57 μM. In this case, the signal-to-noise ratio is extremely low at concentration < 57 μM.

Next, I examined the effect of laser scanning speed on $\log(F_{860}/F_{810})$. The laser scanning speed or scan rate in image acquisition relates to the dwell time of the focused laser beam illumination at each pixel. The measured value of $\log(F_{860}/F_{810})$ against laser scanning speed (10 – 1000 Hz) is shown in Figure 4.5a, and the fluorescence intensities versus the scan rate are shown in Figure 4.5b and 4.5c. Again, the error bars are the propagated errors for the log values, and the error bars of the intensity values are the standard errors. The figure shows relatively constant $\log(F_{860}/F_{810})$ values except at low laser scanning speed < 100Hz. In parallel, Figure 4.5b and 4.5c show that the intensity begins to decrease at scan rate < 100 Hz at pH = 5, and < 200 Hz at pH = 9, probably due to photobleaching.

Figure 4.6 shows several pH calibration curves obtained at different focal planes above the cover slip surface in the sample chamber. Each data point is an average of three measurements, and the error bars are the standard deviation of the three measurements. The results indicate that all pH calibration curves are in good agreement, so there is no significant variation for $\log(F_{860}/F_{810})$ measured at various depths in the sample.

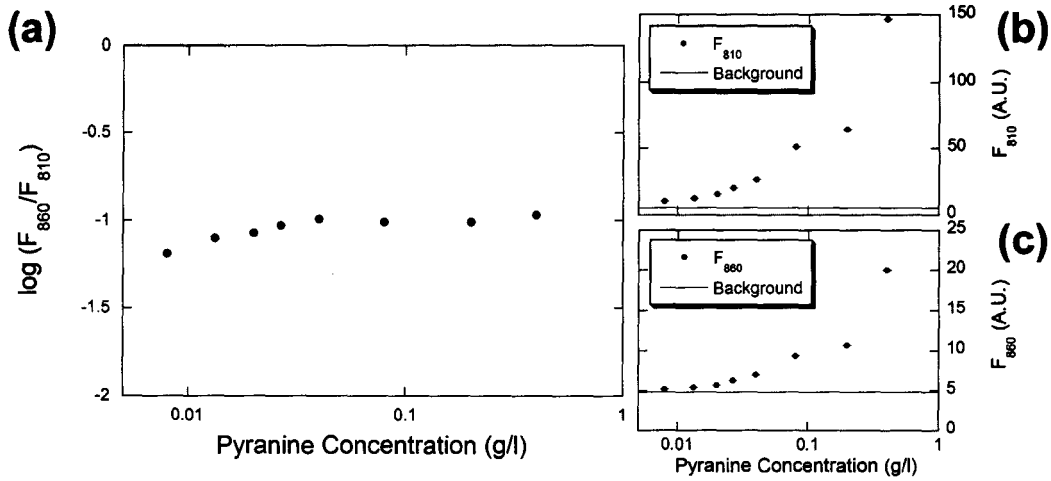

Figure 4.4. (a) Log(F_{860}/F_{810}) measured at various concentrations of pyranine with two-photon excitation. (b) Fluorescence intensity of pyranine measured at (b) 810 & (c) 860 nm excitations and compared to the background intensity.

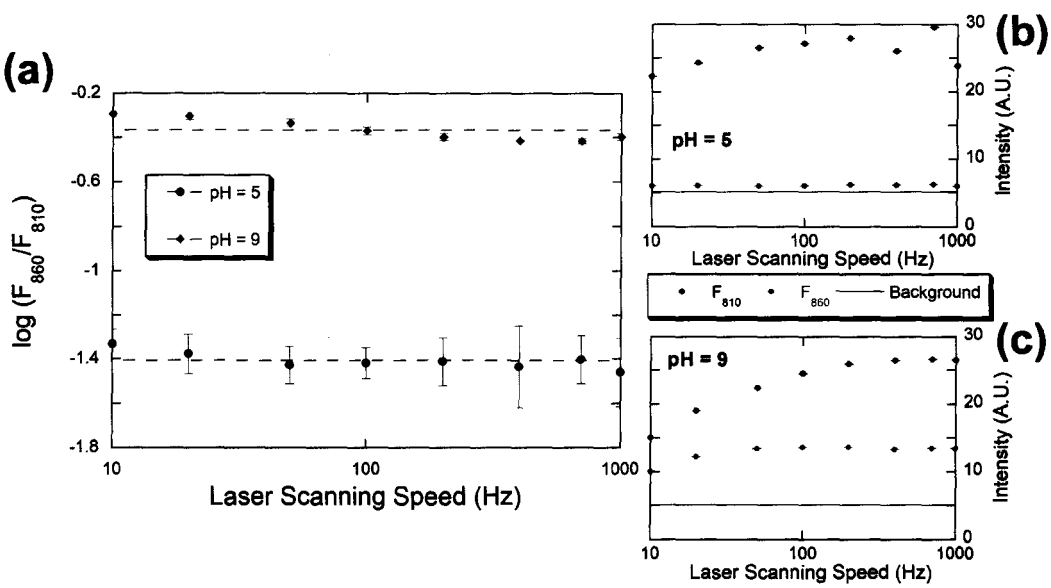

Figure 4.5. (a) Log(F_{860}/F_{810}) for pyranine (pH = 5 & 9) measured at various laser scanning speeds with two-photon excitation. (b) Fluorescence intensity of pyranine measured at (b) 810 & (c) 860 nm excitations. Horizaontal lines show the estimated background intensity.

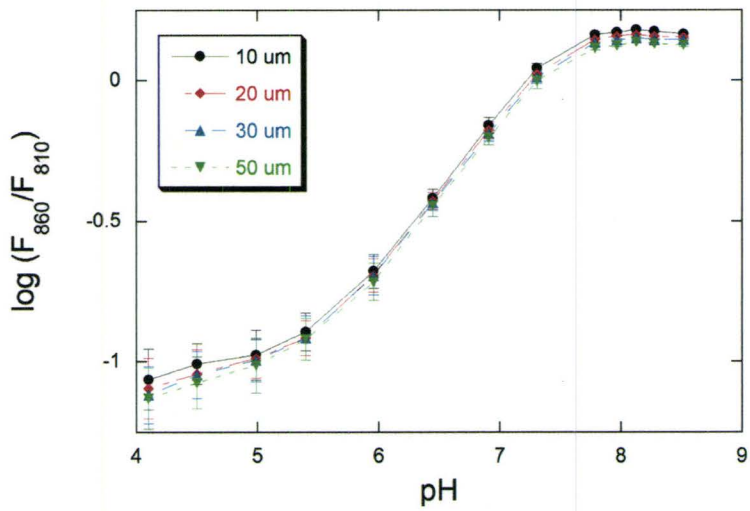

Figure 4.6. pH calibration curves of pyranine obtained in focal planes placed at different distances from the cover slip surface.

4.3.4 Immunolabeling of μ-opioid receptors

To test the presence and location of μ-opioid receptors in HEK293-MOR cells, I used immunolabeling against the receptor, and a secondary antibody labeled with Alexa Fluor 546. I performed the same immunolableing procedure on wt-HEK293 cells as a negative control. Figure 4.7 illustrates several confocal and DIC images of wt-HEK293 and HEK293-MOR cells treated with or without DAMGO and Tween 20. The addition of DAMGO to HEK293-MOR should induce endocytosis and internalize the μ-opioid receptors. Meanwhile, it should have no effect on the wild-type cells. Tween 20 permeabilizes the cell membranes; therefore, it should allow antibodies to penetrate in the cell and to bind to internalized receptors. The intensity levels of the four fluorescence images shown in Figure 4.7 were rescaled in exactly the same way to allow comparison and better visualization.

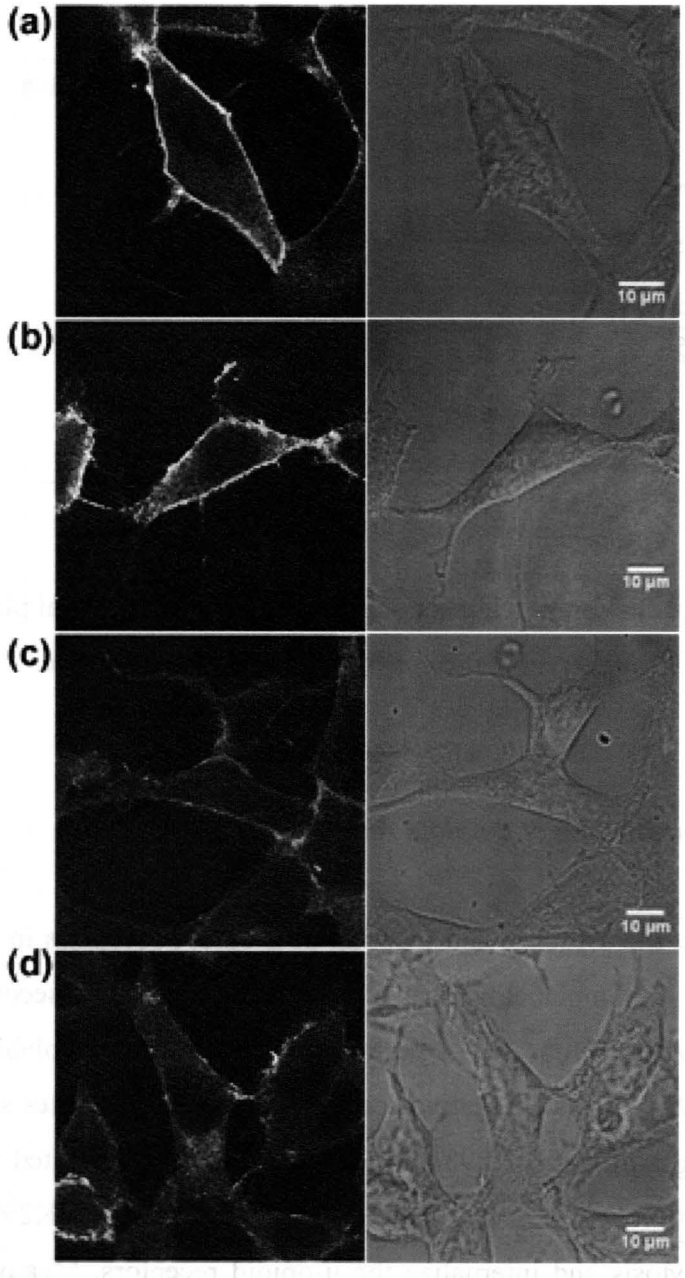

Figure 4.7. Confocal (left) & DIC images (right) of HEK293-MOR cells with fluorescently labeled μ-opioid receptors. (a) DAMGO (-) and Tween 20 (-). (b) DAMGO (-) and Tween 20 (+). (c) DAMGO (10 μM) and Tween 20 (-). (d) DAMGO (10 μM) and Tween 20 (+). The intensity levels of the fluorescence images were rescaled for better visualization.

Table 4.1: Net average fluorescence intensity per pixel measured in the cytosol of HEK293-MOR and wt-HEK293 cells with/without adding DAMGO and Tween 20.

	Net Average Fluorescence Intensity Per Pixel in the Cytoplasm			
	With Permeabilized Cell Membrane		With Intact Cell Membrane	
	With DAMGO	No DAMGO	With DAMGO	No DAMGO
HEK293-MOR	17.3 ± 0.1	15.16 ± 0.06	14.91 ± 0.08	13.85 ± 0.08
Wt-HEK293	6.15 ± 0.05	10.58 ± 0.06	1.72 ± 0.04	7.84 ± 0.05

Background intensity for HEK-293 cells = 3.88 ± 0.01.

To quantify receptor internalization, average intensities per pixel were measured in the cytosol of the transfected and the wild-type cells. The areas of the cytoplasm shown in the fluorescence images were first determined on the DIC images, and the average fluorescence intensities were calculated in those areas. Then, net average intensities were calculated by subtracting the background intensity. The background intensity was determined at the cytosol of HEK 293 cells without going through the labeling procedures, and I found that there was no significant difference between background obtained from HEK293-MOR and wt-HEK293 cells. Net average intensities are tabulated on Table 4.1. The results indicate that the fluorescence measured in the cytosol of wild-type cells is stronger than the background. Since no μ-opioid receptor is expressed in the wild-type cells, the fluorescence at the cytoplasm may be due to non-specific binding of the antibody. Also, the net fluorescence in the cytosol of HEK293-MOR cells is stronger than for wild-type cells, so this could indicate the existence of μ-opioid receptors in the cytoplasm. It may be combined with a residual signal coming from fluorescence at the membrane.

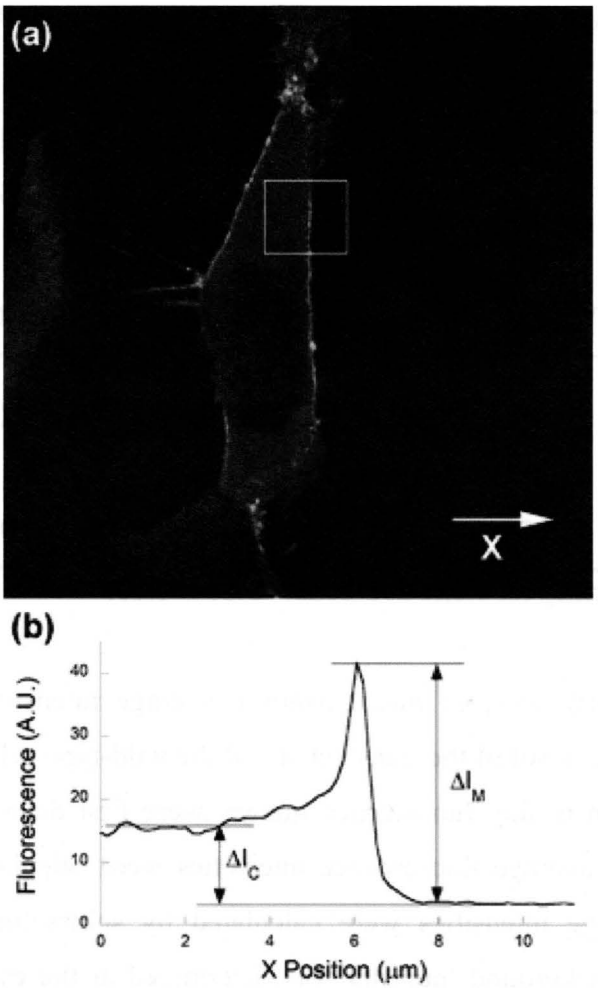

Figure 4.8. (a) Confocal image of fluorescently labeled μ-opioid receptors on HEK293-MOR cells with intact membrane in the absence of DAMGO. (b) Average 1-D intensity profile in the selected area shown on (a). The ratio of intensity, $\Delta I_C/\Delta I_M$, was determined to be 0.32 in this particular example. The levels of the fluorescent image were adjusted for the purpose of better illustration.

The internalization of μ-opioid receptors is expected to decrease the amount of receptors on the cell membrane; hence, it should decrease the fluorescence emission at the membrane, while increasing the fluorescence emission in the cytosol. The amount of receptors in the cytosol compared to the

membrane can be evaluated from the ratio of intensity, $\Delta I_C/\Delta I_M$, where ΔI_C is the net average intensity emitted in the cytosol, and ΔI_M is the net peak intensity emitted on the cell membrane. The 1-D intensity profile on Figure 4.8 provides an illustration of ΔI_C & ΔI_M. Both ΔI_C and $\Delta I_C/\Delta I_M$ are expected to increase when the μ-opioid receptors internalize as a result of endocytosis. To determine the ratio of intensity, first, the confocal image was rotated until a portion of the cell membrane aligned vertically as shown on Figure 4.8a, and a box was selected over the region with the vertically aligned membrane. After that, the average intensity profile of the horizontal axis in the selected area was determined by using a build-in function in ImageJ. The values of ΔI_C and ΔI_M were determined in the intensity profile as illustrated on Figure 4.8b. Then, the average values of $\Delta I_C/\Delta I_M$ were calculated by averaging the values obtained from more than 10 cells on multiple images, and the results are tabulated on Table 4.2. The errors on each measurement are the standard errors. The results show that the ratios increase after the cells were exposed to DAMGO, which indicates that there is a decrease in μ-opioid receptors on the membrane, compared to internalized receptors as well.

Table 4.2: Average ratio of intensity measured on HEK293-MOR cells with intact or permeabilized membrane and with (+) or without (-) adding DAMGO.

	Average ratio of intensity, $\Delta I_C/\Delta I_M$			
	With Permeabilized Cell Membrane		With Intact Cell Membrane	
	With DAMGO	No DAMGO	With DAMGO	No DAMGO
HEK293-MOR	0.63 ± 0.02	0.44 ± 0.03	0.49 ± 0.04	0.26 ± 0.03

4.3.5 pH measurement in pyranine-loaded vesicles

The ratiometric pH imaging method was applied to measure temporal pH changes in pyranine-loaded vesicles. The creation of pyranine-loaded vesicles in the cells was triggered by the addition of pyranine and DAMGO to the medium. The presence of DAMGO should trigger endocytosis and lead to the uptake of pyranine. In addition, the pyranine-loaded vesicles should carry μ-opioid receptors. I first verified whether there was a spontaneous uptake of pyranine into cells, and I found that pyranine is uptaken into the HEK293-MOR cells even without adding DAMGO. This spontaneous uptake of pyranine is also observed in wt-HEK293 cells. Since pyranine is membrane impermeable [34-36, 64], no pyranine leakage is expected across the cell membrane, thus this must be due to spontaneous endocytosis. After varying incubation conditions with pyranine, I found that no significant amount of pyranine is observed in the cells when they are incubated at room temperature for < 10 minutes without DAMGO. In fact, temperature is the major factor to induce spontaneous loading of pyranine in the HEK 293 cells, because there is significant amount of pyranine observed in the cells with only 1 minute incubation at 37°C without DAMGO.

Figure 4.9 shows the result of a temporal pH measurement of pyranine-loaded vesicles in HEK293-MOR cells after incubating with 57 μM pyranine and 17 mM DAMGO at room temperature for 2 minutes. Figure 4.9a illustrates the time lapse pH maps for a 10-minute measurement, while the time zero measurement was roughly 20 minutes after finishing sample preparation. In addition, Figure 4.9b shows the temporal pH change measured in the two vesicles. Figure 4.10 shows another measurement on the same sample. For this series of images, imaging began roughly 40 minutes after finishing sample preparation, which was ~ 10 minutes after the previous measurement. Figure 4.8a shows pH and DIC images for a few selected frames during a 20-minute measurement, and

Figure 4.10b shows the average temporal pH change of the vesicles. After that, another sample was prepared by incubating the HEK293-MOR cells with 57 μM pyranine and 67 mM DAMGO at room temperature for 5 minutes. Figure 4.11a shows few selected pH and DIC images of the sample during a 10-minute measurement. Furthermore, Figure 4.11b shows the temporal pH change in two selected areas shown in Figure 4.11a. The start of this measurement was roughly 10 minutes after the last step of the sample preparation. According to the estimated start time of the three measurements after sample preparation, the temporal pH change in the pyranine-loaded vesicles is summarized as shown in Figure 4.12.

The last example illustrated in Figure 4.13 is an investigation of spontaneous loading of pyranine in HEK293-MOR cells. The sample was incubated with 57 μM pyranine at 37°C for 5 minutes without DAMGO. Figure 4.13a shows few selected frames of pH maps and the corresponding DIC images in a 10-minute measurement. The temporal pH changes in the two selected areas were measured, and the results are illustrated on Figure 4.13b. In this measurement, the first image was taken ~ 5 minutes following sample preparation.

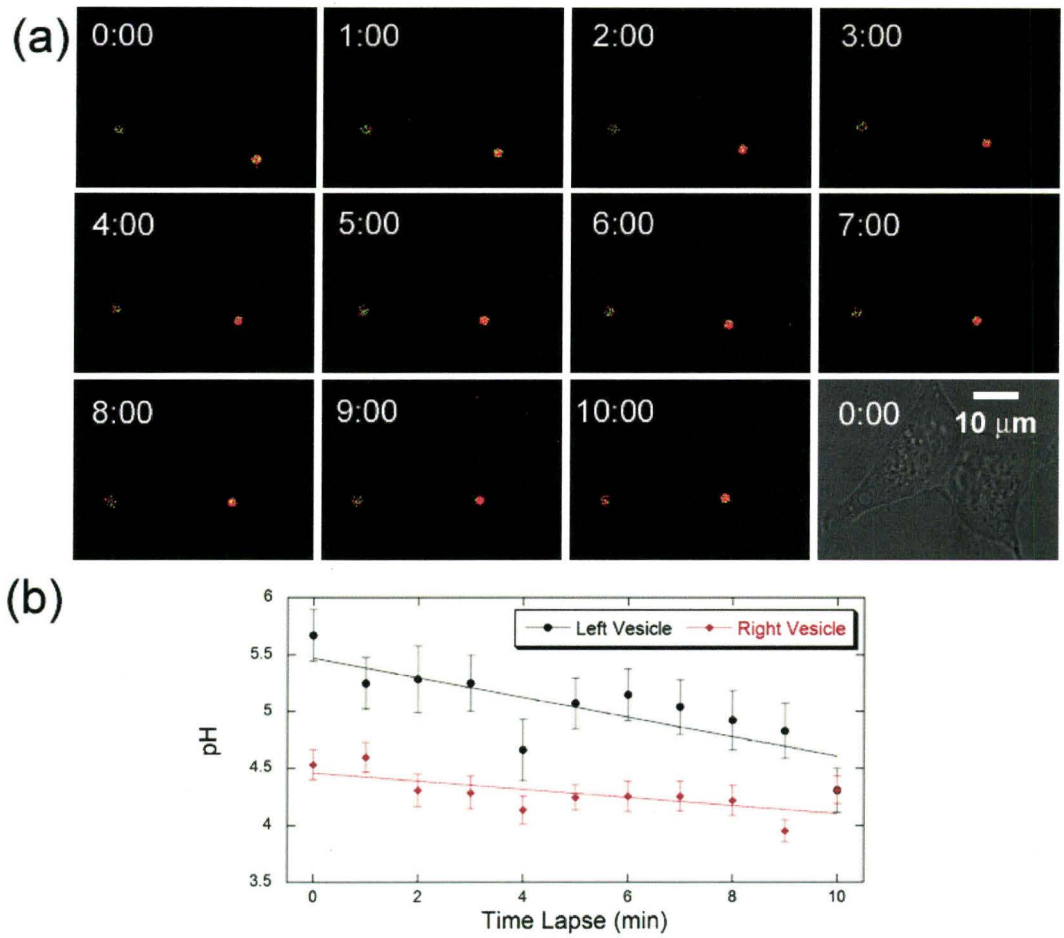

Figure 4.9. (a) Time lapse pH maps of HEK293-MOR cells exposed to 17 mM DAMGO in a 10-minute measurement, and DIC image at time zero. (b) pH measured in each of the two pyranine-loaded vesicles as a function of time. The straight lines serve as a guide visually to indicate the overall trend of pH decrease.

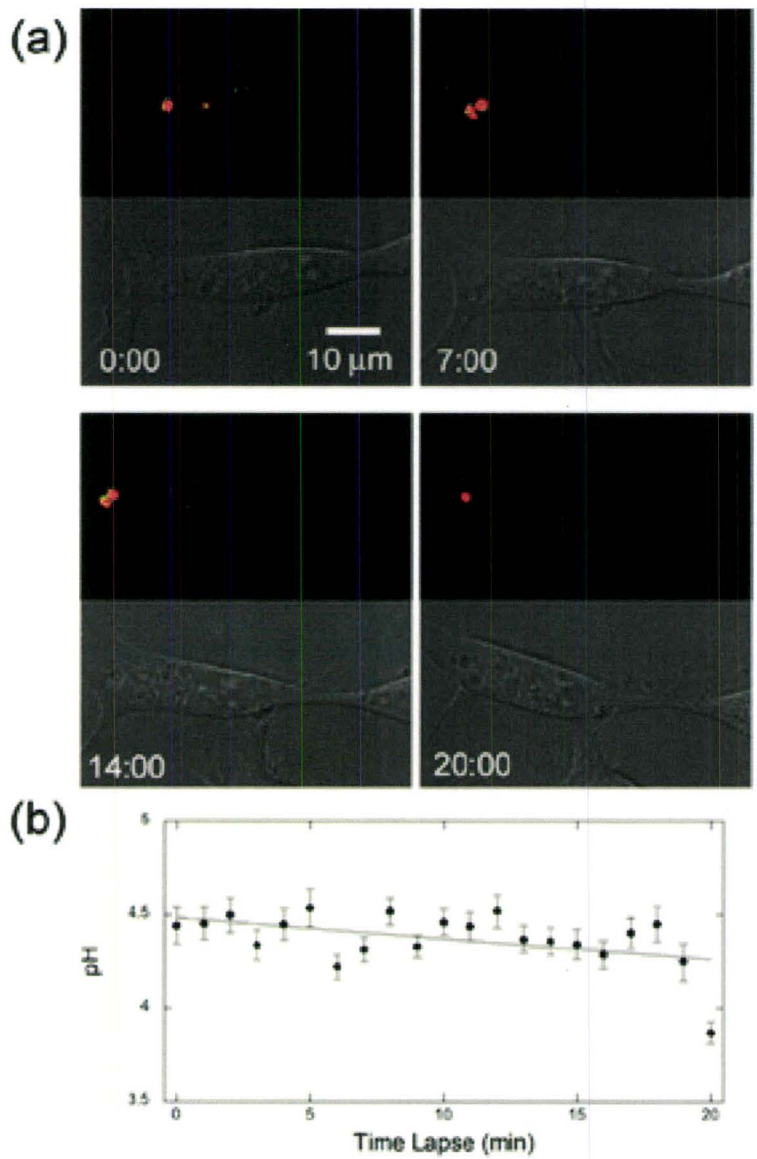

Figure 4.10. (a) Selected pH maps & DIC images of HEK293-MOR cells exposed to 17 mM DAMGO during a 20-minute measurement. (b) Average pH measured for the two vesicles in pH maps as a function of time. The straight line serves as a guide visually to indicate the overall trend of pH decrease.

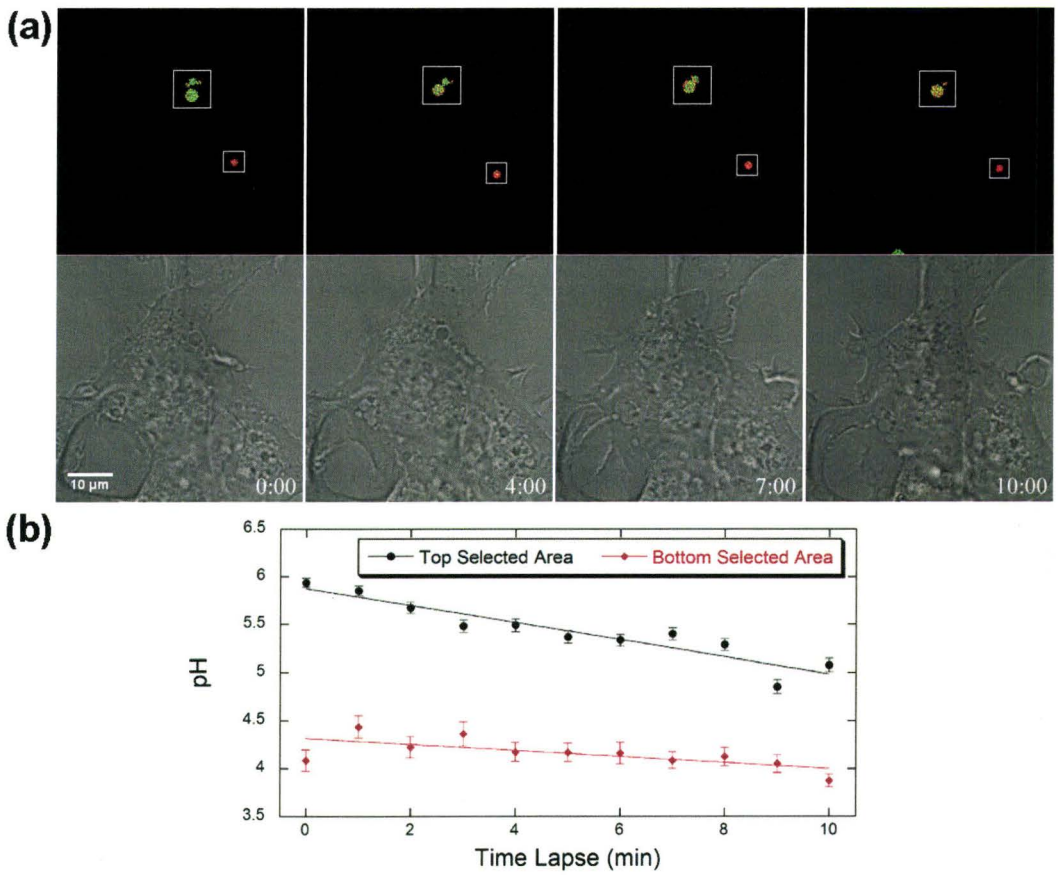

Figure 4.11. (a) pH maps & DIC images for selected frames in a 10-minute observation of HEK293-MOR cells exposed to 67 mM DAMGO. (b) Temporal pH change measured in the two selected area in (a). The straight lines serve as a guide visually to indicate the overall trend of pH decrease.

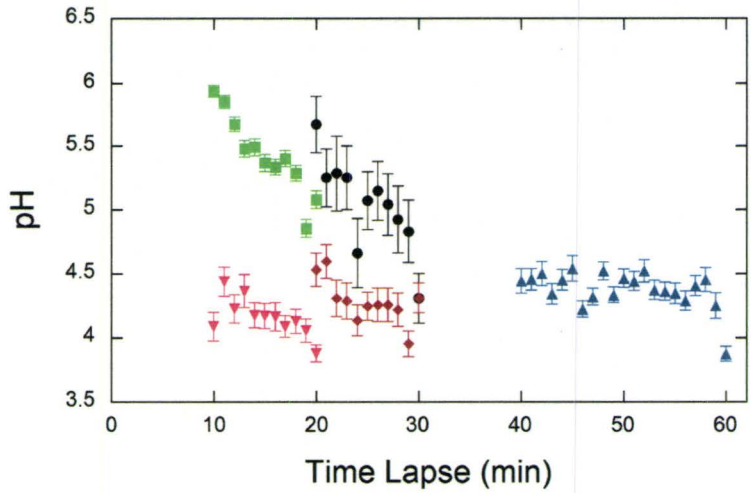

Figure 4.12. A summary of measured pH change as a function of time after sample preparation. Data with different colours are measurements in various vesicles of different samples.

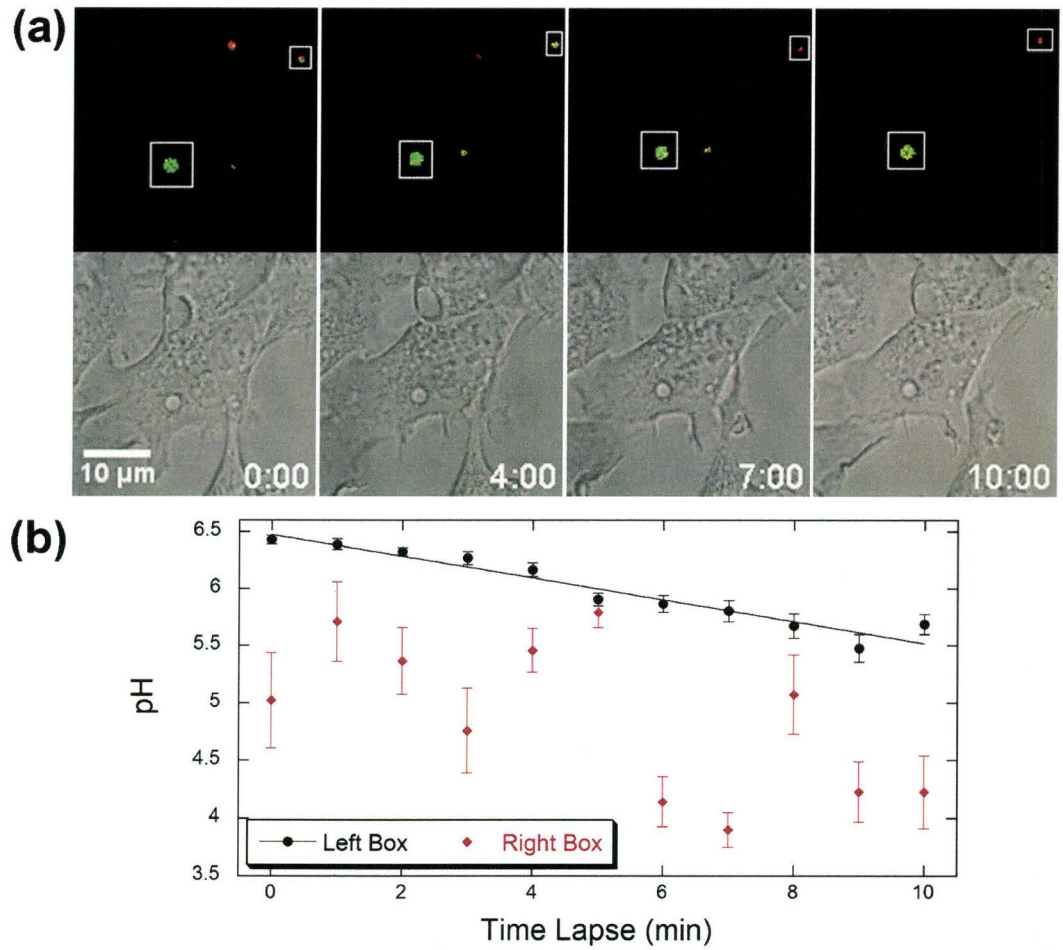

Figure 4.13. (a) pH maps & DIC images of selected frames in a 10-minute measurement of HEK293-MOR cells showing spontaneous pyranine loading. (b) Temporal pH changes measured in the two selected are as shown in (a). The straight line serves as a guide visually to indicate the overall trend of pH decrease.

4.4 Discussion

4.4.1 Ratiometric pH imaging in two-photon excitation

Pyranine is a well studied ratiometric fluorophore in single photon excitation [33-36, 64]; however, there is no information in the literature as to how pyranine would behave as ratiometric pH probe in two-photon excitation. Therefore, my work is to our knowledge the first application of ratiometric pH imaging using pyranine and two-photon excitation. In this study, I examined the ratiometric properties of pyranine by measuring its two-photon excitation spectrum. The excitation spectra of pyranine measured at various pH directly shows the change in fluorescence emission for different excitation wavelengths, including excitation maxima, which allowed choosing optimal excitation wavelengths for the ratiometric pH imaging. This suggests that other ratiometric dyes could be used for two-photon ratiometric imaging. In Figure 4.2, the two-photon excitation spectrum of pyranine at low pH (pH = 5) closely resembles the one-photon absorption spectrum shown in refs. [34] & [64]. However, at higher pH (pH = 7.4 & 9.5), the shapes are different between the two-photon excitation and the absorption spectra. This discrepancy may come from the difference in absorption cross section of pyranine with one- or two-photon excitation, or from the presence of one-photon absorption events not leading to fluorescence. A more in depth study would be necessary to fully characterize the two-photon excitation spectrum of pyranine. For example, it could be compared to single photon excitation spectrum, and further care could be taken to remove any instrumental artifacts.

The pH calibration curve in Figure 4.3 shows that the optimal working range of pyranine for ratiometric pH imaging with two-photon excitation is between pH 5.5 and 7.5. At pH $\geq$ 8, the $\log(F_{860}/F_{810})$ values remain constant, and

pH cannot be measured. At pH $\leq$ 5.5, there is still a small change in $\log(F_{860}/F_{810})$, so it is possible to measure pH, but the result may be less accurate. Furthermore, I found that the slope of the linear region of the pH calibration curve (5.5 $\leq$ pH $\leq$ 7.5) is roughly 0.5. In contrast, a previous study had shown that the slope in the linear region (4 $\leq$ pH $\leq$ 7.5) is around 1 for single photon excitation [34]. According to Henderson-Hasselbalch equation, $pH = pK_a + \log([A^-]/[AH])$. In order to have a slope of 1 on the calibration curve, the fluorescence intensities measured at 810 and 860 nm excitation must be proportional to the concentration of protonated and deprotonated pyranine respectively. For a weak acid like pyranine, the concentration of the protonated form is expected to decrease to zero at high pH, while the concentration of the deprotonated form should drop to zero at low pH. The fluorescence intensity at Figure 4.3b indicates that F860 at low pH does not drop to zero (background signal). Also, at high pH, the F_{810} still remains in high intensity as shown in Figure 4.2 and 4.3b. The strong fluorescence background intensity could be the result of wider two-photon absorption spectra for each pyranine form, which results in the excitation of the two pyranine forms with the chosen wavelengths [97]. As a result, the fluorescence intensities at the two chosen excitation wavelengths are not directly proportional to the concentration of the two pyranine states. This is likely the cause of the leveling off of the calibration curve at low and high pH, and of the decrease in slope of the linear region. Nevertheless, this difference in slope does not prevent using pyranine as the probe for two-photon ratiometric pH determination.

Ratiometric pH imaging with single photon excitation has already been shown to be a robust method for *in vivo* measurements, because the measurement is insensitive to fluorophore concentration. Result on Figure 4.4 indicates that the fluorescence ratio is insensitive to pyranine concentration at concentration $\geq$ 0.03 g/l (57 μM), while there is a slight drop in fluorescence ratio at lower pyranine concentration. The drop in $\log(F_{860}/F_{810})$ may be due to the difficulty to accurately

quantify fluorescence when approaching low signal-to-noise ratio (as happens at low fluorophore concentration). With the confocal microscope, 0.03 g/l (57 μM) therefore represents the lowest pyranine concentration at which we can work with that particular instrument. In the cell experiments, the samples were incubated only with 0.03 g/l (57 μM) pyranine, but the concentration of pyranine in the vesicles that I measured is likely to be higher than 0.03 g/l (57 μM). For example, in the first cell measurement (Figure 4.9), the average intensity of the left vesicle measured in the first 810 nm image is 45 ± 2, and the intensity is 198 ± 9 in the right vesicle. By comparing the intensity to the F_{810} shown in Figure 4.3b, the pyranine concentration of the left vesicle was ~ 0.12 g/l (0.23 mM), and of the right vesicle was ~ 0.53 g/l (~ 1 mM). Although the concentration measurement based on intensity could introduce a higher uncertainty, it is likely that the vesicles contained > 0.03 g/l (57 μM) pyranine. Consequently, the pyranine concentration used in the live-cell pH measurements fulfilled the concentration limit in order to generate reliable results. In fact, the pyranine concentration either in solution or in cell shown in this chapter was at least 100 times higher than the samples used in FCS that described on chapter 3. So, it is impossible to obtain FCS measurement under this pyranine concentration.

In addition, Figure 4.5 shows that the fluorescence ratio is different at lower laser scanning speed. The laser scanning speed changes the dwell time of the laser beam at in each pixel. For long duration of illumination at a single point, photobleaching at that spot becomes more severe, so it could affect the measured fluorescence ratio. Results in Figure 4.5b and 4.5c suggest that there is photobleaching at low laser scanning speed (< 200 Hz), as shown by a decrease of intensity measured in an identical sample. For *in vivo* measurements, using slow laser scanning speed to take confocal images should be absolutely avoided. Since there is a limited amount of fluorophore in each cells, photobleaching at slow laser scanning speeds will further increase the depletion of fluorophores.

By combining ratiometric pH imaging and two-photon excitation microscopy, a few extra advantages are added to this pH measurement technique. pH measurement by ratiometric imaging is independent of fluorophore concentration due to the built-in corrections for slight concentration variation, which is the major advantage of this approach. In addition, two-photon excitation allows a deeper penetration of photons into a sample due to the reduction of light scattering at longer wavelength, so measurement can be taken deeper in the sample. Also, if we want to excite pyranine using single photons, it requires an excitation energy close to ultraviolet (400/450 nm). Since light close to ultraviolet induces strong autofluorescence in biological sample, switching to NIR illumination in two-photon excitation can greatly reduce autofluorescence in the sample. Although two-photon excitation requires higher laser power than one-photon excitation, photodamage to the biological sample is reduced with two-photon excitation due to the poor tissue absorption of near infrared light. Finally, the possibility to use a tunable laser for two-photon excitation means that a single laser can be used for the two excitation wavelengths. It eliminates the need to align two different lasers in the same confocal instrument, and reduces the risk to obtain non-superposable images. Therefore, it makes pixel-by-pixel pH imaging more reliable.

4.4.2 Immunolabeling of μ-opioid receptors

Internalization of μ-opioid receptors is expected in HEK293-MOR cells after treatment with DAMGO. Then, if using immunolabeling against the receptor, fluorescently labeled vesicles should be observed in the cytoplasm of the transfected cells, as in the confocal images shown in ref. [98]. However, my results on Figure 4.5 showed no fluorescently labeled vesicle in the cytosol of HEK293-MOR cells after the sample was treated with DAMGO and fluorescently

labeled. Also, the quantification of the fluorescence measured in the cytosol shows a very small increase in cytosol fluorescence of the transfected cells with DAMGO treatment, compared to the cells without DAMGO treatment. In Table 4.1, the errors on the intensities are the standard error calculated from the average of multiple cells. However, evidence shows that the standard errors are an underestimate of the real errors for the intensities. The average cytosol intensities should agree with each other for the membrane permeabilized wt-HEK293 cells or the wt-HEK293 cells with intact membrane whether they were exposed to DAMGO or not. The reason is that since no epitope-tagged μ-opioid receptor is found on the wild type cells, the immunolabeling should show negative results. In addition, the antibody complexes for immunolabeling cannot penetrate into the cells with intact membrane, so the cytosol intensities of HEK293-MOR cells with intact membrane should be in agreement even if the cells were treated with DAMGO. As a result, the errors of the measured cytosol intensities are probably larger than the standard errors shown on Table 4.1, and the errors could be up to ±6. Then, it is most likely that the results did not clearly indicate the presence of μ-opioid receptors in the cytoplasm after the HEK293-MOR cells were exposed to DAMGO. In this case, the higher cytosol intensities of the HEK293-MOR cells shown on Table 4.1 could be the result of the fluorescence emitted from the top or the bottom membrane of the cells, which were labeled fluorescently.

On the other hand, examination of the ratio $\Delta I_C/\Delta I_M$ suggests that there is a decrease in the amount of μ-opioid receptors on the membrane when the cells were treated with DAMGO. The decrease of μ-opioid receptors on the membrane is most likely the result of receptor internalization. Furthermore, the ratio $\Delta I_C/\Delta I_M$ for cells with a permeabilized membrane is less than for cells with an intact membrane. This indicates that there is a loss of μ-opioid receptors on the membrane when the lipid bilayer is permeabilized. Hence, this may be the explanation of why no fluorescently labeled vesicle is observed in the cytoplasm

of the DAMGO treated HEK293-MOR cells. Possibly, protein cross-linking process in sample preparation failed to anchor the internalized μ-opioid receptors in the cytoplasm. After the detergent dissolved the lipid bilayer of the endosomal vesicles, the internalized μ-opioid receptors might be washed away from the cytoplasm. One possible solution to fix this problem would be to apply a weaker detergent to create pores on the cell membrane rather than dissolving the lipid bilayer entirely. This may allow preserving some μ-opioid receptors inside the cells after adding the detergent. A potential solution to this problem is also suggested by my protocol comparing to other assays. Keith et al used a μ-opioid receptor cDNA containing FLAG epitope tag to transfect HEK 293 cells in the immunofluorescence experiment [98]. Mundell et al used transfected HEK 293 cells with HA-tagged metabotropic glutamate receptor (mGluR) and showed the fluorescently labeled receptors in the cytosol after the agonist-induced receptor internalization (agonist: glutamate) [99, 100]. The result indicate that the HA epitope tags should retain their immunoreactivity after the internalization of the receptors. Therefore, the combination of HA tags and μ-opioid receptors could lose the immunoreactivity after the receptor phosphorylation, and lead to no observable fluorescently for the labeled internalized receptors in the HEK293-MOR cells of my samples. As a result, switching epitope tag on the μ-opioid receptors might solve this problem. Regardless of the immunolabeling result of the internalized receptors, I showed that there are epitope tagged receptors on the membrane. I have also shown that these receptors disappear (likely internalized) in response to DAMGO. Therefore, the transfected HEK 293 cells are response to the agonist binding and receptor-mediated endocytosis might occur afterward.

4.4.3 In vivo pH measurement by ratiometric approach

The goal of the *in vivo* measurement I made was to determine the temporal pH change inside endosomal vesicles during receptor resensitization. The four

examples shown in section 4.3.5 prove that the ratiometric pH imaging with two-photon excitation can measure temporal pH changes in pyranine-loaded vesicles. The results also show that this method can measure a decrease in pH from ~ 6.5 to 4. Previous studies have already determined the pH of various intracellular vesicles in the endocytic pathway: early endosomes (pH = 6 – 6.2), late endosomes (pH = 5.5 – 6), and lysosomes (pH ≤ 5) (reviewed in ref. [101]). The results in Figure 4.12 show that pH in the pyranine-loaded vesicles has already dropped to < 6, as low as the pH found in late endosomes at roughly 10 minutes after the receptor internalization. Some of them have already been acidified to pH < 5 as early as just 10 minutes after the internalization, and eventually, the pH in the vesicles dropped to < 5, which is similar pH range as that of lysosomes. Although this measurement approach could measure the pH in pyranine-loaded vesicle in real time, further investigations are necessary to identify the nature of the pyranine-loaded vesicles. Even though no such vesicle was observed in control samples of wt-HEK293 cells and HEK293-MOR cells in the absence of DAMGO, it is still not certain whether the vesicles observed were actually the result of receptor-mediated endocytosis.

To apply ratiometric pH imaging for *in vivo* measurement, one must be aware that the temporal resolution of the confocal microscope can introduce significant error to the pH measurement. For the confocal microscope used in the present study, the temporal resolution depends on laser scanning speed, size of the image, and delay time for the tunable laser to switch wavelengths. Since the 810 & 860 nm confocal images are taken in sequence, long delay time between taking two confocal images can create mismatch between confocal images. Using faster scan rate and smaller image size can shorten the time to take a single confocal image, but the time to switch excitation wavelengths cannot be shortened due to the limitation from the tunable laser, which is ~0.5s for this confocal microscope. Therefore, the delay time due to the switch of excitation wavelength is the major

limitation on the temporal resolution of my measurements. In my results, there is no significant mismatch observed between confocal images at the same time frame, because the pyranine-loaded vesicles move slowly in the cells.

Another obstacle of the *in vivo* pH measurement is due to the spontaneous loading of pyranine which observed in both the transfected and the wild-type HEK 293 cells. First of all, what triggered this process is still unknown. Also, in order to suppress the spontaneous pyranine loading into the cells, I can only incubate the cells at room temperature for a short period of time. Therefore, it reduces receptor-mediated endocytosis in the samples; hence, it leads to the result of taking at least 10 minutes to search for pyranine-loaded cells in a sample. Previous studies have already indicated that the internalized receptors recycle back to the cell membrane from the early endosomes in just a few minutes at 37°C (reviewed at ref. [101]). Consequently, the long searching time on pyranine-loaded cells could limit the pH measurement in the endosomal vesicles for the receptor resensitization. Therefore, more work is needed to understand this spontaneous endocytosis in the HEK 293 cells.

Future works are required in order to identify the optimal pH condition to dephosphorylate μ-opioid receptors *in vivo*. First, instead of immunolabeling fixed cell sample, the staining process should be done on the live cells, in order for the receptor internalization to be observed in real time during the receptor-mediated endocytosis. Second, the nature of the pyranine-loaded vesicles in the cells needs to be identified. LysoTracker probe can be applied to determine the location of lysosome in the cells. Although LysoTracker probe has high selectivity to stain acidic organelle, it may not have the ability to distinguish lysosome and acidic endosomal vesicle. We can solve this by labeling lysosome first before the addition of DAMGO, so the endosomal vesicles created afterward should contain no LysoTracker. Also, dual staining of lysosomes and μ-opioid receptors can also

provide information on the amount of receptors transported to lysosomes during the internalization. Finally, pyranine can be added to the sample when triggering endocytosis in the immunofluorescence cells. If the pyranine loaded vesicles are created by the receptor-mediated endocytosis, colocalization of pyranine and the immunolabeled internalized receptors should observe. Hence, the nature of the vesicles can be determined.

Chapter 5

Conclusion

The focus of this thesis was to develop pH and temperature measurement methods which are suitable for the study of biological systems. Two original measurement approaches have been introduced; both of them are based on the environmental sensitivity of proton transfer in fluorophores. The first method is based on the determination of fluorescence fluctuations due to fluorophore blinking, in which, the blinking is the result of the reversible protonation of the fluorophore. By using FCS, the blinking can be studied using autocorrelation analysis, and the measured blinking parameters (fraction of protonated molecules and relaxation time) are used as gauges to concurrently probe pH and temperature. The second method is a two-photon ratiometric pH measurement allowing to construct pH images of a sample. This method is based on the comparison of the fluorescence of a ratiometric dye when excited at two different wavelengths. Since the ratio of these two fluorescence signal is sensitive to pH, it can be used to measure pH by imaging the sample using a confocal microscope. By using two-photon instead of one-photon excitation, the ability of the ratiometric pH imaging method to study biological systems was further enhanced.

This first method presents multiple advantages. First, this approach provides absolute pH and temperature measurements. Also, I have shown that the accuracy of this method is independent of typical FCS experimental conditions. Furthermore, it allows measuring steep pH and temperature gradients with good spatial resolution. On the other hand, one major limitation of this temperature measurement, which is based on blinking relaxation time, is that this parameter remains sensitive to pH and buffer composition; therefore, a specific temperature

calibration curve should be obtained for each buffer and pH. The pH measurement, which relies on the fraction of protonated fluorophore, on the other hand, is robust against buffer condition. Since it is difficult to know the exact buffer and salt concentrations in cells; preparing a calibration curve in cells rather than in solution should be completed in order to provide more accurate *in vivo* measurement.

A few advantages have also been suggested in pH measurement using the ratiometric method with two-photon excitation. This method can be integrated to any two-photon confocal microscope easily, and allows direct observation of the cellular process through the confocal images. The method is insensitive to slight change in fluorophore concentrations. Two-photon microscope using NIR allows imaging a thicker sample and it also reduces photodamage to the biological tissues. Also, autofluorescence in the sample is further reduced by using a NIR excitation light. Furthermore, the tunable laser in the two-photon microscope can reduce the chance of getting non-superposable images due to the poor alignment of lasers. One major obstacle of this method is the temporal resolution of the confocal microscope for obtaining two confocal images. It could introduce significant error in pH due to system with poor temporal resolution or fast moving objects in the sample.

As an example, I showed the temperature measurement using the EGFP blinking to characterize the temperature change at the laser focus due to laser induced heating. This method has the potential to be applied directly in biological samples using genetically encoded fluorescent protein fusions. Using appropriate variants of fluorescent protein with observable temperature dependence should lead to precise temperature determination under normal physiological condition. Also, this method could determine the localization, the mobility, as well as acidity and thermal environment found for a particular cellular reaction. This could

provide large amount of information in just a single measurement. Together with immunolabeling, I studied the temporal pH change in pyranine-loaded vesicles induced by the exposure of DAMGO to the HEK293-MOR cells using the ratiometric pH imaging method. However, future work is needed to identify whether the pyranine-loaded vesicles are induced by receptor-mediated endocytosis and to improve the sample preparation to measure the initial pH change in the sample.

Appendix A
Fluorescence Correlation Spectroscopy

A.I Basic concept

Fluorescence correlation spectroscopy (FCS) is a fluorescence technique that allows characterizing the dynamics of fluorophores by measuring fluorescence fluctuations in the sample. The fluorescence fluctuations are often due to the diffusion of fluorophores across the confocal detection volume, but some can also be due to the blinking of the fluorophores induced by different photophysical processes. The measured fluorescence fluctuations are analyzed by using temporal autocorrelation, where an autocorrelation function is the result of the analysis. By using various fitting models, we can determine the physical characteristics of the fluorophores present in the sample: for instance, average number of fluorophore and average residence time of the fluorophore in the observation volume. In addition, FCS can be applied to measure the relaxation time of various photophysical processes such as triplet transition and reversible protonation process.

A.II FCS setup

The experimental setup of FCS is based on that of a confocal microscope. In chapter 2 & 3, I have already discussed how one could use FCS to measure the blinking of EGFP and pyranine. These measurements were completed using two different FCS systems, a home built system (described in ref. [86]) and a commercial system (Evotec Technologies Insight Cell, Hamburg, Germany). Figure A1 shows a schematic diagram of the home built FCS system. The home

built system contains two lasers, a 488nm argon-ion laser (Melles Griot, Carlsbad, CA) and a 442nm He-Cd laser (Liconix, Santa Clara, CA, U.S.A.). The laser beam first passes through a variable neutral density filter (Thorlabs, Newton, NJ, U.S.A.) to adjust the excitation power. The laser beam is then passing through two lenses forming a beam expander, so that the beam size can be either expanded or shrunk (in effect by either replacing the lens or putting an adjustable iris on the beam path). Meanwhile, changing the laser beam size changes the size of the observation volume. The power of the laser beam is measured by an optical power meter (Newport, Irvine, CA, U.S.A.), which can be placed before the back port of the inverted microscope (Nikon Eclipse TE2000-U, Nikon, Tokyo, Japan).

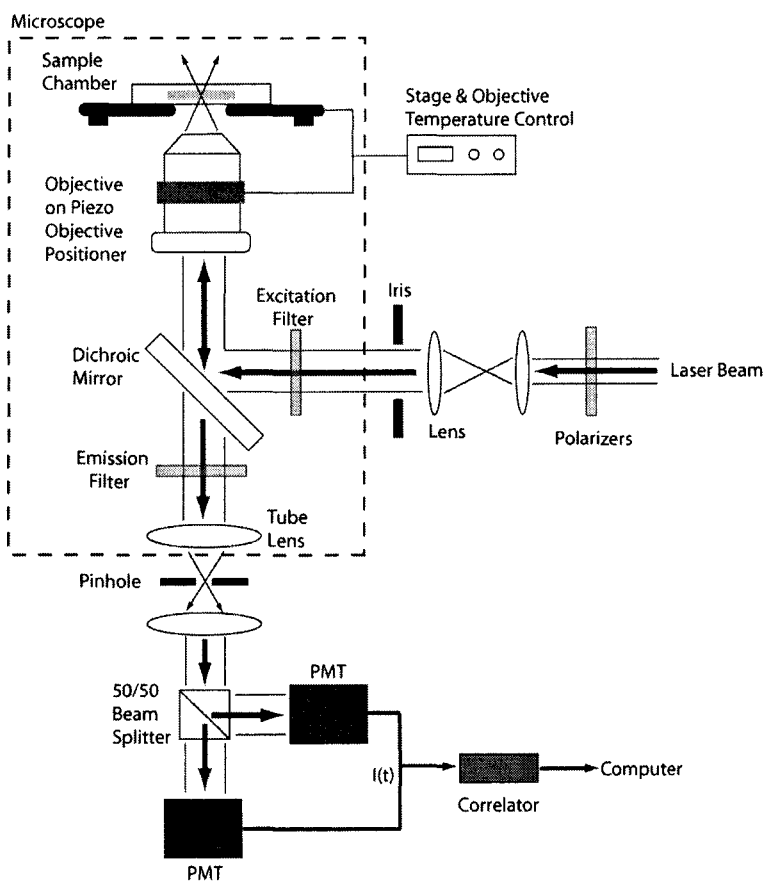

Figure A1. Schematic diagram of the home built FCS system.

When the laser beam is directed into the microscope, it first passes through a filter set. Different filter sets can be placed in the microscope (11008v2 for 442nm excitation and 41001 for 488nm, both purchased from Chroma, Rockingham, VT, U.S.A.), and each filter set includes an excitation filter, a dichroic mirror, and an emission filter. After the laser beam passes through the band pass excitation filter, the dichroic mirror reflects the beam upward to the back aperture of the microscope objective, either an air immersion objective (Plan Apo, 60x 0.95NA, Nikon, Tokyo, Japan) or a water immersion objective (Plan Apo, 60x 1.2NA, Nikon, Tokyo, Japan). The objective focuses the laser beam in the sample and collects the emitted fluorescence at the same time. After that, the emitted light passes through the dichroic mirror and the emission filter, and it is later focused through a pinhole to remove out-of-focus signal. Five different pinhole sizes have been used, 50-, 75-, 100-, 150-, and 200-μm diameter (all purchased from Thorlabs, Newton, NJ, U.S.A.), and the choice of the pinhole depends on the size of the laser focus. After passing through the pinhole, the emitted fluorescence is splitted by a 50/50 beam splitter (Chroma, Rockingham, VT, U.S.A.), and the intensity of each beam is detected by a different photomultiplier tube (H7421, Hamamatsu Photonics, Hamamatsu City, Japan), and fed into a multiple-tau correlator (Flex02-08D, Correlator.com, Bridgewater, NJ, U.S.A.) for signal correlation analysis. Using two photomultiplier tubes can eliminate the correlated noise coming from an individual detector during the autocorrelation analysis. The temporal intensity and autocorrelation functions are then sent to a PC from the correlator. A user interface program was written by Daniel Banks using LabView (National Instruments, Austin, TX, U.S.A.) [102]. This interface program can control some components of the FCS system and it is able to perform data acquisition. During the FCS measurement, the program can display the autocorrelation function and temporal intensity profile in real time. Furthermore, the home-built system gives the possibility to control sample temperature with an inverted microscope stage temperature control system (PE-

100NI, Linkam Scientific, Surrey, UK) and a custom water immersion objective temperature control (Linkam Scientific, Surrey, UK). The temperature control was an important piece of equipment when obtaining the temperature calibration curve of EGFP and pyranine.

The setup of the commercial built FCS system is similar to the home-built system with a few variations. First, the system is an integration of a confocal microscope and FCS components, so it is capable to take confocal image in addition to performing FCS. The system includes three lasers, a 488nm argon-ion laser, a 543nm HeNe laser, and a 647nm solid state laser, and the laser beams are directed into the microscope through optical fibers. Therefore, the system allows dual-colour illumination to a sample at the same spot, and it can measure the two emitted fluorescence separately through two photomultiplier tubes. As a result, the system could perform two autocorrelation measurements for two fluorescence signals and a dual-colour cross-correlation measurement. I used the dual colour illumination to excite EGFP using the blue laser and to induce light absorption in a sample using the red laser.

A.III Autocorrelation function analysis

After the temporal fluorescence intensity is measured, the result can be studied using autocorrelation analysis in order to characterize any fluctuation of fluorescence measured in the observation volume. The autocorrelation $G(\tau)$ of the fluorescence fluctuations for a lag time τ can be calculated from the fluorescence signal, F(t), using the following expression:

$$G(\tau) = \frac{\langle \delta F(t) \cdot \delta F(t+\tau) \rangle}{\langle F \rangle^2}$$

δF(t) is the fluctuation of fluorescence at time t, which can be described as the fluctuations in fluorescence about the average fluorescence $\langle F \rangle$, $\delta F(t) = F(t) - \langle F \rangle$. On average, the fluctuation in fluorescence is zero. If the fluorescence fluctuation is only due to the change of local fluorophore concentration within the effective detection volume, the fluctuations can be described in terms of the spatial distribution of the emitted light, the brightness per molecule, and the mobility of the fluorophores. As a result, the fitting equation of the autocorrelation G(τ) for a freely diffusing fluorophore can be derived as [103]:

$$G(\tau) = \frac{1}{N}\left(1 + \frac{\tau}{\tau_D}\right)^{-1}\left(1 + \frac{1}{S^2}\cdot\frac{\tau}{\tau_D}\right)^{-1/2}$$

N is the average number of fluorophore in the detection volume. τ_D is the average residence time of the fluorophore in the detection volume. S is the aspect ratio of the detection volume:

$$S = z_0 / w_0$$

w_0 and z_0 are the lateral radius and half of the axial length of the detection volume respectively. In addition, the effective detection volume can be expressed as [104]:

$$V = \pi^{3/2} \cdot {w_0}^2 \cdot z_0$$

When the fluorescent molecules are excited, some of them undergo intersystem crossing to the triplet state. Afterward, the fluorophores decay back to ground state through phosphorescence rather than fluorescence. Since the phosphorescence have longer lifetime than the fluorescence, the fluorophores appear to blink when undergoing the triplet transition. If the kinetics of the triplet transition does not alter the diffusion coefficient of the fluorophore, the overall autocorrelation function of the fluorophore is the multiplication of the autocorrelation function for the 3D diffusion and a term describing the blinking due to triplet transition. The derivative of this term is based on solving the rate

equations of fluorophore in different energy state: ground state S_0, first excited state S_1, and triplet state T_1. Consequently, the fitting equation of autocorrelation function described the freely diffusing fluorophore and its triplet blinking can be expressed as follows [49]:

$$G(\tau) = \frac{1}{N}\left(1+\frac{\tau}{\tau_D}\right)^{-1}\left(1+\frac{1}{S^2}\cdot\frac{\tau}{\tau_D}\right)^{-1/2}\cdot\left[1+\frac{T}{1-T}\exp\left(-t/\tau_T\right)\right]$$

Where T is the fraction of fluorophores in the triplet dark state, and τ_T is the relaxation time associated with the triplet transition. Since the kinetics of the blinking due to protonation and deprotonation of EGFP and pyranine can be expressed by similar rate equations as the triplet transition, this fitting equation can also be applied to analyze the autocorrelation function of EGFP and pyranine that undergo the reversible protonation process. In this case, T is the fraction of fluorophore in the protonated dark state, and τ_T is the relaxation time of the protonation / deprotonation reaction.

Appendix B

Calibration of Observation Volume

It is essential to calibrate the observation volume of the FCS system. First of all, it allows us to determine the dimensions of the observation volume and then measure the exact fluorophore concentration in the sample. Also, it helps determining the alignment of the FCS system. To calibrate the observation volume, fluorescein is used because it is a simple and well studied fluorophore. The confocal detection volume is a 3-D Gaussian which decayed to $1/e^2$ at w_0 in the lateral dimension and z_0 in the axial dimension. Usually, the shape of the observation volume can be thought of as an ellipsoid with half-width w_0 and half-height z_0. The calibration procedure includes the determination of autocorrelation functions of fluorescein in PBS. These autocorrelation functions can be then analyzed by the expression of freely diffused fluorophore:

$$G(\tau)=\frac{1}{N}\left(1+\frac{\tau}{\tau_D}\right)^{-1}\left(1+\frac{1}{S^2}\cdot\frac{\tau}{\tau_D}\right)^{-1/2}\cdot\left[1+\frac{T}{1-T}\exp\left(-t/\tau_T\right)\right]$$

The analysis yields average values for τ_D and S. Therefore, the radius of the lateral axis of the observation volume w_0 can be calculated as [103]:

$$\tau_D=\frac{w_0^2}{4D}$$

D is the diffusion coefficient of fluorescein, which is roughly 260 $\mu m^2/s$ at room temperature [86]. Once the value of w_0 is determined, the lateral axis of the detection volume z_0 can be calculated using the aspect ratio, $S = z_0 / w_0$. Then the effective confocal detection volume is calculated using, $V = \pi^{3/2} \cdot w_0^2 \cdot z_0$, and the exact fluorophore concentration in the sample is given by C = N/V. In addition, the aspect ratio can be fixed in the fitting equation for measurements taken under the same experimental conditions. Usually, the brightness per molecule of

fluorescein can be used as an indictor of the alignment of the FCS instrument, in which the system is aligned until achieving the highest brightness per molecule.

Appendix C

Derivation of Protonation/Deprotonation Kinetics

The chemical equation describing the reversible protonation process of EGFP or pyranine is:

$$A^- + H^+ \underset{k_d}{\overset{k_p}{\rightleftharpoons}} AH$$

A^- and AH are the deprotonated and protonated form of the fluorophore respectively. The differential rate equations of this reaction can be written as:

$$\frac{d[AH]}{dt} = -[AH]k_d + [A^-][H^+]k_p \quad \text{(C1)}$$

Also,

$$\frac{d[A^-]}{dt} = [AH]k_d - [A^-][H^+]k_p \quad \text{(C2)}$$

And,

$$\frac{d[H^+]}{dt} = [AH]k_d - [A^-][H^+]k_p$$

Eq. (C1) and (C2) can be solved as shown in the following:

$$\frac{d}{dt}\begin{pmatrix}[AH]\\ [A^-]\end{pmatrix} = \begin{pmatrix}-k_d & [H^+]k_p\\ k_d & -[H^+]k_p\end{pmatrix}\begin{pmatrix}[AH]\\ [A^-]\end{pmatrix}$$

$$[AH] = C_0 \frac{[H^+]k_p}{[H^+]k_p + k_d} + C_2 \cdot \exp\left(-t/\tau_B\right)$$

$$[A^-] = C_0 \frac{k_d}{[H^+]k_p + k_d} - C_2 \cdot \exp\left(-t/\tau_B\right)$$

Where τ_B is the characteristic decay time of the reversible protonation reaction (relaxation time), $\tau_B = \left([H^+]k_p + k_d\right)^{-1}$.

C_0 is the total concentration of the fluorophore, $C_0 = [AH]_0 + [A^-]_0$.

In the equilibrium state, $t \to \infty$

$$\lim_{t\to\infty}[AH] = C_0 \frac{[H^+]k_p}{[H^+]k_p + k_d} = [AH]_0$$

$$\lim_{t\to\infty}[A^-] = C_0 \frac{k_d}{[H^+]k_p + k_d} = [A^-]_0$$

As a result, the ratio of fluorophore in the protonated dark state can be expressed as:

$$B = \frac{[AH]_0}{C_0} = [H^+]k_p \cdot \tau_B$$

On the other hand, the fluorophore ratio in the deprotonated fluorescent state can be derived as:

$$1 - B = \frac{[A^-]_0}{C_0} = k_d \cdot \tau_B$$

The rate constants can therefore be expressed in function of the measured parameters B and τ_B:

$$k_p = \frac{B}{[H^+] \cdot \tau_B}$$

$$k_d = \frac{1-B}{\tau_B}$$

By definition, the equilibrium constant for the reversible protonation process of the fluorophore can be expressed as:

$$K = \frac{k_p}{k_d} = \frac{B}{1-B}\left(\frac{1}{[H^+]}\right)$$

The rate constants for protonation and deprotonation are expected to depend on temperature according to Arrhenius law:

$$k_p = A_p \exp\left(-E_p/RT\right)$$

$$k_d = A_d \exp\left(-E_d/RT\right)$$

A_p and A_d are frequency factors for protonation and deprotonation of the fluorophore respectively. E_p and E_d are activation energies for protonation and deprotonation of the fluorophore respectively. Therefore, the temperature dependence of the equilibrium constant and the blinking relaxation time are expected to have the form:

$$\ln(K) = -\frac{\Delta E}{R}\cdot\frac{1}{T} + \ln\left(\frac{A_p}{A_d}\right) \tag{C3}$$

$$\frac{1}{\tau_B} = [H^+]k_p + k_d = 10^{-pH}\cdot A_p \cdot \exp\left(-E_p/RT\right) + A_d \cdot \exp\left(-E_d/RT\right) \tag{C4}$$

Where $\Delta E = E_p - E_d$ is the difference in free energy between the protonated and deprotonated states.

Appendix D

ImageJ Javascript

Analysis of confocal images to create a 2D pH image by ratiometric pH imaging

```
import ij.*;
import ij.process.*;
import ij.gui.*;
import java.awt.*;
import ij.plugin.filter.PlugInFilter;

public class pH_map implements PlugInFilter
{

	protected ImageStack stack;

	public int setup(String arg, ImagePlus imp)
	{
		stack = imp.getStack();
		return DOES_8G + NO_CHANGES + STACK_REQUIRED;
	}

	public void run(ImageProcessor ip)
	{

		int w = stack.getWidth();
		int h = stack.getHeight();

		ImagePlus pH_image = NewImage.createRGBImage("pH Map", w, h, 1,
NewImage.FILL_RAMP);
		ImagePlus log_value = NewImage.createFloatImage("Log Value", w, h, 1,
NewImage.FILL_RAMP);
		ImageProcessor pH_ip = pH_image.getProcessor();
		ImageProcessor log_ip = log_value.getProcessor();

		ImageProcessor image_ch1 = stack.getProcessor(1);
		ImageProcessor image_ch2 = stack.getProcessor(2);

		int bkgd=30;

		int counter_max =0;
		int counter_min=0;
		int counter1=0;
		int counter2=0;
		int counter3=0;
		int counter4=0;
		int counter5=0;
		int counter6=0;
		int counter7=0;
		int counter8=0;
		int counter9=0;
```

```
int counter10=0;
double pH_value=0;

for (int i=0; i<w; i++)
{
	for (int j=0; j<h; j++)
	{
		int ch1 = image_ch1.getPixel(i, j);
		int ch2 = image_ch2.getPixel(i, j);

		if ((ch1==255) || (ch2==255))
		{
			counter_max++;
			int c=((255 & 0xff)<<16) | ((255 & 0xff)<<8) | 255 & 0xff;
			pH_ip.putPixel(i,j,c);
			log_ip.putPixel(i,j,1);
		}

		else if (ch1<=bkgd)
		{
			counter_min++;
			int c=((0 & 0xff)<<16) | ((0 & 0xff)<<8) | 0 & 0xff;
			pH_ip.putPixel(i,j,c);
			log_ip.putPixel(i,j,0);
		}

		else
		{
			double ratio = (double) ch2/ch1;
			double log_ratio = (double) Math.log(ratio)/Math.log(10);
			if (log_ratio <= -1.0673)
			{
				int c=((255 & 0xff)<<16) | ((0 & 0xff)<<8) | 0 &
0xff;
				pH_ip.putPixel(i,j,c);
				counter1++;
				if (log_ratio>-1.07563 && log_ratio <=-1.0673)
				{
					pH_value=4;
				}
				else if (log_ratio>-1.09523 && log_ratio <=-
1.07563)
				{
					pH_value=3.9;
				}
				else if (log_ratio <=-1.09523)
				{
					pH_value=3.75;
				}
				IJ.write("x, y, log(ratio), pH = "+i+", "+j+",
"+log_ratio+", "+pH_value);
			}

			else if (log_ratio > -1.0673 && log_ratio <=-1.01556)
			{
				int c=((255 & 0xff)<<16) | ((99 & 0xff)<<8) | 71
& 0xff;
				pH_ip.putPixel(i,j,c);
				counter2++;
```

```
                        if (log_ratio>-1.0673 && log_ratio <=-1.05981)
                        {
                                pH_value=4;
                        }
                        else if (log_ratio>-1.05981 && log_ratio <=-
1.04699)
                        {
                                pH_value= 4.1;
                        }
                        else if (log_ratio>-1.04699 && log_ratio <=-
1.03644)
                        {
                                pH_value=4.2;
                        }
                        else if (log_ratio>-1.03644 && log_ratio <=-
1.02746)
                        {
                                pH_value=4.3;
                        }
                        else if (log_ratio>-1.02746 && log_ratio <=-
1.01942)
                        {
                                pH_value=4.4;
                        }
                        else if (log_ratio>-1.01942 && log_ratio <=-
1.01556)
                        {
                                pH_value=4.5;
                        }
                        IJ.write("x, y, log(ratio), pH = "+i+", "+j+",
"+log_ratio+", "+pH_value);
                }

                else if ((log_ratio > -1.01556) && (log_ratio <=-0.96762))
                {
                        int c=((255 & 0xff)<<16) | ((165 & 0xff)<<8) | 0
& 0xff;
                        pH_ip.putPixel(i,j,c);
                        counter3++;
                        if (log_ratio>-1.01556 && log_ratio <=-1.01171)
                        {
                                pH_value=4.5;
                        }
                        else if (log_ratio>-1.01171 && log_ratio <=-
1.00379)
                        {
                                pH_value=4.6;
                        }
                        else if (log_ratio>-1.00379 && log_ratio <=-
0.99516)
                        {
                                pH_value=4.7;
                        }
                        else if (log_ratio>-0.99516 && log_ratio <=-
0.98537)
                        {
                                pH_value=4.8;
                        }
```

```
                else if (log_ratio>-0.98537 && log_ratio <=-
0.97401)
                {
                        pH_value=4.9;
                }
                else if (log_ratio>-0.97401 && log_ratio <=-
0.96763)
                {
                        pH_value=5;
                }
                IJ.write("x, y, log(ratio), pH = "+i+", "+j+",
"+log_ratio+", "+pH_value);
        }

        else if ((log_ratio > -0.96763) && (log_ratio <=-0.86986))
        {
                int c=((255 & 0xff)<<16) | ((255 & 0xff)<<8) | 0
& 0xff;
                pH_ip.putPixel(i,j,c);
                counter4++;
                if (log_ratio>-0.96763 && log_ratio <=-0.96072)
                {
                        pH_value=5;
                }
                else if (log_ratio>-0.96072 && log_ratio <=-
0.94519)
                {
                        pH_value=5.1;
                }
                else if (log_ratio>-0.94519 && log_ratio <=-
0.92717)
                {
                        pH_value=5.2;
                }
                else if (log_ratio>-0.92717 && log_ratio <=-
0.90643)
                {
                        pH_value=5.3;
                }
                else if (log_ratio>-0.90643 && log_ratio <=-
0.8828)
                {
                        pH_value=5.4;
                }
                else if (log_ratio>-0.8828 && log_ratio <=-
0.86986)
                {
                        pH_value=5.5;
                }
                IJ.write("x, y, log(ratio), pH = "+i+", "+j+",
"+log_ratio+", "+pH_value);
        }

        else if ((log_ratio > -0.86986) && (log_ratio <=-0.69826))
        {
                int c=((173 & 0xff)<<16) | ((255 & 0xff)<<8) |
47 & 0xff;
                pH_ip.putPixel(i,j,c);
                counter5++;
```

```
                    if (log_ratio>-0.86986 && log_ratio <=-0.85617)
                    {
                            pH_value=5.5;
                    }
                    else if (log_ratio>-0.85617 && log_ratio <=-
0.82645)
                    {
                            pH_value=5.6;
                    }
                    else if (log_ratio>-0.82645 && log_ratio <=-
0.79363)
                    {
                            pH_value=5.7;
                    }
                    else if (log_ratio>-0.79363 && log_ratio <=-
0.75773)
                    {
                            pH_value=5.8;
                    }
                    else if (log_ratio>-0.75773 && log_ratio <=-
0.71881)
                    {
                            pH_value=5.9;
                    }
                    else if (log_ratio>-0.71881 && log_ratio <=-
0.69826)
                    {
                            pH_value=6;
                    }
                    IJ.write("x, y, log(ratio), pH = "+i+", "+j+",
"+log_ratio+", "+pH_value);
            }

            else if ((log_ratio > -0.69826) && (log_ratio <=-0.45842))
            {
                    int c=((0 & 0xff)<<16) | ((255 & 0xff)<<8) | 0 &
0xff;
                    pH_ip.putPixel(i,j,c);
                    counter6++;
                    if (log_ratio>-0.69826 && log_ratio <=-0.67699)
                    {
                            pH_value=6;
                    }
                    else if (log_ratio>-0.67699 && log_ratio <=-
0.63244)
                    {
                            pH_value=6.1;
                    }
                    else if (log_ratio>-0.63244 && log_ratio <=-
0.58536)
                    {
                            pH_value=6.2;
                    }
                    else if (log_ratio>-0.58536 && log_ratio <=-
0.53601)
                    {
                            pH_value=6.3;
                    }
```

```
                else if (log_ratio>-0.53601 && log_ratio <=-
0.4847)
                {
                        pH_value=6.4;
                }
                else if (log_ratio>-0.4847 && log_ratio <=-
0.45842)
                {
                        pH_value=6.5;
                }
                IJ.write("x, y, log(ratio), pH = "+i+", "+j+",
"+log_ratio+", "+pH_value);
        }
        else if ((log_ratio > -0.45842) && (log_ratio <=-0.18558))
        {
                int c=((0 & 0xff)<<16) | ((128 & 0xff)<<8) | 0 &
0xff;
                pH_ip.putPixel(i,j,c);
                counter7++;
                if (log_ratio>-0.45842 && log_ratio <=-0.43178)
                {
                        pH_value=6.5;
                }
                else if (log_ratio>-0.43178 && log_ratio <=-
0.37765)
                {
                        pH_value=6.6;
                }
                else if (log_ratio>-0.37765 && log_ratio <=-
0.32276)
                {
                        pH_value=6.7;
                }
                else if (log_ratio>-0.32276 && log_ratio <=-
0.26761)
                {
                        pH_value=6.8;
                }
                else if (log_ratio>-0.26761 && log_ratio <=-
0.21273)
                {
                        pH_value=6.9;
                }
                else if (log_ratio>-0.21273 && log_ratio <=-
0.18558)
                {
                        pH_value=7;
                }
                IJ.write("x, y, log(ratio), pH = "+i+", "+j+",
"+log_ratio+", "+pH_value);
        }
        else if ((log_ratio > -0.18558) && (log_ratio <=0.055383))
        {
                int c=((135 & 0xff)<<16) | ((206 & 0xff)<<8) |
235 & 0xff;
                pH_ip.putPixel(i,j,c);
                counter8++;
```

```
                    if (log_ratio>-0.18558 && log_ratio <=-0.15872)
                    {
                            pH_value=7;
                    }
                    else if (log_ratio>-0.15872 && log_ratio <=-
0.10622)
                    {
                            pH_value=7.1;
                    }
                    else if (log_ratio>-0.10622 && log_ratio <=-
0.0559)
                    {
                            pH_value=7.2;
                    }
                    else if (log_ratio>-0.0559 && log_ratio <=-
0.00851)
                    {
                            pH_value=7.3;
                    }
                    else if (log_ratio>-0.00851 && log_ratio
<=0.035181)
                    {
                            pH_value=7.4;
                    }
                    else if (log_ratio>0.035181 && log_ratio
<=0.055383)
                    {
                            pH_value=7.5;
                    }
                    IJ.write("x, y, log(ratio), pH = "+i+", "+j+",
"+log_ratio+", "+pH_value);
            }

            else if ((log_ratio > 0.055383) && (log_ratio <=0.169984))
            {
                    int c=((0 & 0xff)<<16) | ((0 & 0xff)<<8) | 255 &
0xff;
                    pH_ip.putPixel(i,j,c);
                    counter9++;
                    if (log_ratio>0.055383 && log_ratio <=0.074345)
                    {
                            pH_value=7.5;
                    }
                    else if (log_ratio>0.074345 && log_ratio
<=0.108106)
                    {
                            pH_value=7.6;
                    }
                    else if (log_ratio>0.108106 && log_ratio
<=0.135542)
                    {
                            pH_value=7.7;
                    }
                    else if (log_ratio>0.135542 && log_ratio
<=0.155684)
                    {
                            pH_value=7.8;
                    }
```

```
                                        else if (log_ratio>0.155684 && log_ratio
<=0.167515)
                                        {
                                                pH_value=7.9;
                                        }
                                        else if (log_ratio>0.167515 && log_ratio
<=0.169984)
                                        {
                                                pH_value=8;
                                        }
                                        IJ.write("x, y, log(ratio), pH = "+i+", "+j+",
"+log_ratio+", "+pH_value);
                                }

                                else if (log_ratio > 0.169984)
                                {
                                        int c=((0 & 0xff)<<16) | ((0 & 0xff)<<8) |  128 &
0xff;
                                        pH_ip.putPixel(i,j,c);
                                        counter10++;
                                        IJ.write("x, y, log(ratio), pH = "+i+", "+j+",
"+log_ratio+", 8.25");
                                }

                                }
                        }
                }

                int total_pixel=w*h;

                IJ.write("Total Pixels = "+total_pixel);
                IJ.write("Saturated Pixels = "+counter_max);
                IJ.write("Background = "+counter_min);
                IJ.write("pH <= 4 = "+counter1);
                IJ.write("4.0 < pH <= 4.5 = "+counter2);
                IJ.write("4.5 < pH <= 5.0 = "+counter3);
                IJ.write("5.0 < pH <= 5.5 = "+counter4);
                IJ.write("5.5 < pH <= 6.0 = "+counter5);
                IJ.write("6.0 < pH <= 6.5 = "+counter6);
                IJ.write("6.5 < pH <= 7.0 = "+counter7);
                IJ.write("7.0 < pH <= 7.5 = "+counter8);
                IJ.write("7.5 < pH <= 8.0 = "+counter9);
                IJ.write("pH > 8 = "+counter10);

                int
sum=counter_max+counter_min+counter1+counter2+counter3+counter4+counter5+counter6+counter7+coun
ter8+counter9+counter10;
                IJ.write("Sum = "+sum);

                pH_image.show();

        }
}
```

BIBLIOGRAPHY

1. Lowell, B.B. and B.M. Spiegelman, *Towards a molecular understanding of adaptive thermogenesis.* Nature, 2000. **404**(6778): p. 652-660.
2. Alberts, B., et al., *Molecular Biology of the Cell.* 3rd ed. 1994, New York, N.Y.: Garland Publishing.
3. Ricquier, D., *Respiration uncoupling and metabolism in the control of energy expenditure.* Proc Nutr Soc, 2005. **64**(1): p. 47-52.
4. Nakamura, T. and I. Matsuoka, *Calorimetric Studies of Heat of Respiration of Mitochondria.* Journal of Biochemistry, 1978. **84**(1): p. 39-46.
5. Harada, Y., et al., *Mechanochemical coupling in actomyosin energy transduction studied by in vitro movement assay.* J Mol Biol, 1990. **216**(1): p. 49-68.
6. Sherwood, L., *Human physiology : from cells to systems.* 2004, Thomson/Brooks/Cole: Australia ; Belmont, CA.
7. Perry, M.M. and A.B. Gilbert, *Yolk transport in the ovarian follicle of the hen (Gallus domesticus): lipoprotein-like particles at the periphery of the oocyte in the rapid growth phase.* J Cell Sci, 1979. **39**: p. 257-272.
8. Krueger, K.M., et al., *The role of sequestration in G protein-coupled receptor resensitization - Regulation of beta(2)-adrenergic receptor dephosphorylation by vesicular acidification.* Journal of Biological Chemistry, 1997. **272**(1): p. 5-8.
9. Ferguson, S.S.G., *Evolving concepts in G protein-coupled receptor endocytosis: The role in receptor desensitization and signaling.* Pharmacological Reviews, 2001. **53**(1): p. 1-24.
10. von Zastrow, M., et al., *Regulated endocytosis of opioid receptors: cellular mechanisms and proposed roles in physiological adaptation to opiate drugs.* Current Opinion in Neurobiology, 2003. **13**(3): p. 348-353.
11. Hanyaloglu, A.C. and M. von Zastrow, *Regulation of GPCRs by Endocytic membrane trafficking and its potential implications.* Annual Review of Pharmacology and Toxicology, 2008. **48**: p. 537-568.
12. Iyer, V., et al., *Differential phosphorylation and dephosphorylation of beta(2)-adrenoceptor sites Ser262 and Ser355,356.* British Journal of Pharmacology, 2006. **147**(3): p. 249-259.
13. Kelly, E., *G-protein-coupled receptor dephosphorylation at the cell surface.* British Journal of Pharmacology, 2006. **147**(3): p. 235-236.
14. Leonhardt, H., L. Gordon, and R. Livingston, *Acid-base equilibriums of fluorescein and 2',7'-dichlorofluorescein in their ground and fluorescent states.* Journal of Physical Chemistry, 1971. **75**(2): p. 245-249.
15. Martin, M. and L. Lindqvist, *The pH dependence of fluorescein fluorescence.* Journal of Luminescence, 1975. **10**: p. 381-390.

16. Yguerabide, J., et al., *Steady-State Fluorescence Method for Evaluating Excited-State Proton Reactions - Application to Fluorescein.* Photochemistry and Photobiology, 1994. **60**(5): p. 435-441.
17. Sjoback, R., J. Nygren, and M. Kubista, *Absorption and Fluorescence Properties of Fluorescein.* Spectrochimica Acta Part a-Molecular and Biomolecular Spectroscopy, 1995. **51**(6): p. L7-L21.
18. Boens, N., et al., *Photophysics of the fluorescent pH indicator BCECF.* Journal of Physical Chemistry A, 2006. **110**(30): p. 9334-9343.
19. Rink, T.J., R.Y. Tsien, and T. Pozzan, *Cytoplasmic Ph and Free Mg-2+ in Lymphocytes.* Journal of Cell Biology, 1982. **95**(1): p. 189-196.
20. Paradiso, A.M., R.Y. Tsien, and T.E. Machen, *Na+-H+ Exchange in Gastric Glands as Measured with a Cytoplasmic-Trapped, Fluorescent Ph Indicator.* Proceedings of the National Academy of Sciences of the United States of America-Biological Sciences, 1984. **81**(23): p. 7436-7440.
21. Ward, W.W., et al., *Spectral Perturbations of the Aequorea Green-Fluorescent Protein.* Photochemistry and Photobiology, 1982. **35**(6): p. 803-808.
22. Llopis, J., et al., *Measurement of cytosolic, mitochondrial, and Golgi pH in single living cells with green fluorescent proteins.* Proceedings of the National Academy of Sciences of the United States of America, 1998. **95**(12): p. 6803-6808.
23. Kneen, M., et al., *Green fluorescent protein as a noninvasive intracellular pH indicator.* Biophysical Journal, 1998. **74**(3): p. 1591-1599.
24. Miesenbock, G., D.A. De Angelis, and J.E. Rothman, *Visualizing secretion and synaptic transmission with pH-sensitive green fluorescent proteins.* Nature, 1998. **394**(6689): p. 192-195.
25. Sankaranarayanan, S., et al., *The use of pHluorins for optical measurements of presynaptic activity.* Biophysical Journal, 2000. **79**(4): p. 2199-2208.
26. Karstens, T. and K. Kobs, *Rhodamine-B and Rhodamine-101 as Reference Substances for Fluorescence Quantum Yield Measurements.* Journal of Physical Chemistry, 1980. **84**(14): p. 1871-1872.
27. Kato, H., et al., *Imaging of thermal activation of actomyosin motors.* Proceedings of the National Academy of Sciences of the United States of America, 1999. **96**(17): p. 9602-9606.
28. Ross, D., M. Gaitan, and L.E. Locascio, *Temperature measurement in microfluidic systems using a temperature-dependent fluorescent dye.* Analytical Chemistry, 2001. **73**(17): p. 4117-4123.
29. Erickson, D., D. Sinton, and D.Q. Li, *Joule heating and heat transfer in poly(dimethylsiloxane) microfluidic systems.* Lab on a Chip, 2003. **3**(3): p. 141-149.
30. Van Keuren, E., D. Littlejohn, and W. Schrof, *Three-dimensional thermal imaging using two-photon microscopy.* Journal of Physics D-Applied Physics, 2004. **37**(20): p. 2938-2943.

31. Vanhouten, J. and R.J. Watts, *Temperature-Dependence of Photophysical and Photochemical Properties of Tris(2,2'-Bipyridyl)Ruthenium(Ii) Ion in Aqueous-Solution.* Journal of the American Chemical Society, 1976. **98**(16): p. 4853-4858.
32. Gota, C., et al., *Hydrophilic Fluorescent Nanogel Thermometer for Intracellular Thermometry.* Journal of the American Chemical Society, 2009. **131**(8): p. 2766-+.
33. Avnir, Y. and Y. Barenholz, *pH determination by pyranine: medium-related artifacts and their correction.* Anal Biochem, 2005. **347**(1): p. 34-41.
34. Kano, K. and J.H. Fendler, *Pyranine as a Sensitive Ph Probe for Liposome Interiors and Surfaces - Ph Gradients across Phospholipid Vesicles.* Biochimica Et Biophysica Acta, 1978. **509**(2): p. 289-299.
35. Straubinger, R.M., D. Papahadjopoulos, and K. Hong, *Endocytosis and Intracellular Fate of Liposomes Using Pyranine as a Probe.* Biochemistry, 1990. **29**(20): p. 4929-4939.
36. Overly, C.C., et al., *Quantitative Measurement of Intraorganelle Ph in the Endosomal Lysosomal Pathway in Neurons by Using Ratiometric Imaging with Pyranine.* Proceedings of the National Academy of Sciences of the United States of America, 1995. **92**(8): p. 3156-3160.
37. Orij, R., et al., *In vivo measurement of cytosolic and mitochondrial pH using a pH-sensitive GFP derivative in Saccharomyces cerevisiae reveals a relation between intracellular pH and growth.* Microbiology-Sgm, 2009. **155**: p. 268-278.
38. Szmacinski, H., I. Gryczynski, and J.R. Lakowicz, *Calcium-dependent fluorescence lifetimes of Indo-1 for one- and two-photon excitation of fluorescence.* Photochem Photobiol, 1993. **58**(3): p. 341-5.
39. Taki, M., J.L. Wolford, and T.V. O'Halloran, *Emission ratiometric imaging of intracellular zinc: design of a benzoxazole fluorescent sensor and its application in two-photon microscopy.* J Am Chem Soc, 2004. **126**(3): p. 712-3.
40. Srikun, D., et al., *An ICT-based approach to ratiometric fluorescence imaging of hydrogen peroxide produced in living cells.* J Am Chem Soc, 2008. **130**(14): p. 4596-7.
41. McLaurin, E.J., et al., *Two-photon absorbing nanocrystal sensors for ratiometric detection of oxygen.* J Am Chem Soc, 2009. **131**(36): p. 12994-3001.
42. Szmacinski, H. and J.R. Lakowicz, *Fluorescence Lifetime-Based Sensing and Imaging.* Sensors and Actuators B-Chemical, 1995. **29**(1-3): p. 16-24.
43. Sanders, R., et al., *Quantitative Ph Imaging in Cells Using Confocal Fluorescence Lifetime Imaging Microscopy.* Analytical Biochemistry, 1995. **227**(2): p. 302-308.

44. Hille, C., et al., *Time-domain fluorescence lifetime imaging for intracellular pH sensing in living tissues.* Analytical and Bioanalytical Chemistry, 2008. **391**(5): p. 1871-1879.
45. Chapman, C.F., et al., *The Use of Exogenous Fluorescent-Probes for Temperature-Measurements in Single Living Cells.* Photochemistry and Photobiology, 1995. **62**(3): p. 416-425.
46. Jeon, S.M., J. Turner, and S. Granick, *Noncontact temperature measurement in microliter-sized volumes using fluorescent-labeled DNA oligomers.* Journal of the American Chemical Society, 2003. **125**(33): p. 9908-9909.
47. Kaneko, H., et al., *Chloride accumulation in mammalian olfactory sensory neurons.* Journal of Neuroscience, 2004. **24**(36): p. 7931-7938.
48. Calleja, V., et al., *Monitoring conformational changes of proteins in cells by fluorescence lifetime imaging microscopy.* Biochemical Journal, 2003. **372**: p. 33-40.
49. Widengren, J., U. Mets, and R. Rigler, *Fluorescence Correlation Spectroscopy of Triplet-States in Solution - a Theoretical and Experimental-Study.* Journal of Physical Chemistry, 1995. **99**(36): p. 13368-13379.
50. Haupts, U., et al., *Dynamics of fluorescence fluctuations in green fluorescent protein observed by fluorescence correlation spectroscopy.* Proceedings of the National Academy of Sciences of the United States of America, 1998. **95**(23): p. 13573-13578.
51. Widengren, J., B. Terry, and R. Rigler, *Protonation kinetics of GFP and FITC investigated by FCS - aspects of the use of fluorescent indicators for measuring pH.* Chemical Physics, 1999. **249**(2-3): p. 259-271.
52. Hess, S.T., A.A. Heikal, and W.W. Webb, *Fluorescence photoconversion kinetics in novel green fluorescent protein pH sensors (pHluorins).* Journal of Physical Chemistry B, 2004. **108**(28): p. 10138-10148.
53. Shimomura, O., F.H. Johnson, and Y. Saiga, *Extraction, purification and properties of aequorin, a bioluminescent protein from the luminous hydromedusan, Aequorea.* J Cell Comp Physiol, 1962. **59**: p. 223-39.
54. Chalfie, M. and S. Kain, eds. *Green Fluorescent Protein: Properties, Applications, and Protocols*. 1998, Wiley-Liss, Inc.: New York, N.Y.
55. Prasher, D.C., et al., *Primary structure of the Aequorea victoria green-fluorescent protein.* Gene, 1992. **111**(2): p. 229-33.
56. Cormack, B.P., R.H. Valdivia, and S. Falkow, *FACS-optimized mutants of the green fluorescent protein (GFP).* Gene, 1996. **173**(1 Spec No): p. 33-8.
57. Ormo, M., et al., *Crystal structure of the Aequorea victoria green fluorescent protein.* Science, 1996. **273**(5280): p. 1392-5.
58. Elsliger, M.A., et al., *Structural and spectral response of green fluorescent protein variants to changes in pH.* Biochemistry, 1999. **38**(17): p. 5296-301.

59. Yang, F., L.G. Moss, and G.N. Phillips, Jr., *The molecular structure of green fluorescent protein.* Nat Biotechnol, 1996. **14**(10): p. 1246-51.
60. Scheyhing, C.H., et al., *Temperature-pressure stability of green fluorescent protein: a Fourier transform infrared spectroscopy study.* Biopolymers, 2002. **65**(4): p. 244-53.
61. Chalfie, M., et al., *Green fluorescent protein as a marker for gene expression.* Science, 1994. **263**(5148): p. 802-5.
62. Sasaki, E., et al., *Generation of transgenic non-human primates with germline transmission.* Nature, 2009. **459**(7246): p. 523-528.
63. Wong, F.H.C., et al., *A molecular thermometer based on fluorescent protein blinking.* Journal of the American Chemical Society, 2007. **129**(34): p. 10302-+.
64. Wolfbeis, O.S., et al., *Fluorimetric Analysis .1. A Study on Fluorescent Indicators for Measuring near Neutral (Physiological) Ph-Values.* Fresenius Zeitschrift Fur Analytische Chemie, 1983. **314**(2): p. 119-124.
65. Lutty, G.A., *The acute intravenous toxicity of biological stains, dyes, and other fluorescent substances.* Toxicol Appl Pharmacol, 1978. **44**(2): p. 225-49.
66. Pines, E., D. Huppert, and N. Agmon, *Salt Effects on Steady-State Quantum Yields of Ultrafast, Diffusion-Influenced, Reversible Photoacid Dissociation Reactions.* Journal of Physical Chemistry, 1991. **95**(2): p. 666-674.
67. Rini, M., et al., *Real-time observation of bimodal proton transfer in acid-base pairs in water.* Science, 2003. **301**(5631): p. 349-352.
68. Rini, M., et al., *Bimodal proton transfer in acid-base reactions in water.* Journal of Chemical Physics, 2004. **121**(19): p. 9593-9610.
69. Mohammed, O.F., et al., *Sequential proton transfer through water bridges in acid-base reactions.* Science, 2005. **310**(5745): p. 83-86.
70. Cox, M.J. and H.J. Bakker, *Parallel proton transfer pathways in aqueous acid-base reactions.* J Chem Phys, 2008. **128**(17): p. 174501.
71. Cox, M.J., B.J. Siwick, and H.J. Bakker, *Influence of Ions on Aqueous Acid-Base Reactions.* Chemphyschem, 2009. **10**(1): p. 236-244.
72. Peterman, E.J., F. Gittes, and C.F. Schmidt, *Laser-induced heating in optical traps.* Biophys J, 2003. **84**(2 Pt 1): p. 1308-16.
73. Sinton, D., X.C. Xuan, and D.Q. Li, *Thermally induced velocity gradients in electroosmotic microchannel flows: the cooling influence of optical infrastructure.* Experiments in Fluids, 2004. **37**(6): p. 872-882.
74. Saxena, A.M., J.B. Udgaonkar, and G. Krishnamoorthy, *Protein dynamics control proton transfer from bulk solvent to protein interior: a case study with a green fluorescent protein.* Protein Sci, 2005. **14**(7): p. 1787-99.
75. Li Jeon, N., et al., *Neutrophil chemotaxis in linear and complex gradients of interleukin-8 formed in a microfabricated device.* Nat Biotechnol, 2002. **20**(8): p. 826-830.
76. Clapham, D.E., *Calcium signaling.* Cell, 2007. **131**(6): p. 1047-1058.

77. Kholodenko, B.N., *Spatially distributed cell signalling.* FEBS Lett, 2009. **583**(24): p. 4006-4012.
78. Suzuki, M., et al., *Microscopic detection of thermogenesis in a single HeLa cell.* Biophys J, 2007. **92**(6): p. L46-8.
79. Grynkiewicz, G., M. Poenie, and R.Y. Tsien, *A new generation of Ca2+ indicators with greatly improved fluorescence properties.* J Biol Chem, 1985. **260**(6): p. 3440-3450.
80. Willoughby, D., R.C. Thomas, and C.J. Schwiening, *Comparison of simultaneous pH measurements made with 8-hydroxypyrene-1,3,6-trisulphonic acid (HPTS) and pit-sensitive microelectrodes in snail neurones.* Pflugers Archiv-European Journal of Physiology, 1998. **436**(4): p. 615-622.
81. Herman, P., et al., *Electroporative adjustment of pH in living yeast cells: Ratiometric fluorescence pH imaging.* Journal of Fluorescence, 2005. **15**(5): p. 763-768.
82. Ito, S., et al., *Application of fluorescence correlation spectroscopy to the measurement of local temperature in solutions under optical trapping condition.* Journal of Physical Chemistry B, 2007. **111**(9): p. 2365-2371.
83. Huppert, D., et al., *Effect of Water Activity on the Rate of Proton Dissociation.* Journal of the American Chemical Society, 1982. **104**(25): p. 6949-6953.
84. Cox, M.J. and H.J. Bakker, *Parallel proton transfer pathways in aqueous acid-base reactions.* Journal of Chemical Physics, 2008. **128**(17): p. -.
85. Stellwagen, E., J.D. Prantner, and N.C. Stellwagen, *Do zwitterions contribute to the ionic strength of a solution?* Analytical Biochemistry, 2008. **373**(2): p. 407-409.
86. Banks, D.S. and C. Fradin, *Anomalous diffusion of proteins due to molecular crowding.* Biophys J, 2005. **89**(5): p. 2960-2971.
87. Satsoura, D., et al., *Circumvention of fluorophore photobleaching in fluorescence fluctuation experiments: A beam scanning approach.* Chemphyschem, 2007. **8**(6): p. 834-848.
88. Ross, A. and J.N. Kearney, *The measurement of water activity in allogeneic skin grafts preserved using high concentration glycerol or propylene glycol.* Cell and Tissue Banking, 2004. **5**(1): p. 37-44.
89. Langmuir, D., *Aqueous environmental geochemistry.* 1997, Upper Saddle River, NJ: Prentice-Hall.
90. Snyder, S.H. and G.W. Pasternak, *Historical review: Opioid receptors.* Trends Pharmacol Sci, 2003. **24**(4): p. 198-205.
91. Denk, W., J.H. Strickler, and W.W. Webb, *Two-photon laser scanning fluorescence microscopy.* Science, 1990. **248**(4951): p. 73-6.
92. Jobsis, P.D., C.A. Combs, and R.S. Balaban, *Two-photon excitation fluorescence pH detection using 2,3-dicyanohydroquinone: a spectral ratiometric approach.* J Microsc, 2005. **217**(Pt 3): p. 260-4.

93. Kim, S., H.E. Pudavar, and P.N. Prasad, *Dye-concentrated organically modified silica nanoparticles as a ratiometric fluorescent pH probe by one- and two-photon excitation.* Chem Commun (Camb), 2006(19): p. 2071-3.
94. Charier, S., et al., *Photophysics of a series of efficient fluorescent pH probes for dual-emission-wavelength measurements in aqueous solutions.* Chemistry, 2006. **12**(4): p. 1097-113.
95. Yao, S., K.J. Schafer-Hales, and K.D. Belfield, *A new water-soluble near-neutral ratiometric fluorescent pH indicator.* Org Lett, 2007. **9**(26): p. 5645-8.
96. Shaw, G., et al., *Preferential transformation of human neuronal cells by human adenoviruses and the origin of HEK 293 cells.* Faseb J, 2002. **16**(8): p. 869-71.
97. Lakowicz, J.R., *Principles of fluorescence spectroscopy.* 3rd ed. 2006, New York: Springer. xxvi, 954 p.
98. Keith, D.E., et al., *mu-Opioid receptor internalization: opiate drugs have differential effects on a conserved endocytic mechanism in vitro and in the mammalian brain.* Mol Pharmacol, 1998. **53**(3): p. 377-384.
99. Mundell, S.J., et al., *Agonist-induced internalization of the metabotropic glutamate receptor 1a is arrestin- and dynamin-dependent.* J Neurochem, 2001. **78**(3): p. 546-551.
100. Mundell, S.J., et al., *Agonist-induced internalization of metabotropic glutamate receptor 1A: structural determinants for protein kinase C- and G protein-coupled receptor kinase-mediated internalization.* J Neurochem, 2003. **84**(2): p. 294-304.
101. Gruenberg, J. and K.E. Howell, *Membrane traffic in endocytosis: insights from cell-free assays.* Annu Rev Cell Biol, 1989. **5**: p. 453-481.
102. Banks, D.S., *Fluorescence Correlation Spectroscopy Studies Characterizing Diffusion and Photophysical Properties of Proteins*, in *Physics & Astronomy*. 2007, McMaster University: Hamilton. p. vi, 154.
103. Magde, D., E. Elson, and W.W. Webb, *Thermodynamic Fluctuations in a Reacting System 柵easurement by Fluorescence Correlation Spectroscopy.* Physical Review Letters, 1972. 29(11): p. 705-708.
104. Schwille, P., F*luorescence correlation spectroscopy and its potential for intracellular applications.* Cell Biochemistry and Biophysics, 2001. 34(3): p. 383-408.